ISBN 91-628-5539-5
LUNFD6/(NFFL-7214)2002

A Study of Parton Dynamics from Deep Inelastic Scattering Events Containing a Jet in the Forward Direction

Thesis submitted for the degree of
Doctor of Philosophy
by

Martin Karlsson

DEPARTMENT OF PHYSICS
LUND, 2002

Abstract

The DIS ep-scattering parton dynamics at low-x is characterised by an initial state cascade in which the virtualities of the propagator gluons are expected to take any kinematically allowed value, in contrast to the leading log behaviour. These dynamics might be enhanced by selecting events in which an energetic jet is found in the forward angular region at HERA, $1.735 < \eta_{JET} < 2.79$. The forward jet event differential cross-section is measured as a function of Bjoerken-x, of the forward jet p_T, and of the fraction of the proton energy carried by the forward jet, x_{JET}. A significant deviation from predictions based on standard DGLAP evolution can be observed. We also investigate events in which two hard jets ($p_T > 3.5\ GeV$) are found in addition to the forward jet, and measure their cross-section. For this class of events we also investigate the cross-section as a function of η, for different values of the angular distance, $\Delta\eta$, between the two hard jets.

Contents

Chapter 1

Introduction

The HERA accelerator can be seen as a type of "electron microscope", where electrons or positrons are scattered against the constituents in the proton at high energies, in order to investigate the inner structure of the proton. The sub-structure of the proton and the point-like nature of its constituents were first revealed by measurements made at the Stanford Linear Accelerator (SLAC). In Deep Inelastic Scattering (DIS), the lepton scatters against a quark of the proton, via the exchange of a photon, causing the proton to break up into a proton remnant and a so-called hard subsystem, created from the photon-quark interaction. The DIS cross-section can be parametrised by the proton structure functions, describing the probability of the lepton scattering against the proton, and describing the structure of the proton in terms of probability distributions of the partons in the proton. Deep inelastic scattering experiments such as those performed at HERA, have played a crucial role in gradually uncovering the proton structure, providing a detailed description of the interactions taking place in ep-scattering, and experimentally justifying the theory of Quantum Chromo Dynamics (QCD). Studies of data taken at HERA in 1992 led to the first observation of so-called rapidity gap events, in which no particles are produced adjacent to the proton direction of motion. These events are interpreted as arising from diffractive processes, in which the probe interacts with a colourless component[1] of the proton. The investigation of this type of interaction is necessary for gaining a full understanding of the proton inner structure and of QCD.

In a certain class of events, collimated flows of particles, $jets$, are created from the interaction. Starting from the final state partons of the different processes, the hadronisation process leads to the production of hadronic jets, that are seen as having the kinematic properties of the partons. The production of hadrons is described by phenomenological models such as the Lund string model. In order to reconstruct and define jets, so-called *jet algorithms* are used. In this thesis, a number of different jet algorithms have been studied, with the purpose of evaluating their ability to reconstruct the properties of the partons. The theoretical predictions of *event generator* programs, applying Monte Carlo computational techniques in making probability based estimates of the scattering, are used. Event generators provide us with the four-vectors of the particles at different theoretical stages of the interaction. The investigation of jet algorithms is carried out on inclusive scattering and on two different models of diffractive scattering.

[1]The mediator of diffractive exchange, sometimes referred to as the *Pomeron*, is assumed to have the quantum numbers of vacuum.

The description of the underlying parton dynamics of ep-scattering is of great interest to the development of QCD. Different approximative models, where calculations of the partonic final state are carried out through the use of so-called *evolution equations*, exist. The proton parton dynamics is modelled through the evolution of the proton parton density into a "ladder" of emissions. The probability of a series of subsequent emissions occurring, are calculated starting from the probability of the proton emitting a parton carrying a certain fraction of the proton momentum. The parton evolution equations, provide estimates of the contribution from the increasingly complex *higher order* processes to the final state. The so-called DGLAP[2] evolution equations provide a good description of the proton structure function F_2, as measured at HERA. However, a rise in F_2 is seen for the kinematic region where the gluon density of the proton becomes high. Although the DGLAP equations seem to reproduce the F_2 measurements quite well, it is expected that a the new dynamic, given by the BFKL[3] evolution equations, become important in the region of small fractional proton momenta, carried by the scattered parton, the *low-x* region. The inclusive F_2 measurement is not sensitive enough to the effects of the new parton dynamics and thus one has to investigate specific final states to enhance the signal.

In $forward\ jet\ events$, an energetic jet is found in the angular region close to the proton remnant. We expect the processes of forward jet events to contain a parton ladder having properties that are not visible in the typical standard DIS event. Forward jet events can be studied as a way of evaluating the description provided by different evolution equations. We have carried out a measurement of the forward jet event cross-section, using experimental data collected by the H1 collaboration during the 1997 running period at HERA. This means an increase in statistics, compared to the previous H1 forward jet analysis, by a factor ≈ 5, and thereby an improved accuracy of the measurement, which is based on a highly exclusive event selection[4]. In addition to the Bjoerken-x differential cross-section, $\frac{d\sigma}{dx}$, we have now been able to measure the forward jet event cross-section as a function of the forward jet transverse momentum, $p_{T,FWD}$, and as a function of x_{JET}, the fraction of the proton energy carried by the forward jet. Experimental data are compared to the theoretical predictions of a number of Monte Carlo generators, based on different evolution schemes. We also study a sub-set of forward jet events, where, in addition to the forward jet, two "hard" jets are found, and we will refer to this class of events as *2+forward jet events*. The differential cross-sections above, are measured also for these events, and we study the rapidity of the forward jet and the two different "hard" jets, for different angular configurations of the two hard jets.

In chapter 2 we will discuss deep inelastic scattering theory and the structure of the proton. Also discussed are the different methods of QCD evolution and the selection of jets. In chapter 3, diffractive DIS and the models thereof are discussed. The HERA accelerator and the H1 detector will be described in chapter 4. Our study of jet algorithms in deep inelastic and diffractive scattering is presented in chapter 5. The forward jet analysis is presented in chapter 6.

[2]The DGLAP evolution equations will be discussed in section 2.3.2.
[3]The BKFL evolution equations will be discussed in section 2.3.3
[4]A forward jet is found in $\approx 1\%$ of the ep DIS events at HERA.

Chapter 2

Deep Inelastic Scattering at HERA

In this chapter the kinematics and theory of deep inelastic lepton-proton scattering in the HERA framework, relevant to this analysis, is presented. A general theoretical description of Deep Inelastic Scattering, DIS, is given in section 2.1, and the proton structure is discussed in section 2.2. The different techniques and phenomenological models used in the calculation and generation of DIS processes are expanded on in sections 2.3 and 2.4. The production and selection of jets in DIS is briefly described in section 2.5.

2.1 DIS Kinematics

At HERA, beams of positrons, with an energy of 27.5 GeV, and protons of 820 GeV are brought to collide head on. The positron probes the proton through the exchange of a vector boson, in a *neutral current*[1] scattering process either a Z^0 particle or a photon. At HERA energies, the exchange is dominated by photons. We denote this by:

$$e^+ + p \rightarrow e^+ + X \tag{2.1}$$

In elastic scattering, the proton remains intact, $X \equiv p$. When inelastic scattering occurs, the proton does not remain unchanged and X is the hadronic final state, created from the photon-proton interaction. An inelastic event is one in which the invariant mass of the hadronic final state is much larger than the proton rest mass ($W^2 \gg m_p^2$). Deep Inelastic Scattering (DIS) occurs when the squared momentum transfer of the photon is very large compared to the proton rest mass ($Q^2 \gg m_p^2$). In such an event, the proton is split up completely and a new formalism is needed to describe the underlying dynamics.

If the lepton has four-momentum $P_e = (E_e, p_e)$ in the initial state, and four-momentum $P_e' = (E_e', p_e')$ in the final state, the squared negative four momentum transfer is defined:

$$Q^2 \equiv -q^2 = -(P_e - P_e')^2 \quad , \tag{2.2}$$

where q is the four momentum of the exchanged photon. The variable Q^2 may be considered the invariant mass squared of the exchanged photon.

[1] In a charged current process, the exchanged boson is a W^+, resulting in the process: $e^+ + p \rightarrow \nu_e + X$.

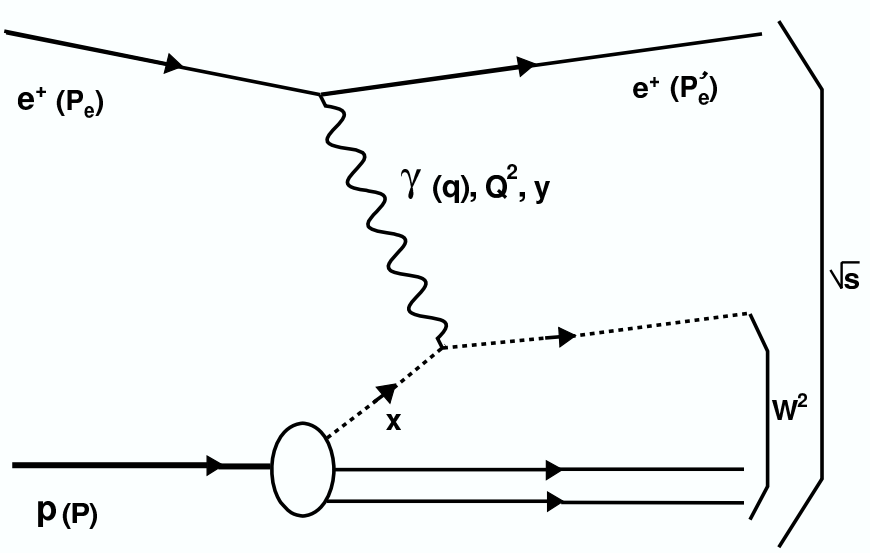

Figure 2.1: *Illustrative diagram of DIS kinematics. Four-momenta and kinematic variables related to different parts of the diagram are given.*

Other commonly used variables are the *Bjoerken-*x and y:

$$x \equiv \frac{Q^2}{2P \cdot q} \quad , \tag{2.3}$$

$$y \equiv \frac{P \cdot q}{P \cdot P_e} \quad , \tag{2.4}$$

where P is the four-momenta of the proton. In the *Quark Parton Model* (*QPM*), the proton is said to consist of mutually non-interacting point-like *partons*, quarks. The lepton scatters elastically against one of the partons, and the proton breaks up. Here, Bjoerken-x, is the fraction of the proton momentum carried by the struck quark, and y, is the fractional energy lost by the lepton in the collision, i.e. the fraction of the lepton energy carried by the photon in the proton rest frame.

The invariant mass squared of the photon-proton subsystem, equivalent to the invariant mass squared of the hadronic system in the final state, is denoted:

$$W^2 \equiv (P + q)^2 \quad , \tag{2.5}$$

and including also the lepton, the invariant mass squared of the full lepton-proton system is described by the variable:

$$s \equiv (P_e + P)^2 \quad , \tag{2.6}$$

which also is referred to as the centre-of-mass (CMS) energy squared of an event.

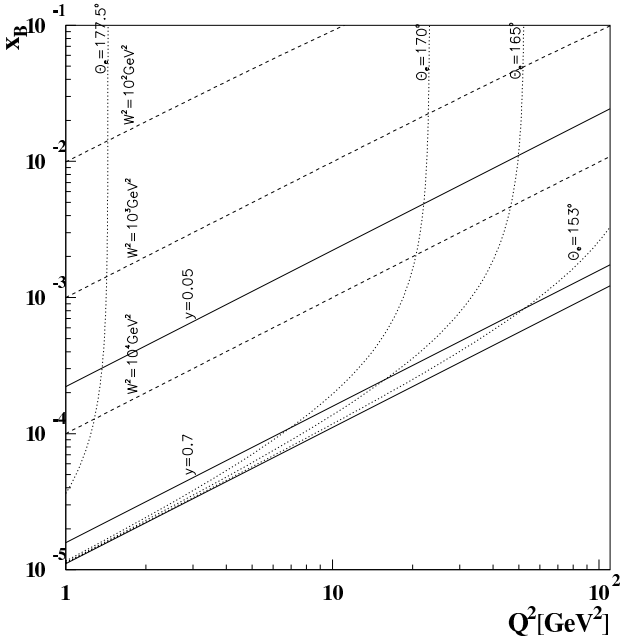

Figure 2.2: *The kinematic range in Q^2 and x, with y, W^2 and the polar angle of the scattered lepton, θ_e given, for the HERA CMS energy, $\sqrt{s} = 296\,GeV$.*

The collision between 27.5 GeV positrons and 820 GeV protons corresponds to a CMS energy, $\sqrt{s}$, of 296 GeV. The variables x, y, Q^2 and s are related according to:

$$Q^2 = xys \quad , \tag{2.7}$$

if the proton mass, m_p, is neglected. Inclusive[2] scattering is, neglecting the azimuthal degree of freedom, at a fixed value of s completely described by two of these variables, for example x and Q^2. (A plot over the kinematic relations of positron-proton collisions at HERA energies is shown in fig. 2.2.)

2.2 The Structure of the Proton

The differential cross-section for inclusive inelastic scattering can be parameterised using two *Structure Functions*, $F_1(x, Q^2)$, and $F_2(x, Q^2)$[3]

$$\frac{d^2\sigma}{dxdQ^2} = \frac{4\pi\alpha^2}{xQ^4}\left[xy^2 \cdot F_1(x, Q^2) - (1-y) \cdot F_2(x, Q^2)\right] \quad , \tag{2.8}$$

[2]When referring to inclusive ep-scattering, only the properties of the scattered electron, and not those of the hadronic final state are considered. The hadronic final state, created from the $\gamma - p$ interaction, is integrated over in an inclusive measurement.

[3]The relationship between F_1, F_2 and the cross-sections corresponding to longitudinally and transversely polarised photons respectively, σ_L and σ_T, is: $\frac{F_2 - 2xF_1}{2xF_1} = \frac{\sigma_L}{\sigma_T}$.

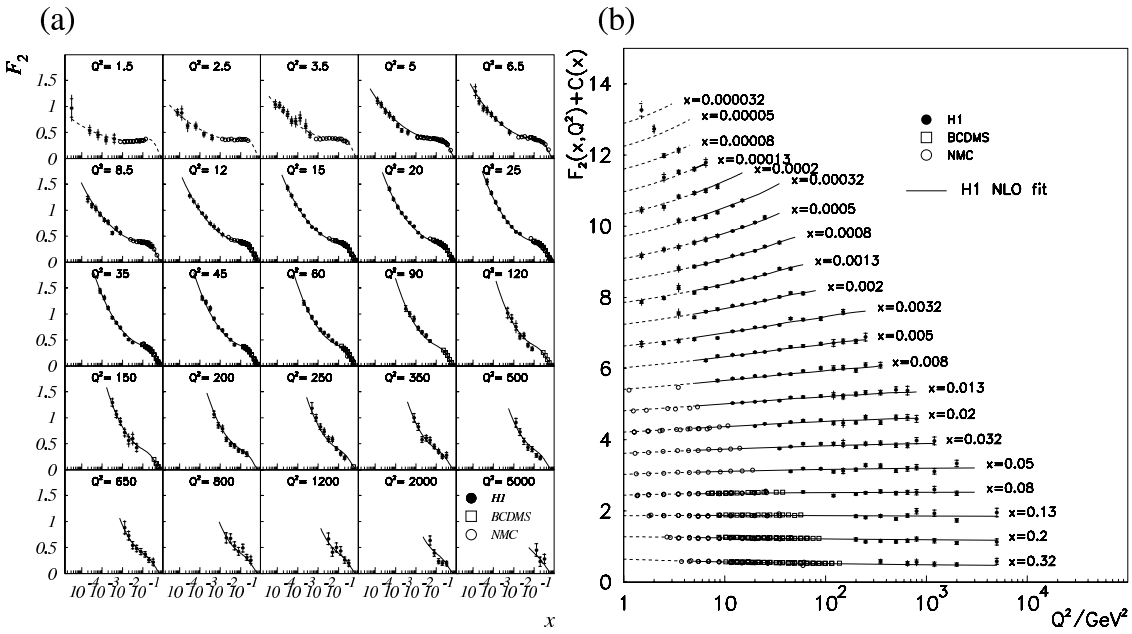

Figure 2.3: *A H1 measurement [1] of the proton structure function F_2 as a function of (a) x for different values of Q^2 and (b) Q^2 for different values of x.*

where α is the electro-weak coupling constant.

Lepton-proton scattering is of historical importance in that it led to the discovery of point-like quarks in the proton, and the development of the quark parton model. The proton was in this model originally said to consist of three partons, the *valence quarks*, each carrying approximately one third of the total momentum of the proton. At fixed medium values[4] of x, an approximate independence of Q^2 can be observed in F_2. This is a phenomena that is usually referred to as *Bjoerken scaling*, or *scale invariance*, meaning that Q^2 can be increased or decreased, leaving the values of the structure functions approximately unchanged:

$$F_i(x, Q^2) \approx F_i(x) \quad i = 1, 2 \tag{2.9}$$

It implies the existence of point like partons, quarks, inside the proton. Thus, above certain values of Q^2, the exchanged photon has a short enough wave-length, compared to the proton size, for the scattering to occur against the quarks. The point-like nature of the quarks leads to the scattering being independent of the photon wave-length and dependent only on the dimensionless variable x.

The structure functions are usually identified by the summation over *parton distribution functions*, $f_i(x, Q^2)$, describing the probability of a parton, i, carrying a fraction, x, of the proton

[4]The scaling behaviour is completely true for $x \approx 0.15$, and the scaling effect becomes smaller the further away from this value in x we are.

momentum at a certain value of Q^2. We have for *spin*-$\frac{1}{2}$ particles:

$$F_2(x, Q^2) = x \sum_i e_i^2 f_i(x, Q^2) \tag{2.10}$$

where e_i is the electric charge of a parton of type i. In the quark parton model of the proton, i, represents the valence quark flavours: i=u, d, and e_u=$\frac{2}{3}$, e_d=$-\frac{1}{3}$ (contributions from other type of quarks can also occur due to gluon splittings into pairs of so-called sea quarks, see below). The DIS cross-section can be divided into contributions from transversely and longitudinally polarised virtual photons. The structure function F_1 is dependent only on the transversely polarised contributions, while F_2 depends on both contributions. Neglecting the longitudinally polarised photon exchange contribution to the cross-section[5], F_1 and F_2 are related according to:

$$F_2(x, Q^2) = 2xF_1(x, Q^2) \quad , \tag{2.11}$$

which is called the *Callan-Gross relation* [2]. This relation is in agreement with experimental observations, within certain kinematic regions [3]. Using the notation of eq. (2.10), F_1 can be written as:

$$F_1(x, Q^2) = \frac{1}{2} \sum_i e_i^2 f_i(x, Q^2) \quad , \tag{2.12}$$

The quark parton model was invented before the theory of *Quantum Chromo Dynamics* (*QCD*) had been developed and it does not fully describe the proton structure, but may rather be regarded as providing a zeroth order approximation of the proton structure function. Deviations from the scaling relation in eq. (2.9) are observed in recent DIS data (see fig. 2.3) showing a certain change in F_2 with Q^2. This so-called *scaling violation* can not be explained within the boundaries of the quark parton model.

In QCD, the perturbative expansion of the structure function to higher orders in α_s includes the emission of gluons, and the creation of pairs of quarks and anti-quarks, *sea quarks* within the proton. The valence quarks are no longer independent of each other, but couple via gluons, the mediators of the strong force. The gluons can also couple to other gluons. In DIS it is possible for the photon to scatter not only against valence quarks, but also against sea quarks, created as a result of the strong interaction in the proton. At high values of Q^2, where the strong force operates at small distances, the partons move freely. In QCD, the *strong coupling constant*, α_s, depends on Q^2 such that the constituents of the proton approach *asymptotic freedom* with regard to the strong force, as Q^2 increases: $\alpha_s(Q^2) \to 0$, when $Q^2 \to \infty$. This means that above certain values of Q^2, the photon will probe the proton as consisting of free point-like objects, and DIS processes of higher orders become distinguishable if the virtuality[6] of the process is high enough. For smaller values of Q^2, we enter the so-called infra-red region, where $\alpha_s(Q^2)$ becomes large and the partons of the proton are bound together more tightly. The scattering will in this case occur as if the proton is a compact object in itself, rather than consisting of point-like partons.

[5]The contribution from longitudinally polarised exchanges can be neglected, since it does not contribute in the region of low values of the Bjoerken scaling variable y, where the ep neutral current DIS exchange at H1 generally takes place.

[6]The exchanged photon has a large virtuality when Q^2 is large, and becomes real when Q^2 has a small value.

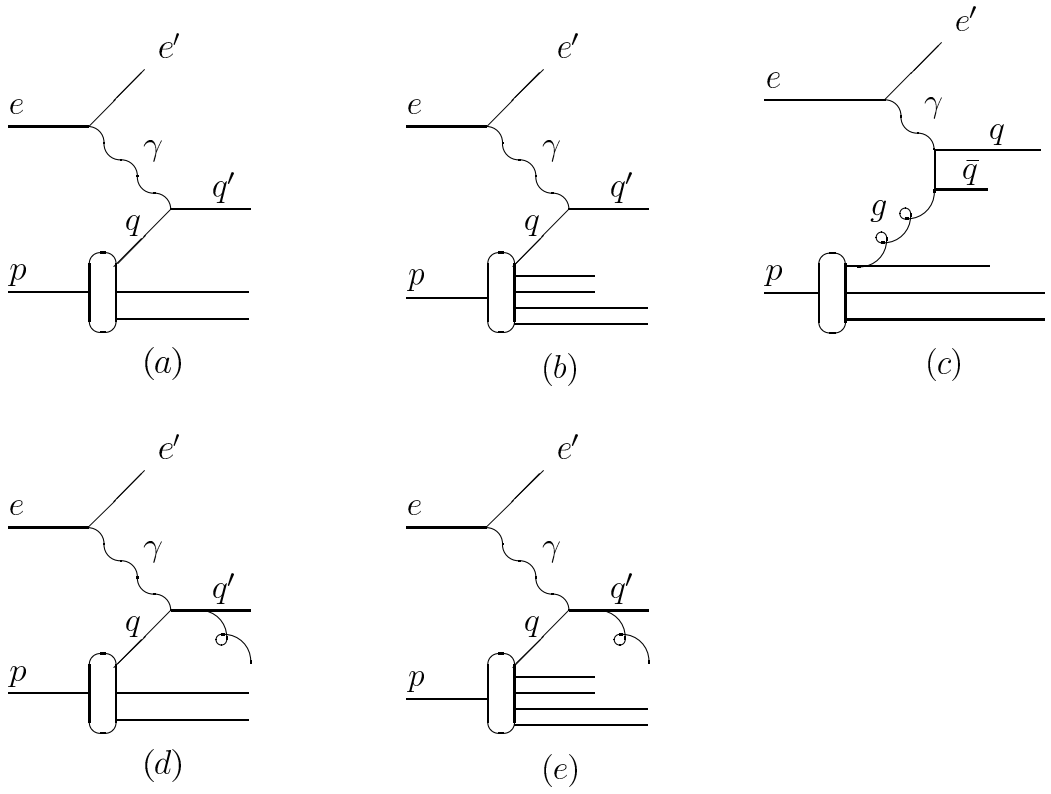

Figure 2.4: *Generic diagrams of deep inelastic ep scattering. Shown are (a) zeroth order α_s scattering on a valence quark; QPM, (b) QPM scattering on a sea quark, (c) first order α_s scattering against a sea quark; Boson Gluon Fusion, (d) first order α_s scattering on a valence quark, that emits a gluon; QCD-Compton and (e) QCD-Compton scattering on a sea-quark that emits a gluon. Versions of diagram (c), (d) and (e) with the legs crossed also exist. Versions of diagram (d) and (e) exist with the gluon emitted directly from the scattered quark, and with the legs of these diagrams crossed.*

2.3 DIS Processes and Evolution Equations

For large virtualities and for small values of the strong coupling constant, α_s, ep scattering is dominated by zeroth and first order processes, directly calculable in perturbative QCD. These processes will be described in section 2.3.1. With larger values of α_s, the perturbative expansion in QCD becomes less and less reliable. Gluon self-coupling and higher order processes need to be included, and full perturbative calculations to all orders are not possible in this context. Approximative methods of evolution are therefore applied to estimate higher order effects. In sections 2.3.2, 2.3.3 and 2.3.4 the DGLAP, BFKL and CCFM approximations of higher order QCD processes will be discussed.

2.3.1 Zeroth and First Order QCD processes

Figure 2.4.a is a generic Feynman diagram of a *QPM process*, in which the photon interacts directly with a valence quark and no gluons are emitted. The diagram does not contain any gluon vertices, and at this level, the scattering does not include any strong interaction. According to *Feynman rules*, the cross-section of this process is therefore not dependent on α_s, and it can be described as a *zeroth order α_s process* in QCD.

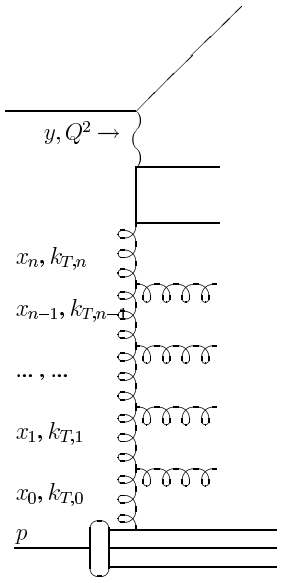

Figure 2.5: *Generic diagram of an evolution parton ladder, here consisting of gluon splittings, with the variables related to the different parts of the ladder given.*

A *first order,* $\mathcal{O}(\alpha_s)$, process in QCD, is a process for which the representative Feynman diagram contains one gluon vertex. In deep inelastic lepton-proton scattering, this is either a *Boson Gluon Fusion* process, in which a gluon in the proton is split up into a $q\bar{q}$ pair, and the photon scatters on one of these quarks (see fig. 2.4.c) or a $QCD-Compton$ process, in which the photon scatters on a quark that emits a gluon (see fig. 2.4.d). The cross-sections of these processes are proportional to α_s, and the scattering occurs with a probability set by α_s. Analogously, QPM and QCD-Compton scattering can also take place against a sea quark in the proton[7] (see fig. 2.4.b and fig. 2.4.e). Due to the complicated nature of the strong force, zeroth and first order α_s processes do not alone provide a proper description of the scattering. Higher order processes must be included, and these are treated by the concept of a parton density and the evolution equations.

2.3.2 DGLAP Evolution

In the $DGLAP$ (Dokshitzer, Gribov, Lipatov, Altarelli and Parisi) [4, 5, 6, 7] evolution method, the parton densities are evolved in the variable Q^2. Only the diagrams that give leading contributions of Q^2, or $log(Q^2)$ are taken into account. Different parton types are given different parton density functions, $f_j(x', t)$, describing the probability of finding a parton of type j, carrying a fraction, x', of the original proton momentum, at a given scale, t. Every parton, j, is also given a probability of originating from a parton of type i: $P_{i/j}(\frac{x}{x'})$, where, x, is the fraction of the proton momenta carried by parton i. The *splitting kernel*, $P_{i/j}(z)$, may be considered a probability density, in the sense that it describes the probability of a parton "containing" a daughter parton, carrying a fraction, z, of the parent quark momenta. The leading order (LO) α_s splitting kernels are derived from $2 \rightarrow 2$ scattering processes, and higher order kernels can be derived

[7] It should be noted however, that sea-quarks are created from gluon splittings and hence the result of a BGF-like process inside the proton.

analogously. From a starting value, t=${Q_0}^2$, the parton density functions are then evolved in Q^2, step by step, using the DGLAP equations:

$$\frac{df_i(x,t)}{d\log t} = \frac{\alpha_s(t)}{2\pi} \sum_j \int_x^1 \frac{dx'}{x'} f_j(x',t) P_{i/j}(\frac{x}{x'}) \quad , \tag{2.13}$$

where the sum is over all parton types, j, that the parton, i, can branch to. The parton density functions can then, at a higher scale, be compared to experimental data.

Terms of the type $\alpha_s log(Q^2)$ are characteristic results of the DGLAP evolution integrations, in the leading logarithmic approximation (*LLA*). A DGLAP evolution to $\mathcal{O}({\alpha_s}^n)$ may be considered a summation over a ladder of n consecutive parton branchings (see fig. 2.5) in which the propagating partons are $strongly\ ordered$ in virtuality. The virtuality can be written: $Q^2 = \frac{{k_T}^2}{1-z}$, and at small values of z, strong ordering in virtuality therefore also means strong ordering in transverse momentum squared:

$$k_{T0}^2 \ll k_{T1}^2 \ll ... \ll k_{Tn-1}^2 \ll k_{Tn}^2 \quad , \tag{2.14}$$

each parent parton, n, carrying a much larger transverse momentum than the daughter parton, $n-1$, and all parton transverse momenta (virtualities) being limited below by the fixed value, ${Q_0}^2$, at which the evolution starts, and above by the photon virtuality, Q^2. The $\alpha_s log(Q^2)$ terms represent the contribution to the scattering, from the parton splitting diagrams in which the partons are strongly ordered in transverse momentum squared, k_T^2, with respect to polar angle. Terms of the type $log(\frac{1}{x})$ represent the contribution from diagrams strongly ordered in fractional momenta. DGLAP is viable when the former contribution is large compared to the latter: $log(Q^2) \gg log(\frac{1}{x})$.

DGLAP provides a good description of the inclusive structure function as measured at HERA [1], even at low x. For low x, however, there is a growth in F_2 as x decreases. This is related to the high gluon density in this region. Evolving the parton ladder here, the $log(\frac{1}{x})$ contributions are expected to become substantial. Investigating the final state in DIS, by e.g. studying forward jet and particle production [8, 9, 10, 11, 12], the standard DGLAP description of data is not always satisfactory[8]. The applicability of DGLAP at low x is therefore in question, and another evolution method may be needed.

2.3.3 BFKL Evolution

The BFKL (Balitsky, Fadin, Kuraev and Lipatov) evolution [13, 14] of parton densities is made in x, or in terms of $log(\frac{1}{x})$. It is carried out for a ladder of parton splittings (see fig. 2.5), for which the propagating partons, $i = 1, n$ are strongly ordered in fractional momenta x_i:

[8]When considering the photon as a partonic particle, and with evolution taking place on both sides of the hard sub-system, the DGLAP description can reach an agreement with data also for the exclusive quantities of the hadronic final state.

$$x_0 \gg x_1 \gg ... \gg x_{n-1}, \gg x_n \quad , \tag{2.15}$$

where Bjoerken-x sets the lower limit.

The BFKL equations are applicable for the region $log(\frac{1}{x}) \gg log(Q^2)$ in LLA, and are expected to contribute primarily for evolution at low x. In the region of low x at HERA we, as mentioned above, see a rise in the structure function F_2, because of the high gluon density in this region, and the parton branchings are thought to be dominated by gluon splittings. BFKL evolution unfolds the gluon density in x and the BFKL evolution equation has the form:

$$\frac{df(x,k_T)}{d\log(\frac{1}{x})} = \int dk_T'^2 K(k_T^2, k_T'^2) f(x, k_T'^2) \quad , \tag{2.16}$$

where k_T is the transverse momentum of the parent parton in a particular splitting, and k_T' the transverse momentum of its daughter. The splitting dynamic is described by the operator $K(k_T^2, k_T'^2)$, which is called the *BFKL kernel*. The function $f(x, k_T^2)$, is referred to as the *unintegrated gluon density*:

$$xg(x,Q^2) = \int_0^{Q^2} \frac{dk_T'^2}{k_T^2} f(x,Q^2) \quad , \tag{2.17}$$

where $g(x,Q^2)$ is the proton gluon density.

No requirement on strong ordering in virtuality is made on BFKL evolution. A "random walk" in the propagator k_T:s may thus lead to a diffusion of the ladder into the infra-red region. Also, no limits are set on the possible energy of the emissions in the (LLA) evolution, and energy conservation is thereby broken.

For fixed Q^2 and α_s, and at small x, we have that [15] $f(x,k_T) \propto x^{-\lambda}$, where $\lambda = 3\alpha_s$ and $c = 4log2$. This is similar to the x dependence of F_2 for low values of x. Studying the structure function has so far not enabled us to determine whether BFKL resolves the rise in F_2 at low x or not. Therefore less inclusive quantities and regions where BFKL-like parton dynamics are expected to come into play are being investigated exclusively.

2.3.4 CCFM Evolution

The CCFM (Catani, Ciafaloni Fiorani, Marchesini) evolution [16, 17, 18, 19] of the parton density, is carried out in angle, under the condition of angular ordering between the ladder emissions:

$$\Theta_{i+1} > \Theta_i \quad , \tag{2.18}$$

where Θ_i is the polar angle of emission $i = 1, n$, with respect to the incoming parton. The ordering relation can be written:

$$Q_0 < q_1 z_1, \ ..., \ < q_{n-1} z_{n-1} < q_n, \ q_n z_n < \bar{q} \quad , \tag{2.19}$$

where z_i is the fraction of emission $i-1$:s momentum carried by emission i, and

$$q_i = \frac{p_{T,i}}{1-z} \quad , \tag{2.20}$$

where $p_{T,i}$ is the transverse momentum of emission i. The evolution starts at Q_0, and the above angular limit is set by $\bar{q}$. With the unintegrated gluon density, $\mathcal{A}$, taken as a function of three independent variables:

$$xg(x,\bar{q}) \simeq \int_0^{\bar{q}^2} dk^2{}_T x\mathcal{A}(x,k^2{}_T,\bar{q}) \quad , \tag{2.21}$$

the CCFM evolution equation can be written:

$$\bar{q}^2 \frac{d}{d\bar{q}^2} \frac{x\mathcal{A}(x,k_\perp,\bar{q})}{\Delta_s(\bar{q},Q_0)} = \int dz \frac{d\phi}{2\pi} \frac{\tilde{P}(z,\bar{q}/z,k_\perp)}{\Delta_s(\bar{q},Q_0)} x'\mathcal{A}(x',k'_\perp,\bar{q}/z) \tag{2.22}$$

where ϕ is the azimuthal angle, Δ_s is the Sudakow form factor and $\tilde{P}$ is the splitting function:

$$\tilde{P}(z,q,k_\perp) = \frac{\bar{\alpha}_s(q(1-z))}{1-z} + \frac{\bar{\alpha}_s(k_t)}{z}\Delta_{ns}(z,q,k_\perp) \quad , \tag{2.23}$$

and Δ_{ns}, is the *Non-Sudakow form factor*, characteristically controlling the dependence on z, of the evolution. In the DGLAP limit, with not too small z, the angular ordering becomes ordering in q:

$$Q_0 < ... < q_{n-1} < q_n < \bar{q} \tag{2.24}$$

When approaching the BFKL limit, z becomes small, and eq. (2.19) gives essentially no restriction in q. In the low-x region, the CCFM equation sums terms of $log(\frac{1}{x})$, equivalently to BFKL, but includes a full treatment of the kinematics at each splitting.

2.4 Matrix Elements, QCD Radiation and Hadronisation

Theoretical estimates of particle scattering can be carried out based on random number generation, applying *Monte Carlo* techniques, through so-called *event generator* computer programs. In an event generator, the probabilities of different interactions to occur are calculated, and the four-vectors of the particles at different levels of the interaction can be obtained.

The theoretical description of particle scattering, as typically implemented in current event generators, might be divided into a number of qualitatively different stages, with respect to process virtualities, momentum transfer, the couplings and time-scales involved in the interactions. In a DIS ep-scattering event, mediated by a photon, the photon-positron interaction is calculated from perturbative QED and the proton is described by parton density functions, fitted to the structure function, F_2. Hard parton processes up to leading order α_s can be calculated from *matrix elements* (ME), describing the probabilities for different interactions to occur, given by

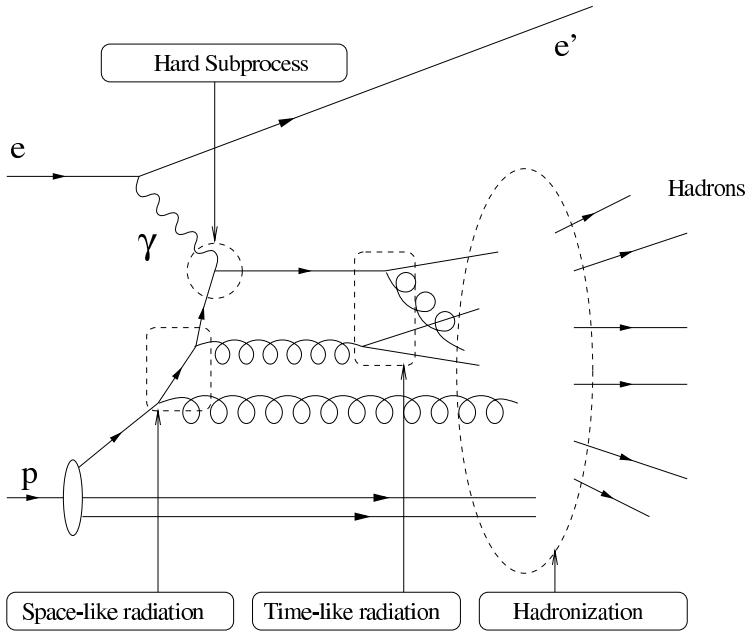

Figure 2.6: *Illustrative diagram over initial (space-like), final (time-like) state radiation, and hadronisation.*

perturbative QCD calculations. For the other stages of the scattering, approximative techniques and phenomenological models are applied. Initially, particles of high virtuality are involved in hard (large momentum transfer), space-like interactions, with strong interaction occurring at low values of α_s. In the next stage, *QCD radiation*, parton emissions, are added and simulate the influence of higher order corrections. *Hadronisation* occurs via strong interactions at large values of α_s, and is responsible for the transition from parton to hadron level, where various types of decays can occur at large time-scales. Two different ways of applying QCD radiation will be discussed in sections 2.4.1 and 2.4.2. Hadronisation according to the Lund String Model is described in section 2.4.3.

2.4.1 Parton Showers

QCD radiation may be modelled through initial and final state *parton showers*, meaning parton emissions as calculated with the help of QCD evolution equations. Initial state parton showers consist of space-like parton emissions that are added to the matrix element partons, and are used in event generators to account for higher order processes. The initial state parton emissions can branch into new partons with probabilities given by the splitting kernels of the evolution equations, time-like emissions are added to the final state partons and a shower of partons is thereby created.

Treating the photon as an extended object with a composite structure, the evolution equations may be applied also to the partons in the photon. In the *resolved photon model* [20, 21], the possibility for the photon to create a parton shower exists, by the evolution of a photon-induced

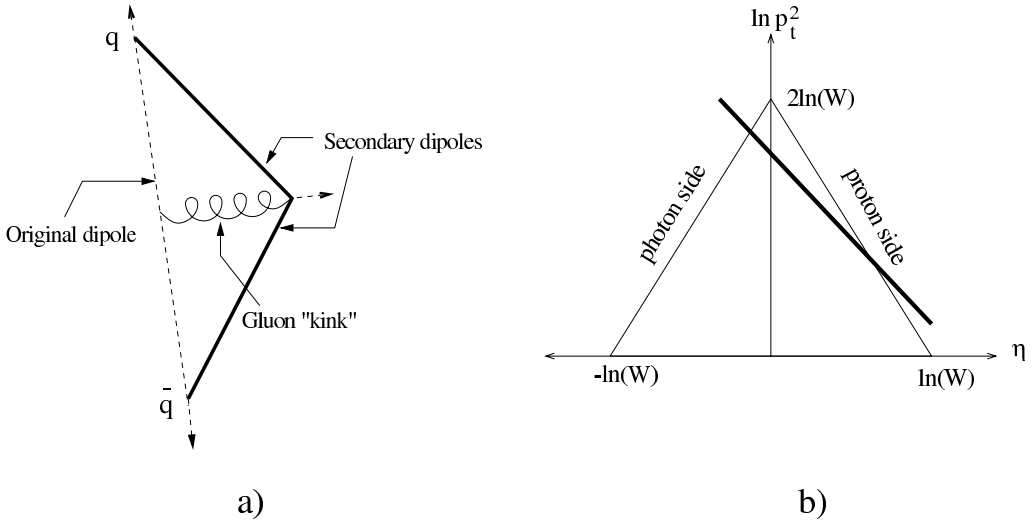

Figure 2.7: *Illustrative diagrams of CDM radiation.* (a) *A colour dipole is formed from a* $q\bar{q}$ *pair, and gluons are emitted. New dipoles are created and new gluons are radiated.* (b) *The phase space for gluon emission spanned by a dipole with energy W, for a gluon with transverse momenta* p_T *and pseudo-rapidity,* η*, in the dipole centre of mass system. The reduction in phase space due to the extension of the proton remnant is indicated on the right hand side of the diagram.*

parton ladder. The limits of the evolution are set by the virtuality of the photon, or the virtuality of the hard subprocess, as typically given by the mass of the hard subsystem squared, $\hat{s}$, or the transverse momentum squared of the partons, p_T^2.

In DIS event generators such as LEPTO [22], HERWIG [23] and RAPGAP [20], parton showers are applied according to a DGLAP-based (LLA) evolution. In the CASCADE [24] generator, initial state parton showers are applied according to CCFM evolution. RAPGAP and HERWIG include the possibility of resolving the photon. The parton showers of these generators are hence produced under the condition of strong ordering in virtuality, on the proton side, and applying the resolved photon model, also on the photon side.

2.4.2 The Colour Dipole Model

The *Colour Dipole Model*, (CDM) [25] was originally developed for processes of the type: $e^+e^- \rightarrow q\bar{q}$, and provides a different method for applying QCD radiation to the processes. The colour charges of the quark and the antiquark in these processes together form a colour dipole. The colour dipole is given a probability of emitting a gluon, where the emitted gluon can take part in creating a new dipole, leading to consecutive gluon radiations and creation of new dipoles. For a dipole of mass W, the phase space available for the emission of a gluon with pseudo-rapidity η[9] and transverse momentum, p_T, relative a coordinate system defined for the first emission is,

[9]Pseudo-rapidity is defined as η=$-ln(tan(\theta/2))$

due to conservation of energy, bounded by the relation [26] (see fig. 2.7):

$$p_T \cdot cosh(\eta) < \frac{W}{2} \quad , \tag{2.25}$$

Applying the colour dipole concept to deep inelastic ep scattering, the scattered quark and the proton remnant are responsible for creating the first dipole. The proton is not point-like and this suppresses the phase space available for gluon emission compared to the $e^+e^- \rightarrow q\overline{q}$ scattering case, since the quarks are point-like. The exchanged photon can be treated as an extended object, analogous to the resolved photon in the parton shower scenario, and this also leads to constraints on the gluon emission phase space.

The colour dipole model is implemented in the Monte Carlo generator $ARIADNE$ [27], where in DIS, boson gluon hard scattering is represented by matrix elements while QCD-Compton processes are completely covered by CDM radiation.

2.4.3 The Lund String Model

Strong interaction occurs between particles carrying colour charge. The strong force field has a tube-like structure with constant energy density per unit of length at large distances. The occurrence of single quarks has never been observed in nature, and this is accounted for in QCD by the energy of such a force field approaching infinity when a quark and an anti-quark are separated by large distances. This phenomena is referred to as *colour confinement*. The process that takes us from single partons, not observed in nature, to the hadrons that we can observe, is called hadronisation. It is described by phenomenological models, such as the *Lund String Model* [26]. In this model, the strong force is represented by *colour strings* that connect e.g. a quark and an antiquark together into a colourless meson. The force, F_S, of the string between the quarks, holding such a pair together, is approximately proportional to the distance, r, between them: $F_S \propto r$. Consider a parton level $q\overline{q}$ pair connected by a string, where the quarks possess certain kinetic energy and are moving apart. The force mediated by the string on the partons increases as the distance between the quarks increases, and kinetic energy is transferred from the quarks to the string. If the energy of the string is high enough, it can "break", and two new quark pairs can be created, each pair bound together by a colour string, which in turn can split up and create new pairs. This process of *string fragmentation* stops when the strings do not possess enough energy for new hadrons to be created. Partons are in this way, with increasing α_s, combined into hadrons.

2.5 Jet Production and Jet Algorithms

Flows of particles that are collimated in energy, momentum and angle are often referred to as *jets*. So-called *jet algorithms* provide different methods for combining parton, hadron or detector level objects into jets. The jet phase-space is set by a number of *resolution parameters*, defining e.g. how close in angular space two particles must be to be included in a jet.

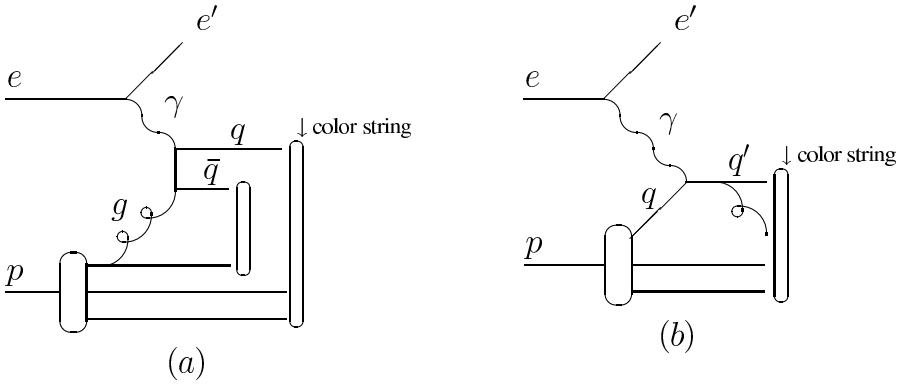

Figure 2.8: *String configuration in ep DIS for (a) a BGF process and (b) a QCD-Compton process.*

On the matrix element level, we might simply define each parton with a transverse momentum, p_T, in the HCMS[10], above a certain limit, $p_T > p_{Tmin}$, as a jet. For example, in an ep DIS boson gluon fusion process a $q\bar{q}$ pair is produced, where the two quarks are expected to possess high (HCMS) transverse momenta, and each quark of this pair may thereby be considered a jet. Considering QCD radiation on parton level, jets can be created from combinations of hard and soft partons or from hard or soft partons only. Requiring high (HCMS) jet p_T, the main contribution to jets from QCD radiation will however be in broadening the energy flow of the jets. On the hadron level we generally expect jets to carry the properties of the partons, and an $\mathcal{O}(\alpha_s)$ ep scattering process, containing two hard partons, is expected to give rise to two high p_T jets also on the hadron level. The proton remnant then often defines a jet in the most forward (beam-pipe) region, that through hadronisation becomes densely populated by particles. An event, where three jets are defined, including the proton remnant jet, is often referred to as a $(2+1)$ jet event.

Requirements on a jet algorithm include infra-red and collinear safety, meaning that adding a parton with infinitely low energy should not affect the result of the jet reconstruction. A good jet algorithm is also one that is able to differentiate between soft and hard partons and, when clustering hard jets, be able to associate soft partons with hard partons close in phase space in the way that best represents the underlying physics of an event. Furthermore, the hadronisation correction, i.e. the differences in energy between the final state partons and jets on hadron level should be small.

During the hadronisation process, the strong force can act in pulling partons away from their original direction of motion, due to so-called *string effects*, in string model terminology. In fig. 2.8, generic diagrams of BGF and QCD-Compton ep scattering processes are shown, and the different string configurations are indicated. Two partons bound together by a colour string exercise a force on each other, and get "dragged" in the direction of motion of the other parton of the pair. The signature of such effects at hadron level are asymmetries or shifts in the correlation with parton level jets. This also contributes to an increased energy flow of energetic jets, such as the proton remnant one, as mentioned above, due to the colour connections of the proton partons

[10]HCMS stand for Hadronic Center of Mass System, the $\gamma - p$ rest frame, where $q - P = 0$

with the rest of the system.

Chapter 3

Diffractive DIS at HERA

Rapidity gap events are characterised by an absence of hadronic activity in a sizable angular region with respect to the direction of motion of the proton. At HERA, around 10% of the DIS events exhibit such a gap in rapidity close to the beam pipe, where no hadrons are detected [28, 29]. This phenomena can be explained by introducing *diffractive* processes, in which the scattering is said to occur via a colour singlet intermediate state. There are no colour string connections to the proton remnant and consequently no contribution to hadronisation from this state. An overview of diffraction is given and the kinematics and theory of diffractive scattering is presented in sections 3.1-3.3. The different models of diffractive exchange relevant to this analysis are described in section 3.4.

3.1 Regge Theory and the Pomeron

The *Regge phenomenological model* [31, 32], as developed in the 1960-70's is not thoroughly based on QCD, but has nevertheless in many ways been successful in providing a description of long-range two-body hadronic scattering processes. These processes are described in terms of *reggeon* exchange and resonances. The possible resonances, i.e. those that conserve quantum numbers, are divided into groups of particles that all possess identical quantum numbers except for spin. The meson resonances that belong to one of these groups exhibit a linear dependence of the particle spins, J, on their mass squared, M^2. Denoting the square of the four-momenta transferred in the scattering with the Mandelstam variable, t, $|t| \equiv M^2$, the spin-mass dependence is governed by the *trajectory* that the resonances span in energy-angular momentum space:

$$\alpha(t) = \alpha(0) + \alpha' t \quad , \tag{3.1}$$

for small $|t|$, where $\alpha(0)$ is the intercept of the trajectory at $t = 0$, and α', makes up the slope in t. In fig. 3.1 the standard meson contributions, ρ, ω, f and a [30] are fitted to a trajectory with an intercept $\alpha(0) = 0.55$ and $\alpha' = 0.86$.

The *Optical Theorem* tells us that the total cross-section, σ_{TOT}, is proportional to the elastic amplitude of the scattering i.e. when $t = 0$. Let s denote the centre of mass energy squared, of the scattering. The variable s is like the variable t, a Mandelstam variable. For two-body scattering $ab \to a'b'$, we have $s = (P_a + P_b)^2$, and $t = (P_b - P_b')^2$, where P_a is the four-momenta

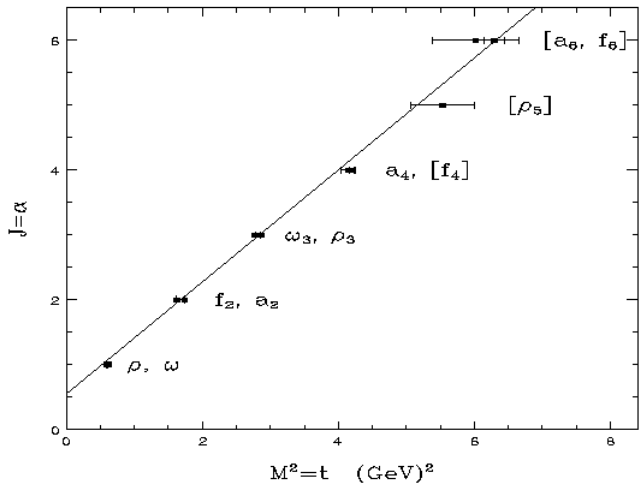

Figure 3.1: *The ρ, ω, f, a Regge trajectories. The line is a straight line fit with $\alpha(t) = \alpha(0) + \alpha' t = 0.55 + 0.86t$ [30].*

of particle a before the scattering has occurred, and with corresponding notation for the other components. The cross-section can be calculated as [33]:

$$\sigma_{TOT} \propto s^{\alpha(0)-1} \tag{3.2}$$

At high energies, the cross-section can not be described through meson contributions alone, and a *pomeron* contribution is postulated [34]. The pomeron trajectory is measured to be [35]:

$$\alpha(0) \approx 1.08 + 0.25t \tag{3.3}$$

No other particles are found on this trajectory and according to Regge theory, the particle resonances corresponding to the pomeron contribution carry the quantum numbers of vacuum. The pomeron mediates the characteristic interaction of diffractive interactions, where there is no exchange of quantum numbers.

The full parametrisation of the cross-section, including the contributions from both ordinary reggeon/meson, $I\!R$, and pomeron, $I\!P$, exchange, can now be written:

$$\sigma_{tot} = As^{\alpha_{I\!R}(0)-1} + Bs^{\alpha_{I\!P}(0)-1} \quad , \tag{3.4}$$

when $t \to 0$. A and B are process-dependent constants.

3.2 Diffractive DIS kinematics

In a DIS event, the photon can be seen as a point-like object probing the proton. Alternatively, the creation of a hard subsystem may be considered a result of *photon dissociation*, where in

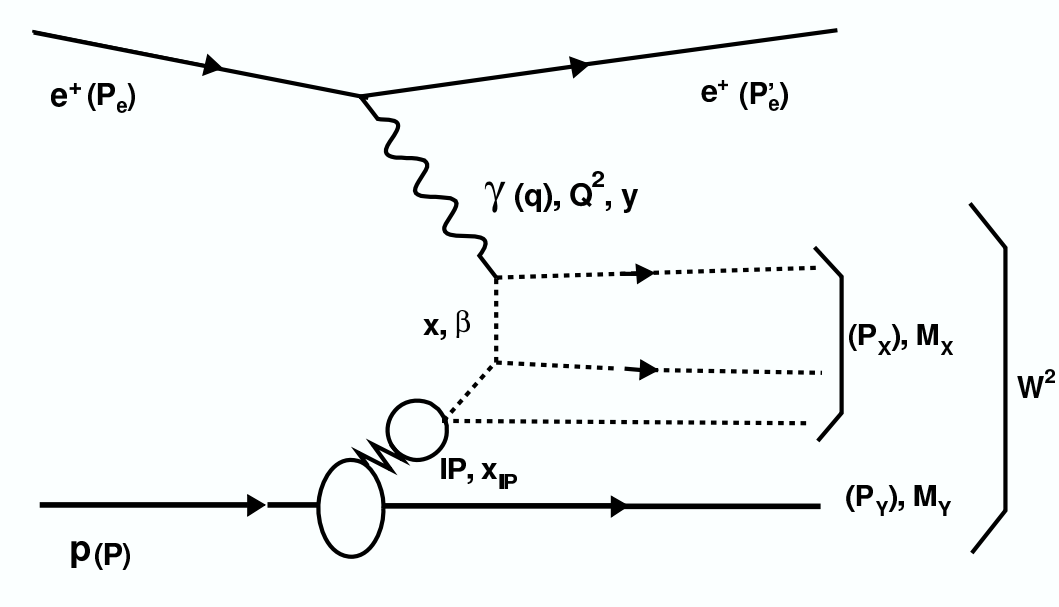

Figure 3.2: *Illustrative diagram of diffractive DIS kinematics. The four-momenta and kinematic variables related to different parts of the diagram are given.*

an $\mathcal{O}(\alpha_s)$ BGF event, the photon is transformed into a $q\bar{q}$ pair with the quantum numbers of the photon. In the same way, the transformation of the proton into an unbound state, can be referred to as *proton dissociation*. In diffractive γp scattering, the hadronic final state can be divided into two different subsystems X and Y: $\gamma + p \rightarrow X + Y$. System X, carrying four-momenta P_X, is the $\gamma - I\!P$ subsystem created from the interaction between the photon and the pomeron, or the *diffractive system*. The system Y, with four-momenta P_Y, is made up of the scattered proton. The subsystems are separated by a rapidity gap, since there is no colour string connection between them. The masses of the two different sub-systems are denoted M_Y and M_X, and are defined through:

$$M_Y^2 \equiv P_Y \cdot P_Y \quad , \tag{3.5}$$

and

$$M_X^2 \equiv P_X \cdot P_X \quad , \tag{3.6}$$

where P_X and P_Y is the four-momenta of respective system.

In diffraction, the pomeron momentum transfer squared, t, is given by:

$$t \equiv (P - P_Y)^2 \quad , \tag{3.7}$$

and describes the virtuality of the pomeron.

A variable of interest in processes including pomeron exchange is the $pomeron$-x, the fraction of the proton momentum carried by the pomeron in the scattering. It is defined:

$$x_{I\!P} \equiv \frac{q \cdot (P - P_Y)}{q \cdot P} \tag{3.8}$$

The variable β is in diffraction used to denote the fraction of the pomeron momentum carried by the parton interacting directly with the photon (the parton for which $Bjoerken-x$ is the fraction of the proton momenta it carries). We define it:

$$\beta \equiv \frac{Q^2}{2q \cdot (P - P_Y)} \quad , \tag{3.9}$$

and the relation between x, β and $x_{I\!P}$ is:

$$x = \beta x_{I\!P} \tag{3.10}$$

3.3 The Diffractive Structure Function

A diffractive structure function, F_2^D, can, analogously to the proton structure function, F_2, be used to describe the cross-section $\sigma_{ep \to eXY}$ for diffractive scattering. With five degrees of freedom, the complete expression of the cross-section may be written:

$$\frac{d^5\sigma_{ep\to eXY}}{d\beta\, dQ^2\, dx_{I\!P}\, dt\, dM_Y} = \frac{2\pi\alpha^2}{\beta Q^4}\left[2(1-y) + \frac{y^2}{1+R^{D(5)}}\right] \cdot F_2^{D(5)}(\beta, Q^2, x_{I\!P}, t, M_Y) \quad , \tag{3.11}$$

where $R^{D(5)}$ is the ratio between the contributions to the cross-section from longitudinally and transversely polarised photon scattering, which will be assumed to be zero from now on[1].

Performing an integration[2] over M_Y and $|t|$, a diffractive structure function with three degrees of freedom, $F_2^{D(3)}(\beta, Q^2, x_{I\!P})$, can be defined. Measurements of $F_2^{D(3)}$ have been performed by H1 [36] and different $fits$, corresponding to different descriptions of the partonic content of the pomeron have been applied. This has been done under the assumption that $F_2^{D(3)}$ is factorisable:

$$F_2^{D(3)}(\beta, Q^2, x_{I\!P}, t) = f_{I\!P/p}(x_{I\!P}, t) F_2^{I\!P}(\beta, Q^2) \quad , \tag{3.12}$$

where $f_{I\!P/p}$ is the pomeron flux and $F_2^{I\!P}$ is the pomeron structure function. We also assume the possibility of creating a Regge parametrisation of the pomeron structure function:

$$F_2^{D(3)}(\beta, Q^2, x_{I\!P}) = f_{I\!P/p}(x_{I\!P}) F_2^{I\!P}(\beta, Q^2) + f_{I\!R/p}(x_{I\!P}) F_2^{I\!R}(\beta, Q^2) \quad , \tag{3.13}$$

where $f_{I\!P/p}$ is the pomeron flux, $f_{I\!R/p}$ the reggeon flux and $F_2^{I\!R}$ is the reggeon structure function. The structure functions $F_2^{I\!P}$ and $F_2^{I\!R}$ describe the partonic structure corresponding to the reggeon

[1] At low values of the Bjoerken scaling variable y, the ep neutral current DIS exchange at H1 is dominated by transversely polarised photons.

[2] The integration over M_Y and $|t|$ is made since these quantities are not possible to measure at H1.

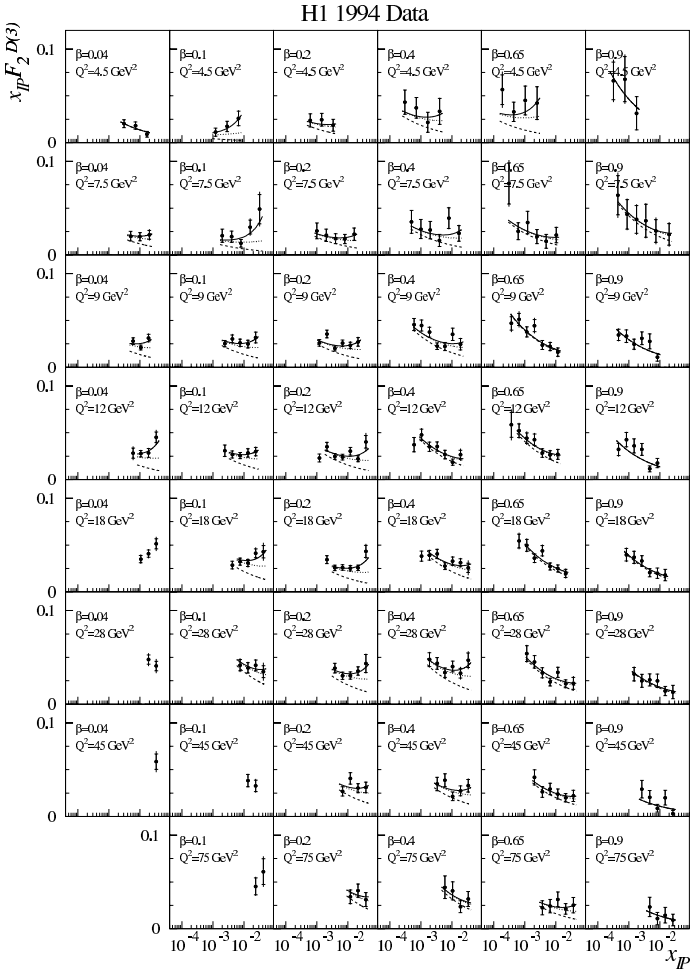

Figure 3.3: $x_{I\!P} F_2^{D(3)}(x_{I\!P}, \beta, Q^2)$ *plotted as a function of* $x_{I\!P}$ *for different values of* β *and* Q^2. *Regge parametrisation has been added to the plot. The reggeon contribution makes up the lower line, and the pomeron and reggeon contribution added make up the upper line.*

and pomeron exchanges respectively. We can hereby, like for the proton structure function, express the pomeron structure function in terms of parton distributions:

$$F_2^{I\!P}(\beta, Q^2) = \beta \sum_i e_i^2 f_i(\beta, Q^2) \quad , \tag{3.14}$$

where e_i is the electric charge of a parton of type i. The models treating the pomeron as having a partonic content are called *resolved* or *factorisable* pomeron models (see section 3.4.1). The different fits have been obtained using the DGLAP equations (see section 2.3.2), and based on different partonic structures, as described and compared to data in fig. 3.4- 3.5. In fit 1 there is a contribution only of quarks at the evolution starting scale and shortly summarising current findings at HERA, fit 1 does not provide a satisfactory description of the F_2^D scaling violations and is not able to provide a correct description of the hadronic final state. Fit 2 includes also gluons and thereby better describes the data. In fit 3 the gluon distributions are expanded polynomially

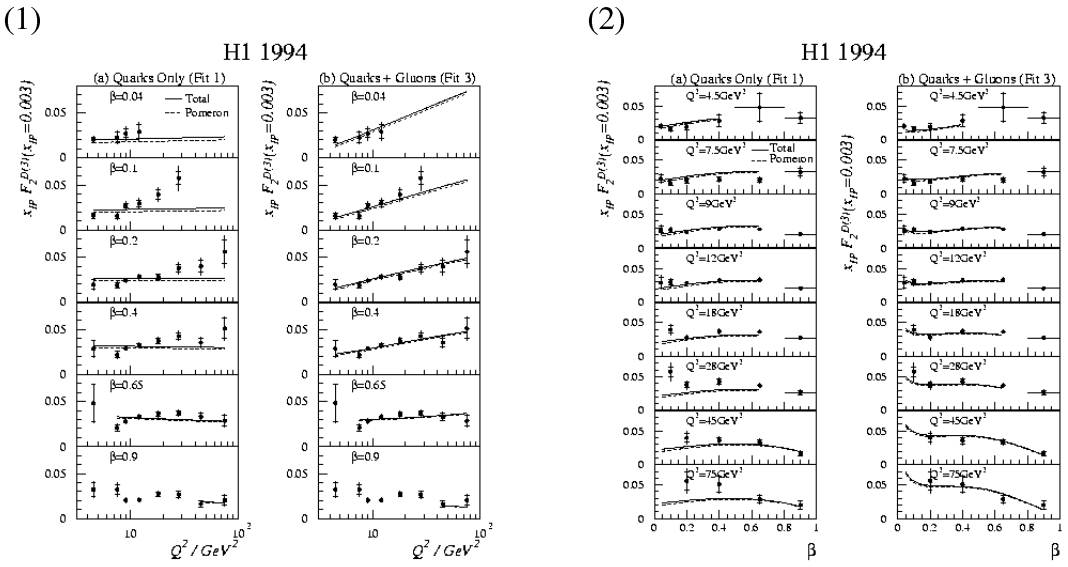

Figure 3.4: $x_{I\!P} F_2^{D(3)}(x_{I\!P}, \beta, Q^2)$ *shown for* (1) $x_{I\!P} = 0.003$ *as a function of* Q^2 *for different values of* β*. Different QCD fits are superimposed on the plots. The pomeron contribution is showed as a dashed line for* (a) *QCD fit 1, where only quarks contribute to the pomeron structure and* (b) *QCD fit 3, where quarks and gluons contribute to the pomeron structure. In* (2) $x_{I\!P} F_2^{D(3)}(x_{I\!P}, \beta, Q^2)$ *is plotted for* $x_{I\!P} = 0.003$ *as a function of* β*, for different values of* Q^2*. Different QCD fits are superimposed on the plots. The pomeron contribution is showed as a dashed line, for* (a) *QCD fit 1; only quarks contribute to the pomeron structure and* (b) *QCD fit 3; quarks and gluons contribute to the pomeron structure.*

and the description of data is again improved slightly.

3.4 Models of Diffraction

A number of different QCD-based models of diffraction exist. Here, the resolved pomeron model (section 3.4.1) and a model based on 2-gluon exchange (section 3.4.2) will be discussed.

3.4.1 The Resolved Pomeron Model

In the Ingelman-Schlein *resolved pomeron model* of diffractive exchange [37], the pomeron is treated as a hadronic particle with a partonic structure. The scattering takes place against a parton in the pomeron, causing it to break up, analogous to the scattering against the partons in the proton in standard DIS. In a zeroth order α_s diffractive process, the photon scatters on a quark in the pomeron (see fig. 3.6.a). A first order α_s diffractive process can be a BGF process in which a gluon in the pomeron splits up into a $q\bar{q}$ pair, and the photon scatters against one of these quarks (see fig 3.6.b), or a QCD-Compton process, in which the photon scatters against a quark in the pomeron, that emits a gluon, (see fig. 3.6.c). The $\gamma - I\!P$ scattering can in this way lead the pomeron breaking up, the creation of a hard subsystem with high (HCMS) p_T jets, and

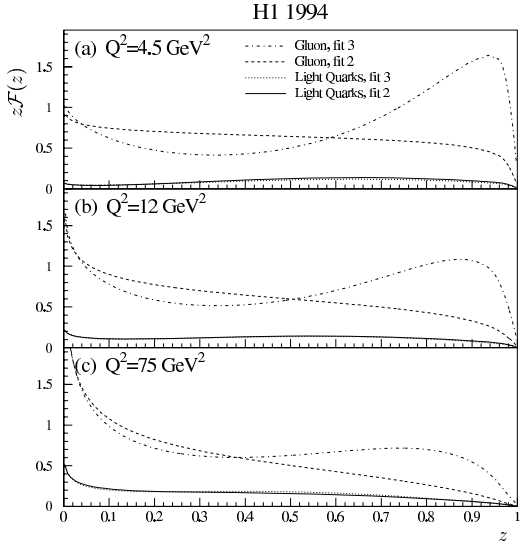

Figure 3.5: *Light quark and gluon contributions to $zF(z)$ for QCD fit 2 and QCD fit 3 for (a) Q^2=4.5 GeV^2, (b) Q^2=12 GeV^2 and (c) Q^2=75 GeV^2*

a *pomeron remnant* that continues in the proton direction of motion with low transverse momenta.

In the resolved pomeron model it is possible to factorise the diffractive structure function ${F_2}^{D(4)}$ into a probability of the scattering involving pomeron exchange, $f_{IP/p}(x_{I\!P}, t)$, and a structure function of the pomeron $F_2^{I\!P}$, as described in eq. (3.12). The pomeron structure function can be identified through a summation over the possible parton densities, $f_i(\beta, Q^2)$, according to eq. (3.14). The partons of the pomeron can, like those of the proton, emit further partons which may be described by the DGLAP or BFKL evolution schemes (discussed in chapter 2.3.2 and 2.3.3).

3.4.2 2-gluon Exchange

A perturbative model of diffraction may be constructed based on the exchange of a "hard pomeron", a system of multiple gluons that form a colour singlet state. In the simplest case, the pomeron consists of a colourless pair of gluons, in processes of the type $ep \rightarrow e' q\bar{q} p'$, and $ep \rightarrow e' q\bar{q} g p'$ (see fig. 3.7.a and b). The two gluons from the proton couple to the $q\bar{q}$ pair, and a gap in rapidity is hence expected to be created between the proton and the pair of hard partons in the final state. In a diffractive process mediated by a 2-gluon exchange, all partons are required to participate in the hard interaction. In a $q\bar{q}g$ final state, the gluon can have small transverse momentum, a situation similar to the BGF process in the resolved pomeron model. However, the gluon can also have large p_T, and a high p_T 3-jet system be created, which has no counterpart in the resolved pomeron model. In addition to the specific $x_{I\!P}$ dependence of 2-gluon exchange, the observation of a 3-jet high p_T system, without a soft remnant, would be the signature of a hard perturbative QCD diffractive process. The full energy of the colour singlet system will therefore be transferred to the hard subsystem, consisting of two ($q\bar{q}$), or three ($q\bar{q}g$) high (HCMS) p_T jets.

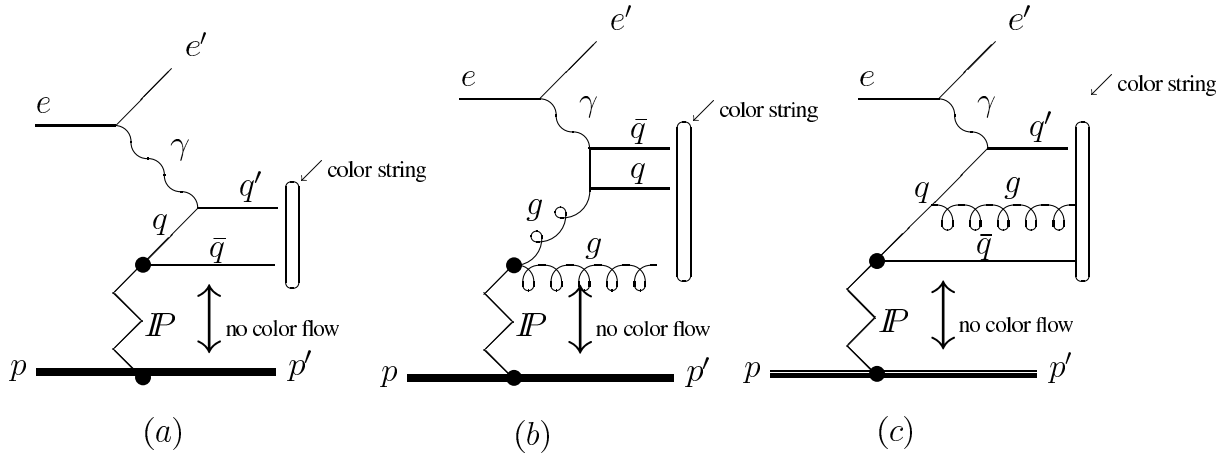

Figure 3.6: *Generic Feynman diagrams of the zeroth and first order α_s diffractive deep inelastic scattering processes in the resolved pomeron model for (a) diffractive QPM Zeroth order α_s scattering on a quark in the pomeron, (b) first order α_s Boson Gluon Fusion scattering on a quark in a $q\bar{q}$ pair, created from the split-up of a gluon in the pomeron and (c) first order α_s QCD-Compton scattering on a pomeron quark, that emits a gluon.*

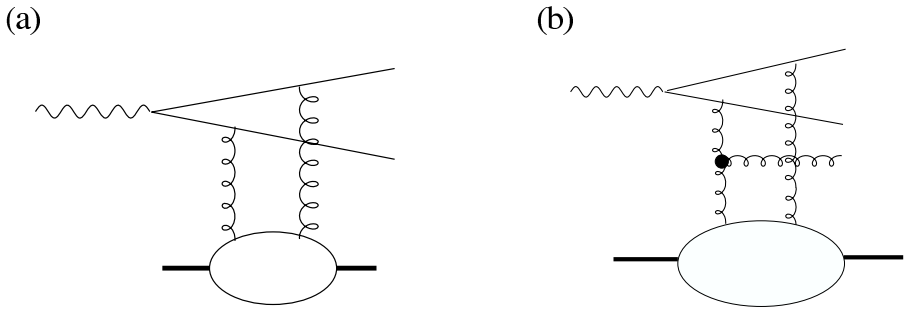

Figure 3.7: *Diagrams of diffractive processes involving 2-gluon exchange. Shown are (a) an $ep \to e'q\bar{q}p'$ and (b) an $ep \to e'q\bar{q}gp'$, process.*

Perturbative QCD calculations have been made for the above processes, assuming high-p_T (HCMS) parton configuration jets and large photon virtualities, Q^2, in [38, 39, 40, 41, 42]. The cross-section of 2-gluon exchange processes is highly dependent on the gluon density of the proton, $G_p(x_{I\!P}, \mu^2)$, and therefore also on $x_{I\!P}$, and the scale of the gluon density μ.

Chapter 4

HERA and the H1 Experiment

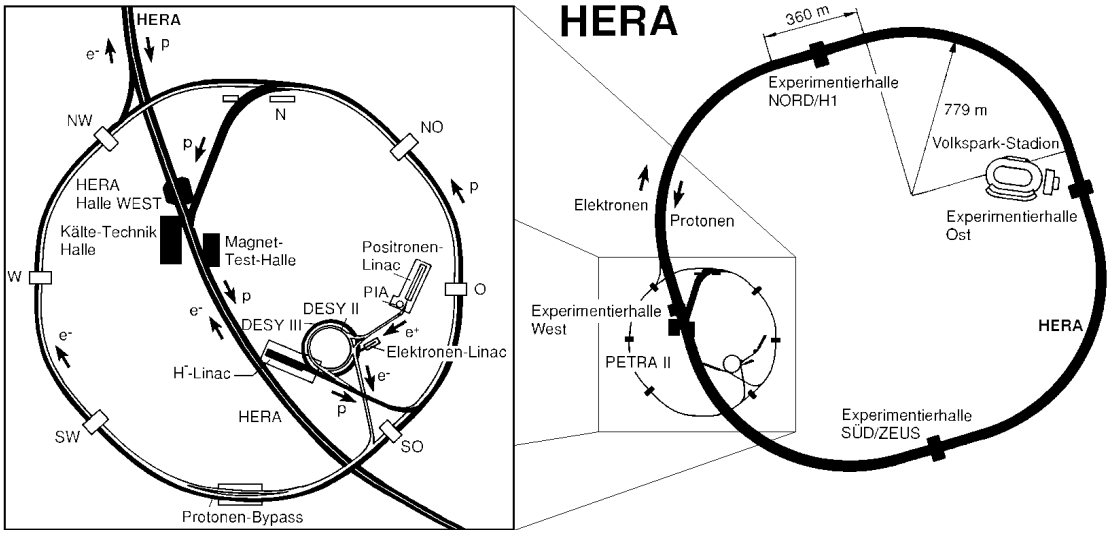

Figure 4.1: *Overview of DESY and HERA.*

H1 is one of the experiments situated at the HERA accelerator ring, where positrons[1] are brought to collide with protons at high energies. H1, like the ZEUS experiment, is dedicated to the study of lepton-proton scattering with the goal of exploring the inner structure of the proton. We will in this chapter first introduce the HERA accelerator in section 4.1 and the H1 detector with its various components will be described in section 4.2.

4.1 The HERA Accelerator

The HERA tunnel has a 6.3 km circumference and houses two beam lines in which electrons or positrons of 27.5 GeV and protons of 820 GeV (until 1997) or 920 GeV (from 1998 on) are accelerated and made to collide in two interaction points. The particles are first accelerated in linear accelerators, and then in the DESY and PETRA rings before they enter the HERA ring

[1] In July 1994 electrons were replaced by positrons at HERA.

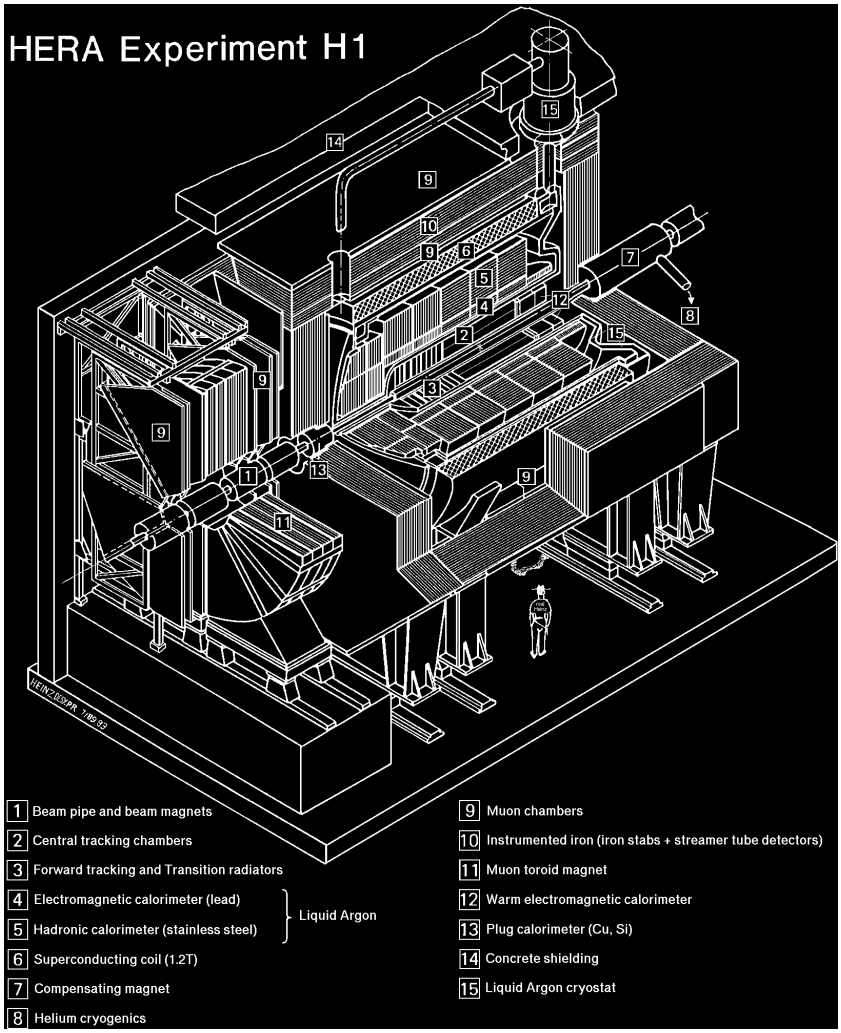

Figure 4.2: *The H1 detector.*

(see fig. 4.1). The leptons enter the HERA electron ring at 12 GeV, where they are accelerated to their final energy. The leptons are guided by warm magnets. The protons are accelerated to 40 GeV before they are injected into the HERA proton ring for their final acceleration. Superconducting magnets are used in HERA for keeping the protons on circle. The acceleration of both leptons and protons is made through the use of radio frequency cavities. Bunches of leptons and protons are stored in the rings with currents of around 30 mA and 80 mA respectively, and the bunch crossing interval is 96 ns.

4.2 The H1 Detector

The H1 detector consists of a multitude of components as can be seen in fig. 4.2. Due to the high energy of the protons, most particles produced in the collisions are expected to be emitted in the proton direction of motion, and the detector therefore carries denser instrumentation in this, the forward, region. The central 2 and forward 3 trackers surround the interaction point. Outside

the trackers, the Liquid Argon (LAr) calorimeter is situated and divided into an electromagnetic [4] and a hadronic part [5]. The Spaghetti Calorimeter, SpaCal [12] which has an electromagnetic and a hadronic part is placed outside the beam pipe in the backward region and completes the calorimetry, covering almost the full solid angle. A cylindrical super-conducting coil [6], surrounds the LAr calorimeter and generates a magnetic field of $1.15\,T$ with the field lines along the beam direction. The iron yoke [10] surrounding the detector, consists of multiple layers of iron with inserted streamer tubes, used for detecting muons and measuring the energy leakage out of the calorimetry. It also acts as a return yoke for the magnetic field. A more detailed description of the detector will be given in the next sections, starting with the calorimetry in 4.2.1 and the tracking in section 4.2.2. The H1 forward detectors are described shortly in section 4.2.3. The time-of-flight and triggering systems employed by H1 will be explained in sections 4.2.4 and 4.2.5. The H1 coordinate system is arranged with the positive z direction along the proton direction of motion, corresponding to a polar angle θ=0°. The positive x direction is pointing to the centre of the HERA ring, and corresponds to the azimuthal angle $\phi = 0°$. The y direction is along the vertical axis where $\phi = 90°$.

4.2.1 Calorimetry

The calorimetry of H1 consists of four different units and is built in the purpose of providing precise measurements of the particle energies and of enabling us to detect jets in the form of energy clusters. The SpaCal and LAr calorimeter together cover a range in pseudo-rapidity $-3.8 < \eta < 3.6$. A Plug calorimeter is implemented in the forward region, and the iron yoke tail catcher measures the energy leakage from the other calorimeters.

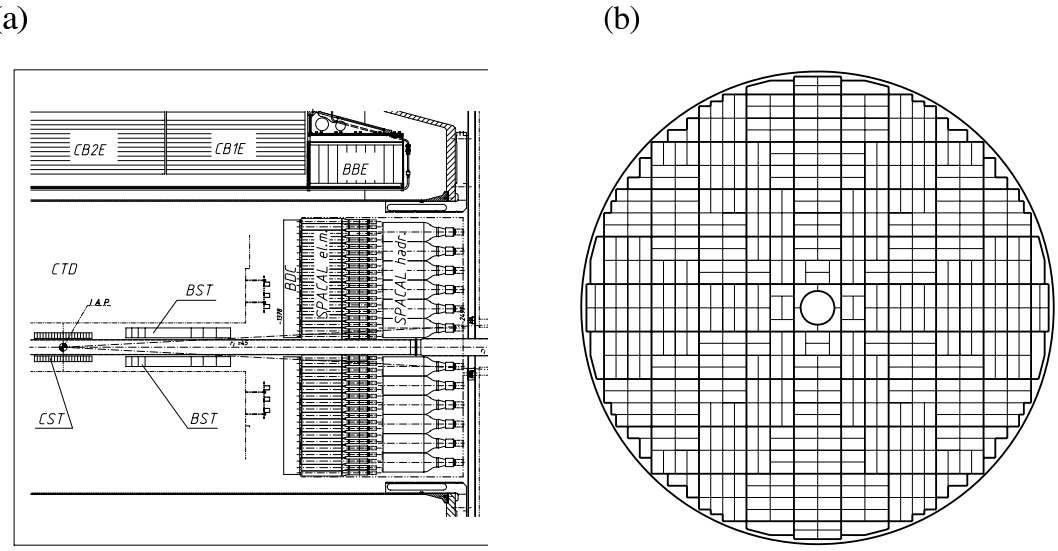

Figure 4.3: *The SpaCal detector. Shown is* (a) *the location in the H1 detector and* (b) *an* r-ϕ *sectional view of the SpaCal electromagnetic detector. Individual cells, each with their own photo-multiplier, are joined together to form two-cell structures (thin lines). The two-cell structures together make up 16 cell modules (thick lines).*

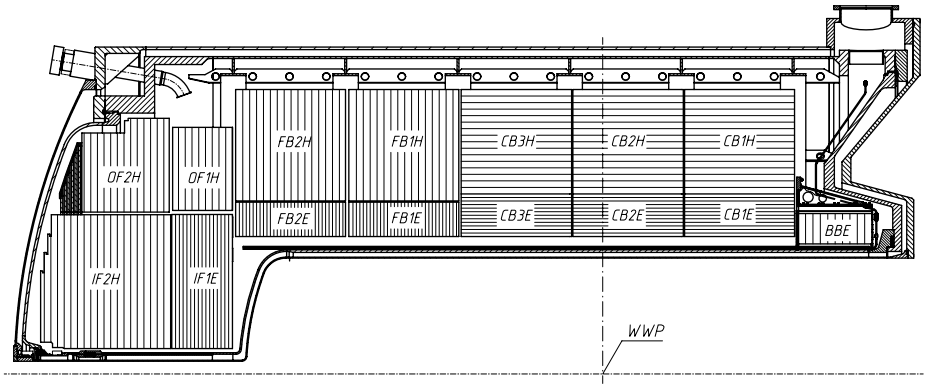

Figure 4.4: *The liquid Argon barrel calorimeter.*

At low values of the momentum transfer, $Q^2 < 100\ GeV^2$, the detectors used for measuring the scattered lepton are the electromagnetic calorimeters and the backward tracking detector. The scattered lepton proceeds in the backward direction and hits the SpaCal. The SpaCal [43] replaced the Backward ElectroMagnetic Calorimeter, $BEMC$ [44], in the end of 1994. It extends the acceptance down to smaller polar angles compared to the old detector, and provides an improved resolution in energy and angle. The angular acceptance of the SpaCal is: $153° < \theta < 177.5°$ which corresponds to a momentum transfer, Q^2, in the range: $1\ GeV^2 \lesssim Q^2 \lesssim 100\ GeV^2$. It is made up of lead sheets with grooves containing scintillator fibres. A particle entering the SpaCal causes a particle shower to develop and the shower particles hitting the fibres cause scintillation. The scintillation energy is then collected and amplified by a photo multiplier tube. The calorimeter is divided into an electromagnetic and a hadronic part (both consisting of cells of lead sheets) making the SpaCal able to isolate the scattered lepton from the hadronic background with great accuracy. The electromagnetic calorimeter has an energy resolution of $\frac{0.07}{\sqrt{E(GeV)}}$, and the hadronic resolution of the SpaCal is $\frac{0.3}{\sqrt{E(GeV)}}$. The SpaCal signal is combined with tracking chamber information as to further reduce backgrounds (more on the trackers is given in section 4.2.2).

The LAr calorimeter has an electromagnetic and hadronic part, and it is situated inside a solenoid magnet as to minimise the amount of dead material in front of it. It is built of 8 wheels in z, each consisting of six to eight sections covering ϕ. The showers in the electromagnetic calorimeter are created through the use of lead plates, while stainless steel is used in the hadronic part. The LAr calorimeter covers in total the range $3° < \theta < 154°$ and can be used for detecting the scattered lepton when its polar angle is below $154°$. The hadronic energy resolution of the LAr is $\sigma(E)/E \approx 0.5\sqrt{(E)}$, and the electromagnetic energy resolution is $\sigma(E)/E \approx 0.11\sqrt{(E)}$.

The calorimetry is complemented by a Plug Calorimeter in the forward region. It covers a range in pseudo-rapidity that is $3.5 < \eta < 5.0$. The instrumentation of the iron yoke acts as a calorimetric tail catcher in the H1 calorimetry, it is used for detecting the particles of the hadronic showers that manage to leak out of the other calorimeters. The tail catcher is divided into three

sections, the central barrel region and the forward and backward end caps. Each of these sections contain 16 layers of streamer tubes.

4.2.2 Tracking

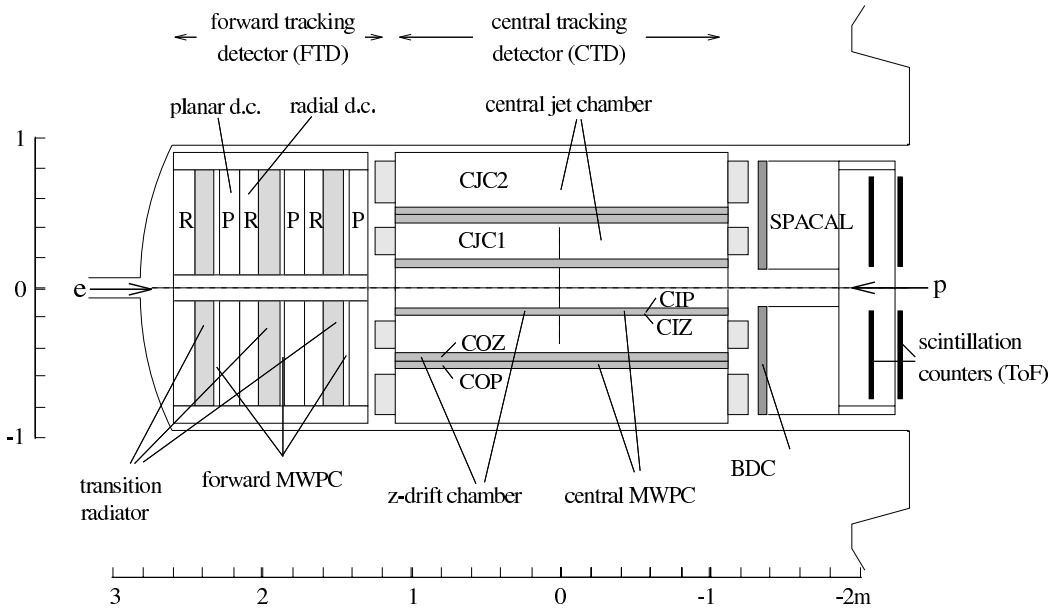

Figure 4.5: *The central and forward tracking system of H1.*

The H1 tracking system is divided into three different parts, the forward, backward and central trackers, as seen in fig. 4.5. The full tracking system covers a range in pseudo-rapidity of $-3 < \eta < 2.8$. The applied magnetic field bends the trajectories of charged particles in the $r-\phi$-plane, and from the bend of the tracks, the particle momentum can be measured. Trackers delivering a fast read-out can also be included in the triggering system (see section 4.2.5).

A Silicon Tracker is placed next to the beam pipe. Outside this, is the Central Tracking Detector (CTD), comprising six chambers housed in an aluminium tank. Closest to the beam pipe of these are the Central Inner Proportional Chamber (CIP) and the Central Inner z Chamber (CIZ). They are followed by the inner Central Jet Chamber, the CJC1, the Central Outer z Chamber (COZ), the Central Outer Proportional Chamber (COP) and the outer central jet chamber (CJC2). Together they cover a polar angular range of $15° < \theta < 165°$. The combined track measurements, give a momentum resolution for charged tracks of $\sigma_p/p^2 \approx 3 \times 10^{-3}\, GeV^{-1}$, where p is the particle momentum. The angular resolution is $\sigma_\theta \approx 1\ mrad$. The Forward Tracking Detector (FTD) consists of three identical $supermodules$ placed around the z axis and covering an angular range $5° < \theta < 30°$. In every supermodule are included twelve layers of planar drift chambers with wires in the $r-\phi$ plane, each plane rotated by $60°$ in ϕ for spatial measurements, and radial drift chambers for a high resolution in ϕ. The backward tracking detector is synonymous with the Backward Drift Chamber, BDC, that is mounted in front of the SpaCal and is used together with information from the vertex position in measuring the angle with a resolution of

$0.5\,mrad$. The angular acceptance is similar to that of the SpaCal, $153° < \theta < 177.5°$. It is built from four orthogonal double-layer drift chambers, containing sense wires that are positioned as to produce a radial drift direction, optimising the resolution in the polar angle θ.

4.2.3 The Forward Muon, Proton and Neutron Detectors

The reconstruction of muons exiting in the H1 forward direction is made by use of the $Forward\ Muon\ Spectrometer$, which is placed after the return yoke and covers an angular range of $3° < \theta < 17°$. It comprises in total six drift chambers, three situated on each side of the Muon Toroid magnet. The chambers are divided up for measurements in both angular regions, four for measuring in θ and two in ϕ.

Also placed in the forward direction is a $Proton\ Remnant\ Tagger$ comprising seven individual scintillators around the beam-pipe. Its purpose is to give a signal when particles from the proton remnant are scattered in the angular region close to the beam-pipe. The $Forward\ Proton\ Spectrometer$ is contained in so-called $Roman\ Pots$ inside the beam-pipe. At a distance of 106 meters to the interaction point, the $Forward\ Neutron\ Counter$ is situated. It is intended for events where a neutron is created from the proton remnant.

4.2.4 Time-of-Flight System

The Time-of-Flight (ToF) system consists of a number of scintillators, placed in the end caps of the return yoke and in the forward region close to the beam pipe. The SpaCal also contributes with time-of-flight information. The purpose of the system, is to reject background relating from beam-gas and beam-wall interactions, taking place outside of the detector. Particles stemming from such backgrounds are expected to have a time-of-arrival that differs from those originating from the interaction point. The different scintillators and the "HERA clock", based on the bunch-crossing frequency of the beams, together provide an exact estimate of the particle flight times and events are rejected on basis of this.

4.2.5 The Triggering System

The high bunch crossing frequency ($\approx 10\ MHz$) at HERA and the number of read out channels (≈ 270000) require a triggering and read-out system that is able to readily select among the events detected by H1. The problem is that the read-out time may not be short enough compared to the bunch crossing interval, to secure the events being read out. Instead an event may be missed by the system while a previous one is being processed. The triggering system is therefore set up as to select the events that satisfy certain physics conditions and are of interest to the different H1 analyses.

The triggering is divided up into four different levels, L1-L4 and works by combining the different trigger systems that are found on sub-detectors throughout H1. The Level 1 (L1) trigger makes a selection for each bunch crossing. It combines the different trigger elements into maximum 128 sub-triggers. Already for the first level trigger, track origin information is used to distinguish ep scattering events from background due to e.g. proton beam gas interaction. The

time-of-flight system is applied, the arrival time of the particles is compared and based on this information, it is decided whether the event is a physics event or not. Some of the events are then $prescaled$[2] and all events are compressed as to reduce the amount of storage needed. The prescaling is done for e.g. high statistic low Q^2 events, by weighting the events and letting one such entry represent a number of events. Trigger Level 2 (L2) is divided into the topological (L2TT) and neural networks triggers (L2NN). It takes in more detailed information and selects events according to more specified physics requirements than L1. The requirements are again increased as the Level 3 trigger (L3) is applied and L3 has an output rate of less than $50\ Hz$. The Level 4 trigger (L4) uses the information of the previous triggers, and at this stage a limited reconstruction of the event is made. Events are classified according to different criteria and are divided into different physics classes. A maximum input of $50\ Hz$ to the L4 trigger is allowed, as to avoid accumulating dead time, and the total dead time is normally kept close to $10\ \%$ under normal running conditions. After all the trigger requirements have been made, the original frequency of events given by the bunch-crossings has been reduced to an output rate of around $10\ Hz$.

[2]A prescale factor n will reduce the sub-trigger rate by the factor n, while every n:th event satisfying the sub-trigger conditions are kept.

Chapter 5

Jet Algorithm Study

Quarks and gluons have never been observed as free particles in nature, and the theory of quantum chromo dynamics (QCD) explains this through the confinement of colour charges. Partons, gluons and quarks, possessing colour charge can only exist in colourless combinations with other partons. Phenomenological models take us from the parton level, where interactions are calculable in QCD, to the hadron level, where the partons are manifested as collimated flows of hadrons, *jets*. Jets can not be unambiguously defined, but we can study the correlation between the kinematic properties of jets, reconstructed by jet algorithms, on different theoretical levels. A resolution measurement can also be made by studying the difference in properties, such as the jet energy and angular alignment, of jets found on different levels. In this way it is possible to evaluate the quality of the jet reconstruction made by different algorithms. The sensitivity of the reconstruction to changes in the resolution parameters and the dependence on the assumptions made regarding QCD scales may also be of importance when considering jet algorithm quality.

In this analysis, we investigate the effects of hadronisation in a generator model of inclusive and diffractive ep-scattering in the HERA kinematic region. First we compare the alignment and energy of Matrix Element level partons (*ME*) to jets reconstructed on the partonic final state, including parton showers (*PS*), (*ME+PS*). We then study the resolution of the jet kinematic quantities on hadron level (H), compared to the partonic initial state (*ME*) (the different levels are illustrated in fig. 5). Jet algorithms have been discussed briefly in section 2.5, and the five different algorithms used in the study will be described more extensively in section 5.1. Section 5.2 covers the different event samples and the selection of events made in the analysis. In section 5.3 we discuss what a quality measurement of a jet algorithm is, and give six criteria for how we define quality in this respect. The resolution of the jet reconstruction on different levels is studied in section 5.4. The reliability of the algorithms is further explored by taking into consideration the sensitivity to a change in the jet algorithm cut-off variable and the sensitivity to changes in the renormalisation and factorisation scales in NLO calculations. The conclusions of the study will be presented in section 5.5.

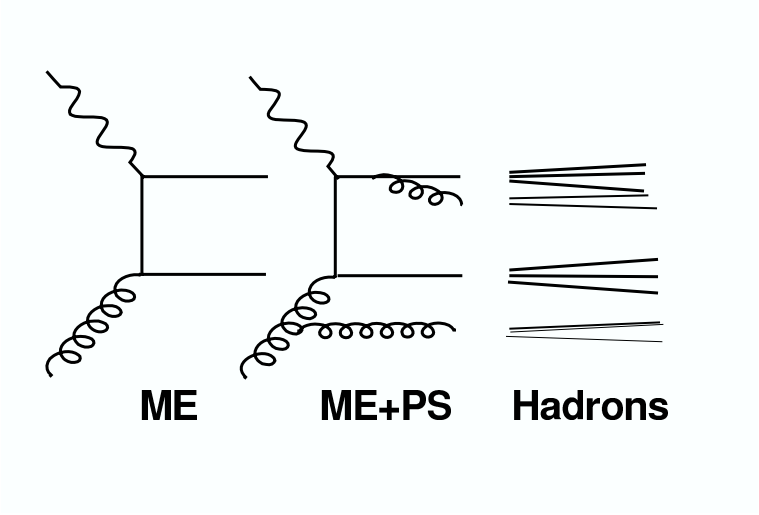

Figure 5.1: *Illustrative picture of the components belonging to the different theoretical levels investigated in this study. Matrix element level (ME) is defined from perturbative calculations, QCD radiation is added in the form of parton showers, approximating higher order emissions and defining the radiation level (ME+PS). Phenomenological models of hadronisation takes us to hadron level (H), where hadrons are grouped together as jets.*

5.1 Jet Algorithms

Jet algorithms start from individual particles, such as partons or hadrons, or assortments of such objects, defining *seed particles*, and combine these into prospective jets, *proto-jets*, through an iterative procedure. The iterations stop when the proto-jet properties are above a certain cut-off level, or when all particles belong to proto-jets. The remaining proto-jets satisfying any additional requirements, are selected as jets. Integral to the combination of particles into jets is the treatment of the *spectator jet*, in the HERA case the proton remnant jet, traveling down the beam-pipe.

The five jet algorithms investigated in this analysis can be divided into one *cone-type* and four *cluster-type* algorithms. Cone-type algorithms reconstruct jets by summing the momentum vectors of all particles within a cone of fixed size, thus directly applying the concept of defining a jet as a certain amount of energy concentrated within a certain region in solid angle. Resolution parameters for cone-type algorithms are typically the size of the cone and the amount of transverse momentum that must be found in the cone for a jet to be defined. In cluster-type algorithms, as first used by the JADE collaboration, particles are clustered together based on the invariant mass or momentum that combinations of particles have. This process continues until the mass of all objects that have been created in the clustering procedure is above a certain cut-off. The remaining objects are defined as jets.

We studied the *CDF-CONE* [45] algorithm, and the cluster algorithms, *JADE* [46, 47], *LUCLUS* [48], *DURHAM-k_T* [49], and the *Inclusive* $k_\perp$ algorithm [50, 51], the latter of which is

a cluster algorithm with a cone-type distance measure. The study is performed for low Q^2 inclusive scattering and for two different types of diffractive exchange, according to the resolved pomeron model (see section 3.4.1) and the production of a $q\bar{q}$ pair through 2-gluon exchange (see section 3.4.2). The different jet algorithms will be described in section 5.1.1-5.1.5 and the event samples used in section 5.2.

5.1.1 The CDF-CONE Algorithm

In an iterative procedure, the *CDF-CONE* algorithm [45], starts by summing the transverse momenta of all particles within a cone of radius, R, centred around a seed particle. The radius is defined in (η, ϕ)-space according to:

$$R = \sqrt{\Delta\eta^2 + \Delta\phi^2} \quad , \tag{5.1}$$

where $\Delta\eta$, and $\Delta\phi$, are ranges in pseudo-rapidity, η, and the azimuthal angle, ϕ, respectively. The centre of gravity of the summed particle momenta in such a cone is compared to the direction of the seed, and if these directions do not agree, the summed momenta becomes the seed of a new cone. The procedure is repeated until the jet direction of the cone momenta is the same as the direction of the seed[1] and the cone is considered a proto-jet. In the next step, the mid-points of all proto-jet pairs are taken as seed directions and the above procedure is repeated. This is done to discriminate against multiple jets being defined from a highly energetic group of particles, including multiple maximas, separated by distances between R and $2R$ in (η, ϕ)-space.

When the proto-jets have been defined according to the above procedure, a cut-off, $p_{T,min}$, is applied to separate out the jets. Particles belonging to more than one of these jets, through overlapping cones, are assigned to a single jet, and proto-jets with a large fraction of their transverse energy also included in more energetic jets are deleted. The remaining proto-jets then define the final set of jets found by the algorithm.

5.1.2 The JADE Algorithm

The *JADE* algorithm pairs together particles based on the invariant mass of the different pairs. The jet reconstruction starts by calculating a dimensionless distance parameter, y_{ij}, for all pairs of particles:

$$y_{ij} = \frac{m_{ij}^2}{W^2} = \frac{2E_iE_j}{W^2}(1 - \cos\theta_{ij}) \quad , \tag{5.2}$$

which is the invariant mass m_{ij} of a pair of (mass-less) particles or proto-jets, i and j, normalised with W^2. E_i and E_j are the energies of the two objects in question, and θ_{ij} is the angle between them. The pair with the smallest y_{ij} is combined into a single object according to a certain scheme. In this study, the E recombination scheme [52], where a new object is created by simply adding the proto-jet four-momenta, is used. Four-momenta are combined as to conserve energy

[1]The directions of cone and seed agree when the cone contains the same set of particles that the seed particle was created from in the previous iteration.

and momentum, and the procedure is repeated until all pairs have a normalised invariant mass greater than a cut-off, y_{cut}, defining the final jets.

The spectator jet in DIS, i.e. the proton remnant in ep scattering, is typically treated as a pseudo-particle in the clustering procedure. In the case of the proton remnant proceeding undetected down the beam-pipe, as in the HERA experiment, the pseudo-particle is added to account for its momentum.

5.1.3 The LUCLUS Algorithm

The clustering algorithm *LUCLUS*, is similar to the *JADE* algorithm, described above, but with a distance-measure d_{join}, based on particle momentum. The distance used is defined by:

$$d_{join}^2 = \frac{2(|\bar{p}_i||\bar{p}_j| - \bar{p}_i \cdot \bar{p}_j)|\bar{p}_i||\bar{p}_j|}{(|\bar{p}_i| + |\bar{p}_j|)^2} = \frac{2|\bar{p}_i|^2|\bar{p}_j|^2(1-\cos\theta_{ij})}{(|\bar{p}_i| + |\bar{p}_j|)^2} \quad , \tag{5.3}$$

where $\bar{p}_i$ and $\bar{p}_j$ are the (three-)momenta of particles i and j. For small angles between the particles, the distance-measure d_{join} may be considered the transverse momentum of particles i or j with respect to the direction given by summing up the four-momenta $\bar{p}_i$ and $\bar{p}_j$. If a proto-jet in the clustering procedure gets a smaller distance to a cluster belonging to another proto-jet, the proto-jets will be re-assigned. In this way, with every iteration, the particle groups are continuously clustered to the closest proto-jet. The clustering is stopped when d_{join} is larger than a cut-off d_{cut} for all proto-jet pairs.

So-called pre-clustering can also be applied, before the actual clustering of proto-jets begins, meaning a fast version of clustering is made, using a small value of d_{cut} in order to speed up the clustering process.

5.1.4 The DURHAM k_T Algorithm

The *DURHAM-k_T* algorithm uses the relative transverse energy of the particles as distance-measure in the clustering procedure. The procedure in DIS is to first do a pre-clustering of the hadrons into a spectator jet and a set of final state proto-jets. The distance, y_{ij}, between two proto-jets, i and j, is calculated:

$$y_{ij} = \frac{2(1-\cos\theta_{ij})}{E_T^2}\min(E_i^2, E_j^2) \quad , \tag{5.4}$$

where E_i and E_j are the energies of the proto-jets. E_T is a resolution parameter. The variable is scaled by the proto-jet transverse energy squared in the denominator, as to define a dimensionless cut-off variable. The distance, between each proto-jet i, and the beam jet p, is then calculated through:

$$y_{ip} = \frac{2(1-\cos\theta_{ip})}{E_T^2}E_i^2 \quad , \tag{5.5}$$

where θ_{ip} is the angle between the proto-jet and the beam direction, and E_i is the energy of the proto-jet i. The variables of the *DURHAM-k_T* algorithm are defined in the rest-frame of the exchanged boson[2], the $Breit\ frame$.

The clustering procedure continues by combining proto-jet i, with either proto-jet, j, or the spectator jet, p, depending on which is closest in distance. This means that if $y_{ij} < y_{ip}$, proto-jets i and j, are clustered together according to the E recombination scheme. If $y_{ip} < y_{ij}$, the proto-jet, i, is included in the beam jet, and disregarded from further clustering. The procedure is iterated, and when we require $y_{ij} > 1$, for all $i \neq j$, or $y_{ip} > 1$ the cut-off will be defined by the E_T parameter. When fulfilled, the proto-jet i is considered a final jet and removed from the iteration.

5.1.5 The Inclusive $k_\perp$ Algorithm

The *Inclusive* $k_\perp$ algorithm uses the jet transverse momentum, p_T, as distance measure, and is like the DURHAM-k_T algorithm executed in the Breit frame. Using this quantity, we define the "size" of each proto-jet:

$$d_i = p_{T,i}^2 \quad , \tag{5.6}$$

where $p_{T,i}$ is the transverse momentum of proto-jet i. The algorithm works according to a clustering scheme, but it is also in some sense cone-like. The distance, d_{ij}, between two proto-jets, i and j is calculated through:

$$d_{ij} = \min(p_{T,i}, p_{T,j})^2 R_{ij}^2 / R^2 \quad , \tag{5.7}$$

where a radius parameter, defined in (η,ϕ)-space:

$$R_{ij}^2 = (\eta_i - \eta_j)^2 + (\phi_i - \phi_j)^2 \quad , \tag{5.8}$$

is included. The variables η_i and ϕ_i are the pseudo-rapidity and azimuthal angle of proto-jet i. The constant R, is a resolution parameter, which in this study is consistently set to $R = 1$.

The clustering procedure works by comparing the distances d_i and d_{ij}. Characteristic for the *Inclusive* $k_\perp$ algorithm is that no particles are excluded from the clustering, but all final state objects are clustered into proto-jets. Proto-jet i is then clustered with proto-jet j, if distance d_{ij}, is smaller than d_i. When d_i is smaller than d_{ij}, for all $i \neq j$, it is closer to the proton remnant than to any proto-jet j. It is then not added to the spectator jet but defined as a jet and taken out of the clustering procedure. The merging of two proto-jets is done according to the p_T-weighted scheme [53], meaning the objects are merged by adding the p_T of the different particles, and the direction of the new object in the η and ϕ plane is calculated as a p_T weighted average of the original objects. The procedure is iterated, merging adjacent pairs of proto-jets to each other, thus continuously clustering proto-jets of increasing p_T. Using the p_T of the jets as cut-off variable, a cut on the minimum transverse momentum, $p_{T,min}$, can be defined, and applied to the jets given by the algorithm.

[2]In the Breit frame, the exchanged boson has four-momenta $q = (0, 0, 0, -Q)$

5.2 Event Characteristics and Generation

The event samples used in this study have been created using the RAPGAP 2.06 [20] Monte Carlo generator. RAPGAP is known to describe both inclusive and diffractive DIS at HERA well. Our primary interest was to investigate the algorithms with respect to $\mathcal{O}(\alpha_s)$ processes, which produce *(2+1) jet* events. This type of events are of importance both to inclusive and diffractive processes. In the inclusive case e.g. di-jet rates can be used for studying the underlying parton dynamics and in providing information on what type of evolution is required to describe them at low values of Bjoerken-x. In diffractive scattering, di-jet events can be used to discriminate between different diffractive models. A good jet resolution is of course needed in both cases, as to make reliable measurements. The dependence of the jet resolution on the jet cut-off variable is also worth studying since applying a high cut-off generally limits the event statistics. Studying *(2+1) jet* events gives us the chance of comparing the jet properties with those of the hard partons from the matrix elements, and thereby study the general performance of the different algorithms, with regard to how the properties of the matrix element partons are reconstructed, and what effects and errors enter on different levels.

QCD radiation is added according to the DGLAP formalism (see section 2.3.2), using parton showers (see section 2.4.1), and the hadronisation process is carried out according to the Lund string model (see section 2.4.3) as implemented in *JETSET* [54].

The generation of diffractive events was made using two different models describing the interaction, the first based on the exchange of a phenomenological pomeron according to the Ingelman-Schlein model (previously discussed in section 3.4.1), and the second on perturbative QCD calculations of a 2-gluon exchange $q\bar{q}$ production process (discussed in section 3.4.2). This will allow us to study two characteristically different ways of modelling diffraction. When diffraction takes place through the exchange of a resolved pomeron, a pomeron remnant is expected, and it may contribute to the jets in the di-jet pair. In a diffractive $q\bar{q}$ production process, mediated by 2-gluon exchange, the two gluons couple directly to the $q\bar{q}$ pair and are not expected to give rise to a remnant. This is something to take into consideration, as a possible pomeron remnant would be of interest to study, and since differences in the jet reconstruction may occur depending on the type of exchange that mediates the diffractive process. Also, different jet algorithms may treat the contribution to jets from the pomeron remnant differently.

The study presented here is performed on low Q^2, inclusive and diffractive scattering. High Q^2 inclusive scattering has also been studied and was presented in [55]. The event samples for the diffractive study contains exclusively diffractive DIS, and for an unambiguous definition of the diffractive processes, the kinematic range must be limited to $x_{I\!P} < 0.01$, which generally is fulfilled at low Q^2. BGF and QCD-Compton scattering has also been studied separately.

With $E_e^{'}$ denoting the energy of the scattered electron, $\theta_e^{'}$ its polar angle, and y being the Bjoerken scaling variable, the phase space of the analysis is for all samples defined by the cuts:

- $Q^2 > 5$ GeV^2
- $E_e^{'} > 11\ GeV$

- $153° < \theta_e{}' < 177.5°$
- $y > 0.05$

These cuts are applied to ensure that the positron is contained within a well-defined phase space, corresponding to the H1 SpaCal acceptance on detector level. A beam-pipe cut is also made as to take into consideration the scattered proton travelling down the beam-pipe in a typical HERA event.

For the resolved pomeron diffractive sample, we have used the H1 parametrisation of $F_2^{D(3)}$ in terms of the parton distributions of the pomeron, applying fit 2, mentioned in section 3.3 and described in [36].

When comparing hadron level jets to matrix element partons we demand exactly two jets on both parton and hadron level in our final event sample. This means that we require the generator to produce two hard partons and that two jets are reconstructed by the jet algorithm on hadron level. A comparison is then carried out between the two parton level jets and the two hadron level jets. The separate jets on the different levels are related to each other based on their position in rapidity, identifying the most forward (large positive rapidity) and backward (small positive or negative rapidity) jets on both levels. This enables us to study the jet behaviour in different regions of rapidity. To protect us further from relating the wrong jets on the different levels, we also require that parton and jet are correlated in ϕ. And, in studying different cut-offs, we require that the p_T cut-off on the reconstructed jet never is below the p_T cut-off present in the matrix element parton calculations, since an uncertainty enters into the these calculations as they diverge at low p_T.

The factorisation and renormalisation scales used in the generation were set to $Q^2 + p_T^2$, and the matrix element hard parton p_T^2 cut-off is consequently set to $4\ GeV^2$. The p_T^2 scale will become more dominant the lower the value of Q^2 is. The p_T of the partons is typically peaked at the cut-off value, and the scale dependence on p_T will become less important as Q^2 increases.

A check of the sensitivity to changes in the factorisation and renormalisation scales was done through the use of the Next to Leading Order (NLO) event generator $DISENT$ [56]. This program perturbatively calculates the hard parton matrix elements for $\mathcal{O}(\alpha_s^2)$ standard DIS processes. We produce event samples for two different choices of the scale settings and study the dependence of the 2-jet rate on the choice of the scale.

5.3 Jet Algorithm Quality

A jet algorithm may, most generally, be considered a method for defining jets. There is no 'right' jet algorithm, if we do not further explain what requirements we want such an algorithm to fulfill. The same is true when talking about the quality of a jet algorithm. We must specify what we mean by 'quality', in order to make an assessment of a jet algorithm in this respect, or compare the ability of one algorithm to reconstruct jets with that of another. This in turn is dependent

on the analysis one wants to use the algorithm for and different algorithms have also been constructed specifically for different kind of experiments.

However, there are certain criteria that one may in many instances consider important. Most typically, we want there to be a correlation between the kinematic properties of jets on different levels. Our main task is to study the agreement between partons and hadron level jets for the different algorithms in inclusive and diffractive HERA ep scattering and provide a judgment of their performance. We also compare matrix element partons with partons after QCD radiation (parton shower level). The treatment of hadronisation is studied separately, comparing parton shower level to hadron level jets. In order to make our assessment of the different algorithms as well-defined as possible, we have set up the following criteria for what a good jet algorithm reconstruction is:

1. Small difference between the generated invariant mass of the hard subsystem and the corresponding reconstructed mass after QCD radiation, and also on hadron level.

2. The direction of motion of the matrix element partons and the corresponding reconstructed jets after QCD radiation, and also at hadron level, should be correlated.

3. Small hadronisation corrections for the jet directions and reconstructed invariant masses of the di-jet subsystem.

4. Small dependence of the jet reconstruction on whether we are measuring an inclusive DIS or an exclusive diffractive process, or on the type of model used for diffraction, for the relations in 1, 2 and 3.

5. Small dependencies on the resolution parameters of the jet algorithm for the relations in 1, 2 and 3.

6. Small dependence on the factorisation and renormalisation scales in NLO calculations.

In order to study the alignment between the jets on different levels in accordance with requirement $1-3$, we calculate the mean of the absolute deviations in angular, (η, ϕ), space and in the energy, $(p_T, \sqrt{\hat{s}})$ phase space, of the selected jets at different levels. A mean distance in (η, ϕ) space is defined according to:

$$< \Delta(\eta\phi) >= \sqrt{< \Delta\eta >^2 + < \Delta\phi >^2} \quad , \tag{5.9}$$

where

$$\Delta\eta = |(\eta_{true} - \eta_{reco})| \quad , \tag{5.10}$$

and

$$\Delta\phi = |(\phi_{true} - \phi_{reco})| \tag{5.11}$$

Similarly, we define an energy-related mean distance using p_T and $\hat{s}$:

$$< \Delta(p_T, \sqrt{\hat{s}}) >= \frac{< \Delta p_T > + < \Delta\sqrt{\hat{s}} >}{2} \quad , \tag{5.12}$$

where

$$\Delta p_T = |(p_{T,true} - p_{T,reco})/p_{T,true}| \quad , \tag{5.13}$$

and

$$\Delta\sqrt{\hat{s}} = |(\sqrt{\hat{s}}_{true} - \sqrt{\hat{s}}_{reco})/\sqrt{\hat{s}}_{true}| \quad , \tag{5.14}$$

where the index $reco$ refers to the level at which the jets have been reconstructed, and $true$ to the lower level which we compare to. With resolution we mean the ability to resolve the underlying structure of the events on different levels. A good resolution corresponds to small values in $< \Delta(\eta\phi) >$ and $< \Delta(p_T, \sqrt{\hat{s}}) >$.

We also measure the systematic deviation of the different quantities, η, ϕ, p_T and $\sqrt{\hat{s}}$ separately:

$$< \delta\eta >=< (\eta_{true} - \eta_{reco}) > \tag{5.15}$$

$$< \delta\phi >=< (\phi_{true} - \phi_{reco}) > \tag{5.16}$$

$$< \delta p_T >=< (p_{T,true} - p_{T,reco})/p_{T,true} > \tag{5.17}$$

$$< \delta\sqrt{\hat{s}} >=< (\sqrt{\hat{s}}_{true} - \sqrt{\hat{s}}_{reco})/\sqrt{\hat{s}}_{true} > \tag{5.18}$$

This is done to obtain an understanding of systematic shifts between different levels. For example, if the proton remnant in standard DIS, or the pomeron remnant for diffractive DIS adds string effects, a systematic deviation between the properties of partons and jets reconstructed on hadron level may be observed.

All quantities in our study, except $\hat{s}$, are derived from the properties of individual jets. The quantities will however be presented as the mean value of the two jets required on the different levels. Large differences in resolution between the most forward and backward jet will therefore be noted separately.

The study is made for 10 different cut-off settings, shown in table 5.1, chosen as to give a similar *(2+1)* jet rate for the corresponding setting between the different algorithms. The results will be presented in diagrams of ten bins, where each bin represents one setting, for which the mean resolution of the jets reconstructed is given.

Setting	I	II	III	IV	V	VI	VII	VIII	IX	X
CDF-CONE	2.5	2.9	3.25	3.75	4.25	4.9	5.5	6.25	7.0	10.0
Incl. $k_\perp$	2.0	2.25	2.5	3.13	3.75	4.4	5.0	5.75	6.5	10.0
k_T	3.3	3.6	3.9	4.4	4.7	5.4	5.9	6.5	7.1	9.5
JADE	0.013	0.015	0.022	0.026	0.030	0.034	0.042	0.046	0.050	0.070
LUCLUS	4.0	4.25	4.5	5.0	5.5	6.3	7.0	7.75	8.5	10.0

Table 5.1: *The settings used for the five different algorithms of the study. The resolution parameters of all algorithms except the JADE algorithm are energy quantities defined in GeV. The JADE parameter, y_c, is dimensionless.*

Continuing with criterion 4, the resolution of a good algorithm with regard should have little dependence on the type of process we measure. If we are interested in comparing inclusive and diffractive scattering, or distinguishing between different diffractive models using jets, the reconstruction in the different cases needs to be carried out with similar accuracy independent of what physics scenario is being reconstructed. Otherwise, meaningful comparisons can not be made, and possible physics differences will be distorted.

Investigating the jet reconstruction with respect to criterion 5, we study the change in the systematic shift of the reconstruction resolution between different levels. If the systematic shift of the resolution provided by the jet algorithm differs between different levels, it will mean that an error is introduced to the reconstruction when the cut-off is applied. This is of particular importance when considering the smearing of the detector, which will induce an additional error if this is the case.

Criterion 6 is made with respect to inclusive processes in Next to Leading Order (NLO) calculations. The factorisation and renormalisation scales are in principle unknown, and changes in the jet properties of a generated sample depending on these scales means an introduction of systematic errors into the reconstruction. A good algorithm is hence one that shows little sensitivity in this respect.

5.4 Jet Reconstruction Performance

We first investigate the jet reconstruction properties as described by the variables defined in eq. (5.9) and (5.12) according to the four first criteria we have set in section 5.3. A good reconstruction of the partons on different levels i.e. a good resolution in angle and energy will be represented by a small value of these variables. In section 5.4.1 we study the effects of adding parton showers to the matrix element partons, i.e. without applying hadronisation. This should give us a general idea of how the algorithms behave in combining objects together, and of how emitted gluons are treated by the algorithms. The effects of hadronisation are studied in section 5.4.2, where we compare the matrix element partons to jets reconstructed from hadrons in order to see how well the hard parton properties are reconstructed on hadron level. Before that

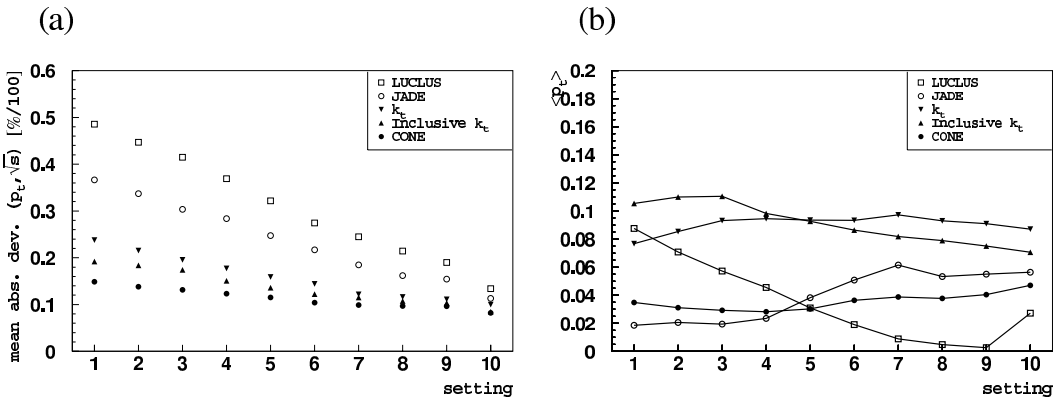

Figure 5.2: (a) *The mean absolute deviation in* $(p_T, \sqrt{\hat{s}})$ *and* (b) *The mean systematic shift in* p_T*, between the matrix element partons and the corresponding jets on the hadron level, for the inclusive RAPGAP sample, as a function of the setting used in the algorithm, seen in table 5.1. The same* p_T *cut is applied on the matrix element parton as is made in the CDF-CONE algorithm. The CDF-CONE algorithm* p_T *cut was also made on the jets reconstructed by all algorithms on hadron level.*

however, we look separately at the effects of hadronisation, comparing hadron level to parton shower level jets. This will provide us information on the sensitivity of the jet algorithms to hadronisation. Hadronisation is expected to worsen the resolution of the reconstruction and to cause an increase in the values of the variables in eq. (5.9) and (5.12). As stated in criterion 4, the differences in the reconstruction between different models, in these comparisons, will be noted. The sensitivity of the different algorithms to changes in the cut-off, according to criterion 5 is discussed in section 5.4.3. Furthermore, we study the sensitivity of the jet reconstruction to changes in the renormalisation and factorisation scales according to criterion 6 in section 5.4.4.

Comparing the reconstructed jets and matrix element partons, it should be noted that a cut-off is already made on the p_T of the hard partons in the event generation, and that no cut-offs corresponding to those made in the jet algorithms on other levels will be added on matrix element level. When jet reconstruction is performed on parton shower level and hadron level, it is not possible to find a cut corresponding to the matrix element p_T cut for all algorithms. In fig. 5.2.a the p_T cut made on the final proto-jets in the *CDF-CONE* algorithm has been applied on the matrix element partons for the plot of the average absolute deviation in p_T and $\sqrt{\hat{s}}$, $< \Delta(p_T, \sqrt{\hat{s}}) >$, as a function of the respective jet algorithm cut-offs. The corresponding systematic shift in p_T is shown in fig. 5.2.b. The resolution of the jets increases with the hardness of the partons i.e. with higher cut-offs, which is the expected behaviour. The consequence of not applying any cut on the matrix element partons, is that partons with a very low p_T may, after parton showering or hadronisation, be reconstructed as jets with a comparatively large p_T. This will lead to a worsened resolution with higher cut-offs, compared to the case where an additional cut on the hard partons is applied, since the minimum p_T of the jets increases with the cut-off, while the p_T cut for the matrix element partons remains at a constant low value.

We also study the contribution of the systematic shift of the reconstruction as expressed in

eq. (5.15-5.18). The main contribution to the absolute mean deviation generally comes from the spread (RMS) of the distributions. This is however not always the case, for the different samples and algorithms. It will be noted when the systematic shift is large and has a big impact on the final result.

5.4.1 From Matrix Element Partons to Partonic Final State Jets

By comparing matrix element partons and partons after QCD radiation, we investigate the effects of parton emissions on the reconstruction of the hard parton properties. This also gives us the most basic way of comparing how the reconstruction is carried out in different processes and models. A good algorithm would group together the matrix element hard partons with the emitted partons such that the properties of the jets on radiation level correspond to those of the matrix element partons. It would produce two jets after radiation, that are close in (η, ϕ) space to the two hard partons, and for which the invariant mass $\sqrt{\hat{s}}$ after radiation is equal to the invariant mass of the hard partons, as stated in criterion 1 and 2 above, and it would do that independently of what type of process is being studied, according to criterion 4.

If we were to apply the jet algorithms already on the matrix element hard partons (without radiation added) the description by the jets of the hard parton properties would obviously become very exact. When including radiation however, the properties of the jets reconstructed will not directly reflect the hard parton properties, but the nature of the algorithm will determine to what extent the reconstructed jets describe these properties.

The mean of the absolute deviation in η and ϕ, $< \Delta(\eta\phi) >$, between the matrix element partons and the partons after radiation is plotted in fig. 5.3.a (inclusive sample), 5.3.b (resolved pomeron sample) and 5.3.c (2-gluon exchange sample), as a function of the setting of the algorithms given in table 5.1. The different algorithms all exhibit a deviation in $(\eta\phi)$ that is below 0.3 units, for the inclusive sample and for both diffractive models. We see that the deviation is similar for the inclusive sample and the resolved pomeron model diffractive sample for most algorithms, but slightly lower in the latter. The *JADE* and *LUCLUS* algorithms show a worse resolution than the *DURHAM-k_T*, the *CDF-CONE* and the *Inclusive $k_\perp$* algorithms for the different cut-off settings. The latter three are below a deviation of 0.2 units for all cut-offs, with the *Inclusive $k_\perp$* performing best for both the inclusive and the resolved pomeron sample. For 2-gluon exchange model $q\bar{q}$ production, the deviation is even lower. Especially the *LUCLUS* and *JADE* algorithms show a dependence on which type of diffractive model we are investigating in this regard. This may be due to the treatment of the remnant particle, that is present in the resolved pomeron but not in the 2-gluon exchange case, where we have a "pure" rapidity gap. Like for the other samples however, the *Inclusive $k_\perp$* and *CDF-CONE* algorithms provide the best resolution also for 2-gluon exchange diffraction. The *DURHAM-k_T* and *LUCLUS* give a similar reconstruction in the 2-gluon case, and the *JADE* algorithm shows the worst performance. We also note that there is no dramatic dependence on the cut-off when comparing parton shower level jets and matrix element partons. Sometimes the resolution becomes worse with an increased cut-off, possibly due to non-equal cut-off values for matrix element and parton shower level as discussed previously.

The mean of the absolute deviation of $< \Delta(p_T, \sqrt{\hat{s}}) >$ between the matrix element par-

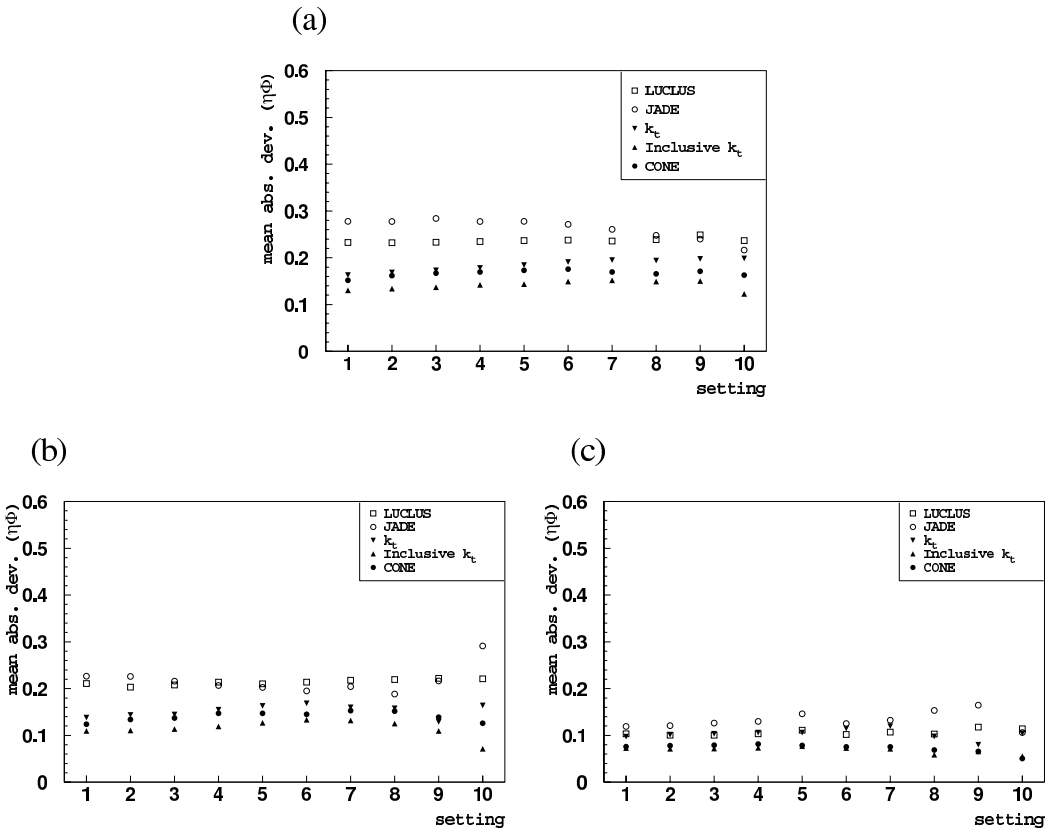

Figure 5.3: *The mean absolute deviation between the matrix element partons and the corresponding jets at the parton shower level in* (η, ϕ) *space for* (a) *the inclusive sample,* (b) *the diffractive resolved pomeron sample, and* (c) *the diffractive 2-gluon* $q\bar{q}$ *production sample, as a function of the setting used in the algorithm seen in table 5.1.*

tons and the partons after radiation is plotted in fig. 5.4.a-5.4.c, as a function of the setting of the algorithms given in table 5.1. It is continuously below 30% for all algorithms and all different samples. The *DURHAM-*k_T, the *CDF-CONE* and the *Inclusive* $k_\perp$ algorithms provide descriptions with deviations below 15% for most settings for both the inclusive and the resolved pomeron samples. The *LUCLUS* and *JADE* algorithms, as for (η, ϕ), reconstruct the jets with consistently larger differences between matrix element and parton shower level, particularly for lower cut-offs. In the inclusive and resolved pomeron samples, both *LUCLUS* and *JADE* exhibit comparatively large shifts in $\sqrt{\hat{s}}$ (see fig. 5.5.a and fig. 5.5.b). A shift in p_T is also apparent in the *LUCLUS* reconstruction (see fig. 5.6 for the inclusive case). The other algorithms seem unaffected by this, and in particular the *Inclusive* $k_\perp$ algorithm shows no such deviation. The occurrence of these deviations may be due to the inclusion of energetic forward-going partons, relating to the proton remnant and pomeron remnant, in the jets. The *JADE* algorithm shows a dependence when investigating different processes and models, especially for lower cut-offs.

In summary, when studying the resolution in the variables defined in eq. (5.9) and (5.12), between the matrix element partons and jets reconstructed after partonshowering, the *DURHAM-*k_T, the *Inclusive* $k_\perp$, and the *CDF-CONE* algorithms give small deviations between the two

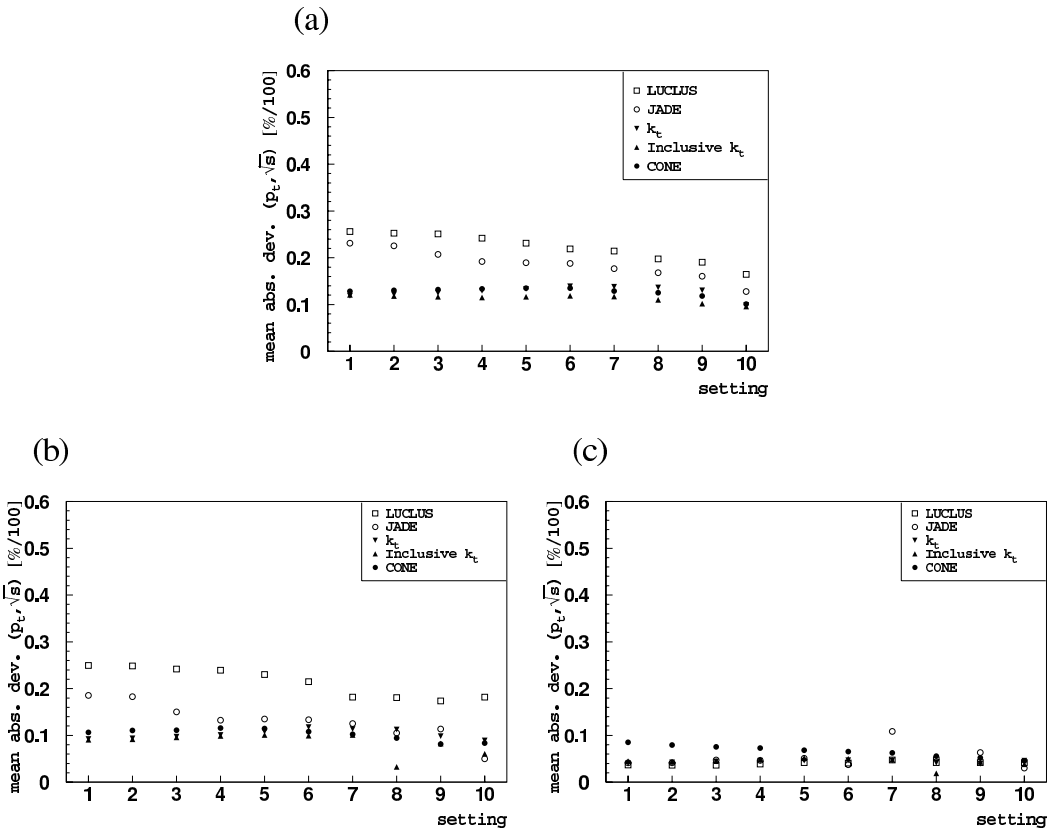

Figure 5.4: *The mean absolute deviation between the matrix element partons and the corresponding jets at the parton shower level in* $(p_T, \sqrt{\hat{s}})$ *space for* (a) *the inclusive sample* (b) *the diffractive resolved pomeron sample* (c) *the diffractive 2-gluon* $q\bar{q}$ *production sample, as a function of the setting used in the algorithm seen in table 5.1.*

levels compared. The *Inclusive* $k_\perp$ often gives the better performance. The *JADE* and *LUCLUS* algorithms show larger deviations in both angular and energy reconstruction and have systematic shifts in the reconstruction of energy. The *JADE* and *LUCLUS* reconstruction also has the largest dependence on the type of process studied.

5.4.2 From Matrix Element Partons to Hadron Level Jets

When comparing matrix element partons to hadron level jets, both the effects of parton showers and hadronisation are included in the jet reconstruction. A good jet algorithm would, according to criterion 1, 2 and 3, be one for which there is an correlation between the matrix element and hadron level jet p_T, energy directions, and one for which hadronisation adds small effects to the jet direction and energy, at the same time showing small dependencies on the process reconstructed.

We first study the hadronisation separately, comparing hadron level to parton shower jets, as shown for (η, ϕ) in fig. 5.7.a-5.7.c. Here we see how the harder cuts of the higher settings contribute to a better resolution in the jet reconstruction. In (η, ϕ) space, the decrease in reso-

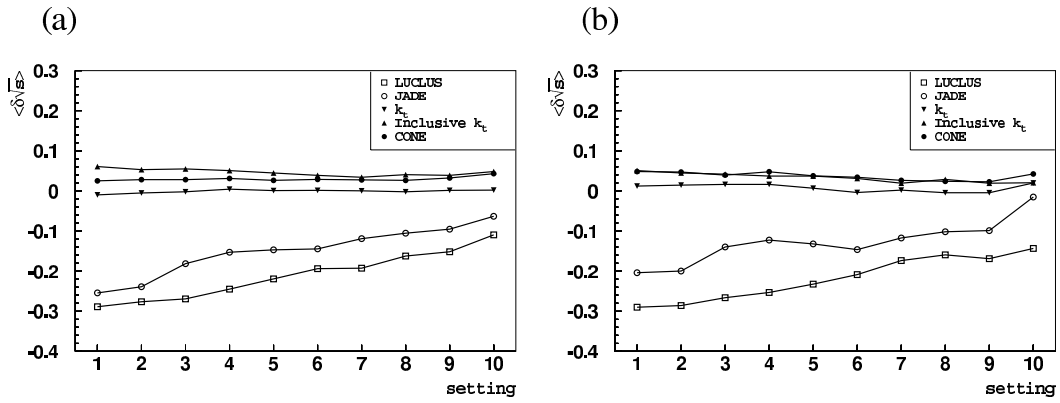

Figure 5.5: *The mean systematic shift between the matrix element partons and the corresponding jets at the parton shower level in $\sqrt{\hat{s}}$ for (a) the inclusive sample, and (b) the diffractive resolved pomeron sample, as a function of the setting used in the algorithm seen in table 5.1.*

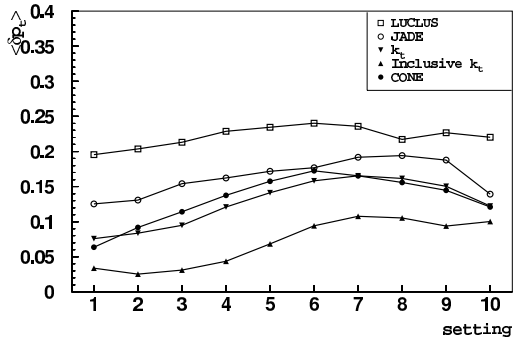

Figure 5.6: *The mean systematic shift between the matrix element partons and the corresponding jets at the parton shower level for p_T, for the inclusive sample as a function of the setting used in the algorithm seen in table 5.1.*

lution due to hadronisation goes from 0.2-0.3 units for a lower jet algorithm cut-off, to 0.1-0.2 units and below for higher settings. This is true both for the inclusive, the resolved pomeron and 2-gluon diffractive samples. Also notable is that there are no great differences in the treatment of hadronisation between the different jet algorithms. A shift in η can however be observed for the *CDF-CONE* algorithm in the inclusive and the resolved pomeron case (see fig. 5.8.a and fig. 5.8.b). When investigating QCD-Compton and BGF processes separately, there are differences in the shifts between the two different type of processes, which could indicate a string effect, where different string configurations contribute differently to the jet reconstruction (see fig. 5.8.c and 5.8.d for the inclusive case, the behaviour for resolved pomeron model diffraction is similar). For 2-gluon $q\bar{q}$ production a shift in η can be observed for all algorithms when studying the jets individually (see fig. 5.9.a for the forward and 5.9.b for the backward jet). String effects are not expected to be large in 2-gluon exchange, and these shifts may be due to standard hadronisation effects.

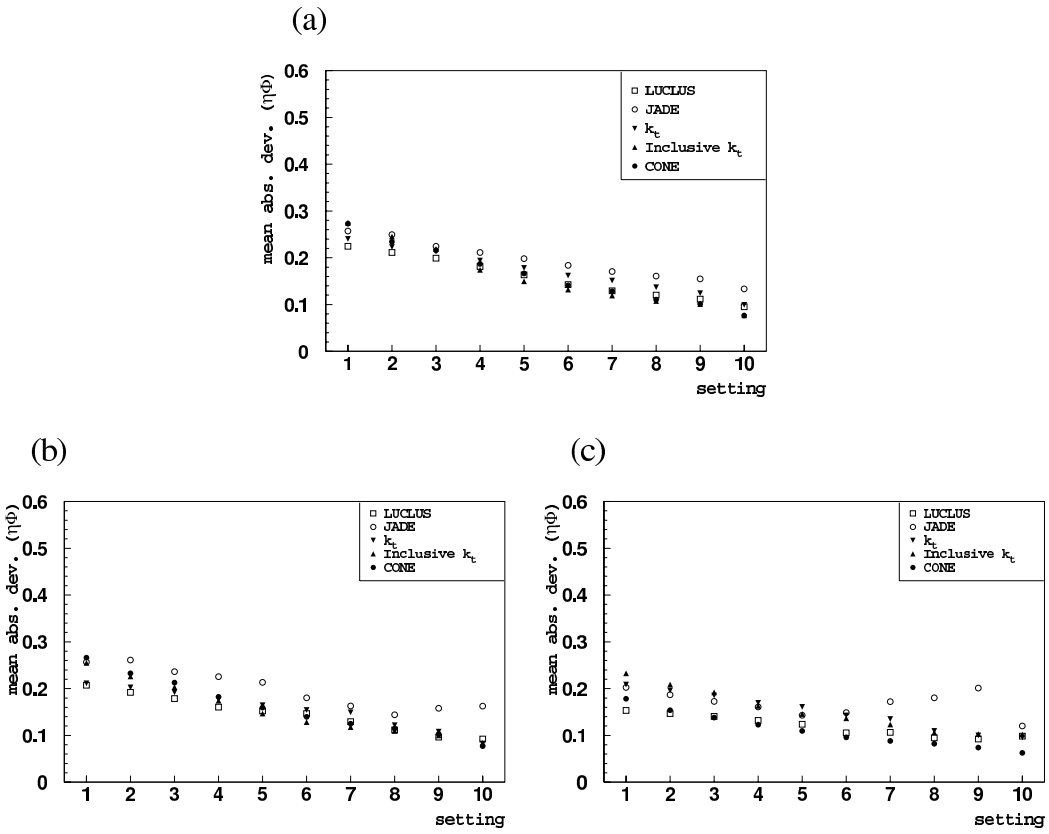

Figure 5.7: *The mean absolute deviation between the final state partons and the corresponding jets at the hadron level in* (η, ϕ) *space for* (a) *the inclusive sample* (b) *the diffractive resolved pomeron sample* (c) *the diffractive 2-gluon* $q\bar{q}$ *production sample, as a function of the setting used in the algorithm seen in table 5.1.*

In $(p_T, \sqrt{\hat{s}})$, as shown in fig. 5.10.a-5.10.c, the picture is quite similar. Hadronisation is treated with little differences in resolution between the algorithms studied, the deviation is typically between $10 - 20\%$ for lower settings and $5 - 10\%$ for higher settings, for the inclusive and resolved pomeron sample. The *CDF-CONE* algorithm however generally performs best. For the 2-gluon sample the resolution of the *Inclusive* $k_\perp$ algorithm is roughly at the same levels as for the inclusive and the diffractive resolved pomeron sample, while the *DURHAM-*k_T algorithm and the *CDF-CONE* algorithm perform a bit better than before. The *LUCLUS* and *JADE* algorithms here however show a resolution of around 5% also for lower settings and apparently treats the hadronisation in this sample differently from that in the inclusive and resolved pomeron sample.

Comparing jets reconstructed on hadron level to matrix element partons, hadronisation effects is added compared to the parton shower level reconstruction (see sec. 5.4.1), and the resolution of the reconstruction of the hard parton properties is expected to worsen. The jet algorithm performance for the reconstruction of the hard subsystem on hadron level is presented in fig. 5.11 and 5.12.

The results for (η, ϕ) are presented in fig. 5.11.a-5.11.c. No large differences in the recon-

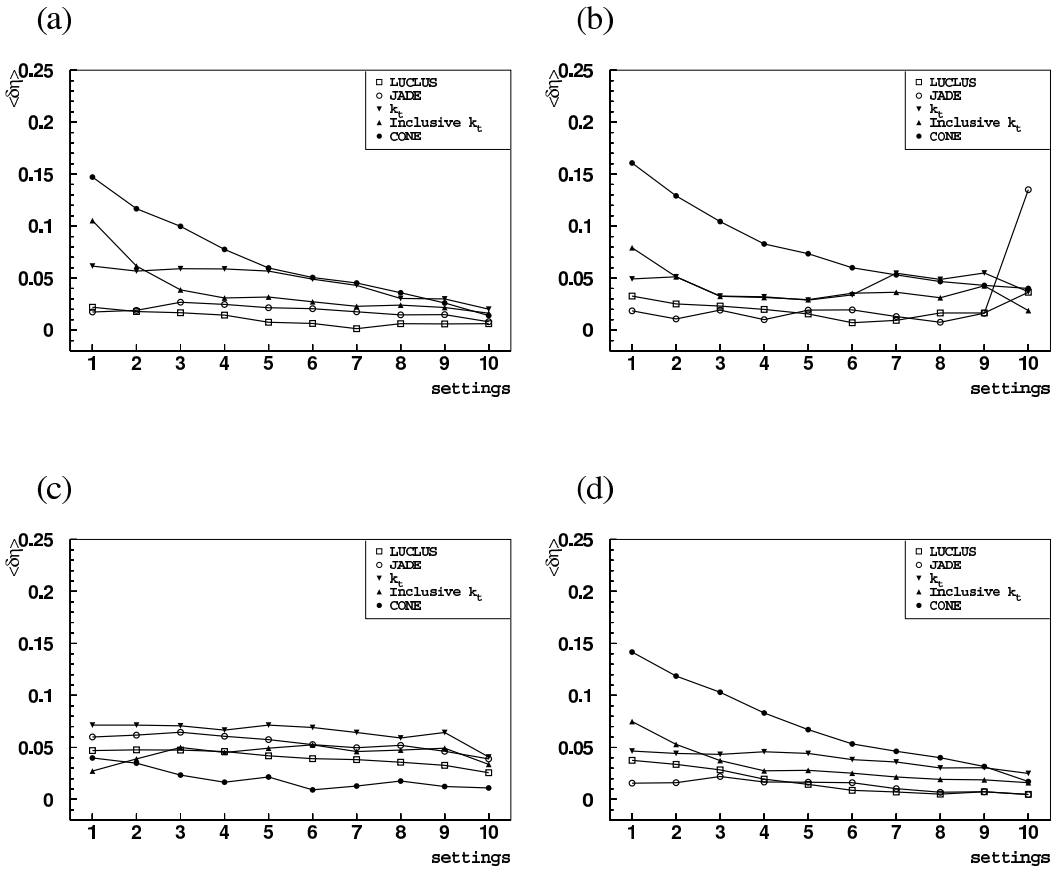

Figure 5.8: *The mean systematic shift between the final state parton and hadron level jets in* η *for* (a) *the inclusive sample* (b) *the diffractive resolved pomeron sample,* (c) *the inclusive QCD-Compton process sample (d) the inclusive BGF process sample, as a function of the setting used in the algorithm seen in table 5.1.*

struction appear for the different algorithms. The *JADE* algorithm however generally performs worst, and the *Inclusive* $k_\perp$ in many cases performs the best. The resolutions stay below 0.3 units in $< \Delta(\eta\phi) >$ for most settings, with an increased cut-off leading to an improved resolution. The deviations are a bit smaller for the diffractive resolved pomeron model sample than the inclusive one, but with a similar process dependence for the different algorithms, and with the *JADE* algorithm being most affected. The resolution of jets reconstructed from the 2-gluon sample is here similar to that of the jets in the other samples, in contrast to what was seen in section 5.4.1. For the inclusive and resolved pomeron samples, the shifts of the jets make up only a small part of $< \Delta(\eta\phi) >$. The contribution to the shift in the 2-gluon exchange sample $< \Delta(\eta\phi) >$ is larger but similar between the different algorithms.

When studying the resolution in $(p_T, \sqrt{\hat{s}})$, as shown in fig. 5.12.a-5.12.c, by comparing matrix element partons with jets reconstructed on hadron level, differences in the reconstruction of the algorithms become more visible than when studying the alignment in direction. The *JADE* algorithm shows an absolute deviation of above 50% for lower cut-off values, and the *LUCLUS* algorithm of around 40%. Going to higher cut-off values, the resolution becomes below 40% for

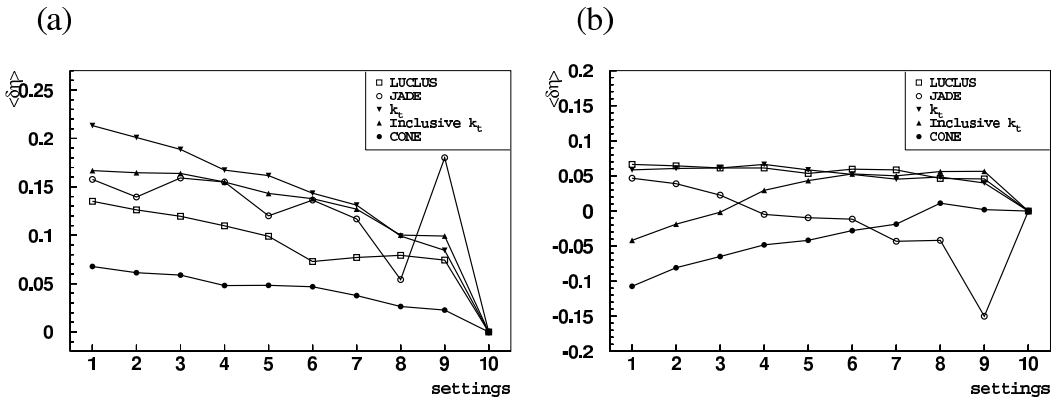

Figure 5.9: *The mean systematic shift between the final state parton and hadron level* (a) *forward jets,* (b) *backward jets, for* η *for the 2-gluon* $q\bar{q}$ *sample as a function of the setting used in the algorithm seen in table 5.1.*

the inclusive sample. *JADE* behaves better for the resolved pomeron diffractive sample, while *LUCLUS* still has an absolute deviation close to 50% for lower settings. These deviations are largely induced by significant shifts in $\sqrt{\hat{s}}$ and p_T for both *LUCLUS* and *JADE* in the inclusive and resolved pomeron case. These shifts could, as noted when studying parton shower level jets, be caused by the inclusion of particles related to the proton or pomeron remnant in the jets, and this effect is enlarged by hadronisation, compared to what is seen at parton shower level (see section 5.4.1). The reconstruction of jets by the *Inclusive* $k_\perp$ and the *CDF-CONE* algorithm, with deviations around or below 20%, seems unaffected by this. They both include a radius dependent selection, possibly leading to an exclusion of the remnant particles. The *DURHAM-*k_T algorithm however also does not show any great shifts in these quantities. We also note that in the inclusive and resolved pomeron case, an increase in cut-off seems to have little influence on the resolution of these three algorithms. A model dependence in the jet resolution can be seen for the *JADE* and *LUCLUS* algorithms, For the 2-gluon exchange sample, the algorithms provide jets with a resolution that is between $5 - 10\%$ for all settings, differing greatly from the inclusive and resolved pomeron case. The resolution of the *Inclusive* $k_\perp$, the *DURHAM-*k_T and the *CDF-CONE* algorithm here show a greater dependence on the value of the jet algorithm cut-off applied than what was the case for inclusive or resolved pomeron scattering, thus also in the 2-gluon case showing a certain dependence on the kind of model we are investigating. The *LUCLUS*, especially for higher settings, shows a dependence also on whether we are investigating an inclusive or resolved pomeron sample.

In summary, the hadronisation is handled similarly for the different algorithms, and between the different samples, though the *JADE* algorithm is particularly affected. The resolution improves with an increase in the cut-off. The *CDF-CONE* algorithm jets gain a shift in η as hadronisation is applied, possibly due to string effects. Comparing hadron level jets to matrix element partons, the *JADE* and *LUCLUS* reconstruction of energy is poor, largely due to shifts in p_T and $\sqrt{\hat{s}}$, induced on the parton shower level. The differences between samples are often smaller on hadron level than on parton shower level, but *JADE* and *LUCLUS* clearly show different characteristics depending on the type of process investigated. This may, as noted in 5.4.1, be due to the

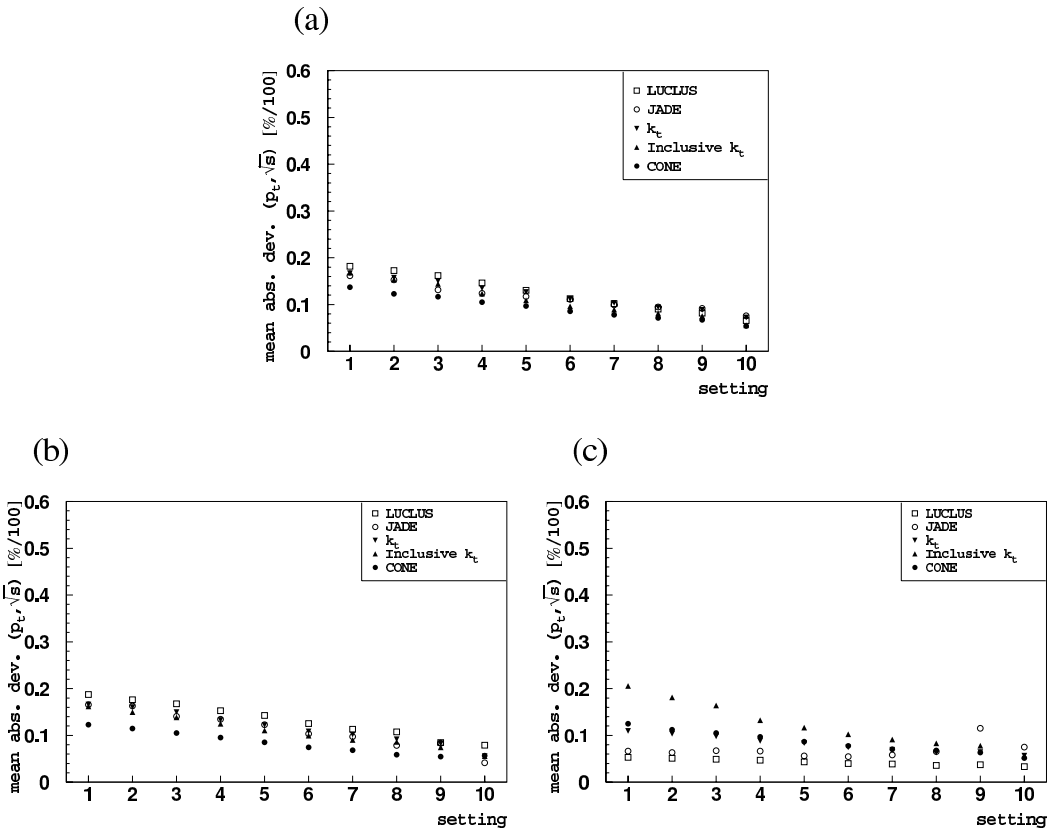

Figure 5.10: *The mean absolute deviation between the final state parton jets and the corresponding jets at the hadron level in* $(p_T, \sqrt{\hat{s}})$ *space for* (a) *the inclusive sample* (b) *the diffractive resolved pomeron sample* (c) *the diffractive 2-gluon* $q\bar{q}$ *production sample, as a function of the setting used in the algorithm seen in table 5.1.*

inclusion of high energy particles, related to the remnants, in the jets, an effect that is enhanced by hadronisation, and that is not present in the 2-gluon exchange case. The *Inclusive* $k_\perp$ and the *CDF-CONE* algorithms perform well in the reconstruction of both direction and energy also for lower cut-offs, with little dependence on the cut-off. The *DURHAM-*k_T has often got a worse, but reasonable resolution. Nor are there any large differences between different samples for these algorithms.

5.4.3 Sensitivity of the Cut-off

If a the value of a jet algorithm cut-off at one level does not correspond to the same value at another level, it is evident that jets will be defined according to different requirements on the different levels. An error is not only introduced if the systematic shift of the cut-off variable is large, as studied in previous sections, but also if this shift changes with a changing cut-off. Considering the effects of the detector, a deviation in this respect will be increased due to smearing. This phenomena should hence be taken into account when evaluating the reconstruction abilities of jet algorithms, as stated in criterion 5 in section 5.3. The dependence of the systematic shift on the cut-off has therefore been studied. The change in the systematic shift will have noticeable

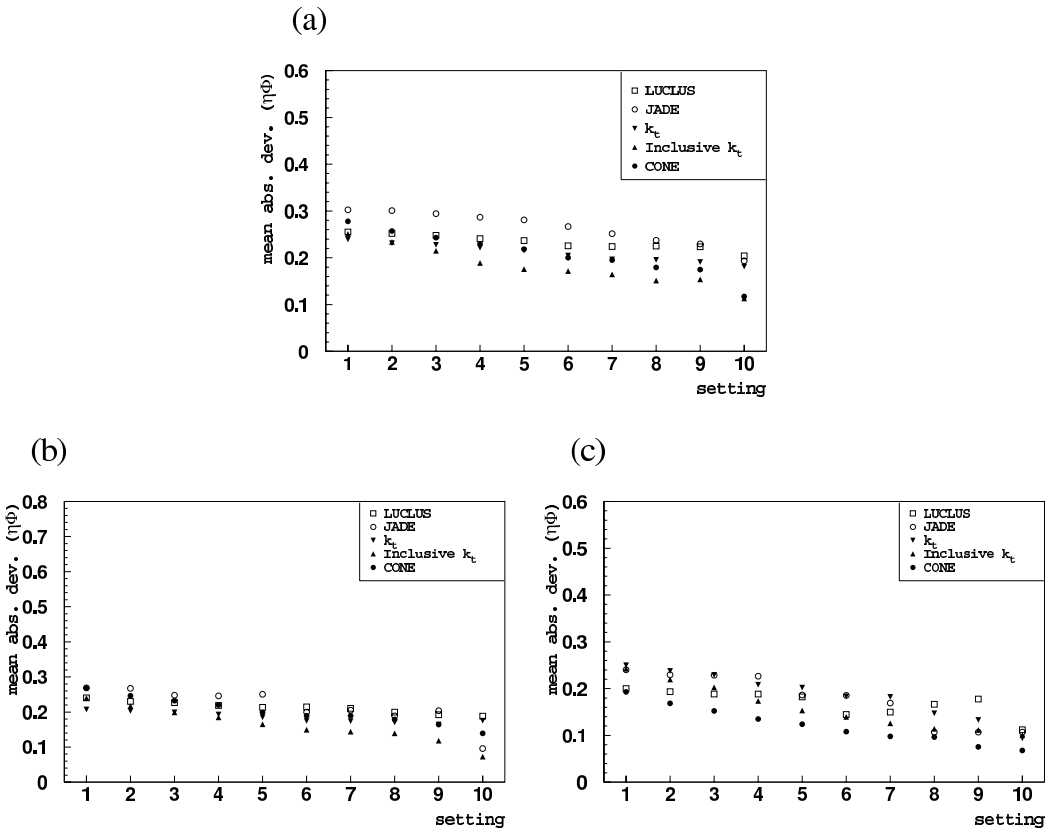

Figure 5.11: *The mean absolute deviation between between the matrix element partons and the corresponding jets at the hadron level in* (η, ϕ) *space for* (a) *the inclusive sample* (b) *the diffractive resolved pomeron sample* (c) *the diffractive 2-gluon* $q\bar{q}$ *production sample, as a function of the setting used in the algorithm seen in table 5.1.*

effects on the reconstruction if it is in the same order of, or larger than, the resolution in energy and angle of the algorithms. If the variation of the systematic shift is small however, compared to the resolution of the jet algorithms, the effects resulting from it will be negligible. As presented in previous sections, the resolution of the reconstructed direction and energy is typically approximately 10% when going from matrix element partons to hadron level jets. It is around $20-30\%$ for the inclusive sample, and a bit lower for the resolved pomeron and the 2-gluon sample. The effects on the systematic shift due to changing the cut-off, from one setting (using the settings of table 5.1) to another is typically in the order of 1% for the inclusive and the resolved pomeron sample. For t2-gluon processes it is 2% and lower. It is hence fair to say that the effect of a non-corresponding systematic shift between the different levels will not be of great importance to the reconstruction, and this is generally true for all settings and for all models studied. This is also true considering the detector resolution, which is typically in the order of 10%.

5.4.4 Next To Leading Order Sensitivity

A Next to Leading Order process in α_s is one for which the Feynman diagram contains two gluon vertices. The calculations of such processes are complicated, and specific generators, such

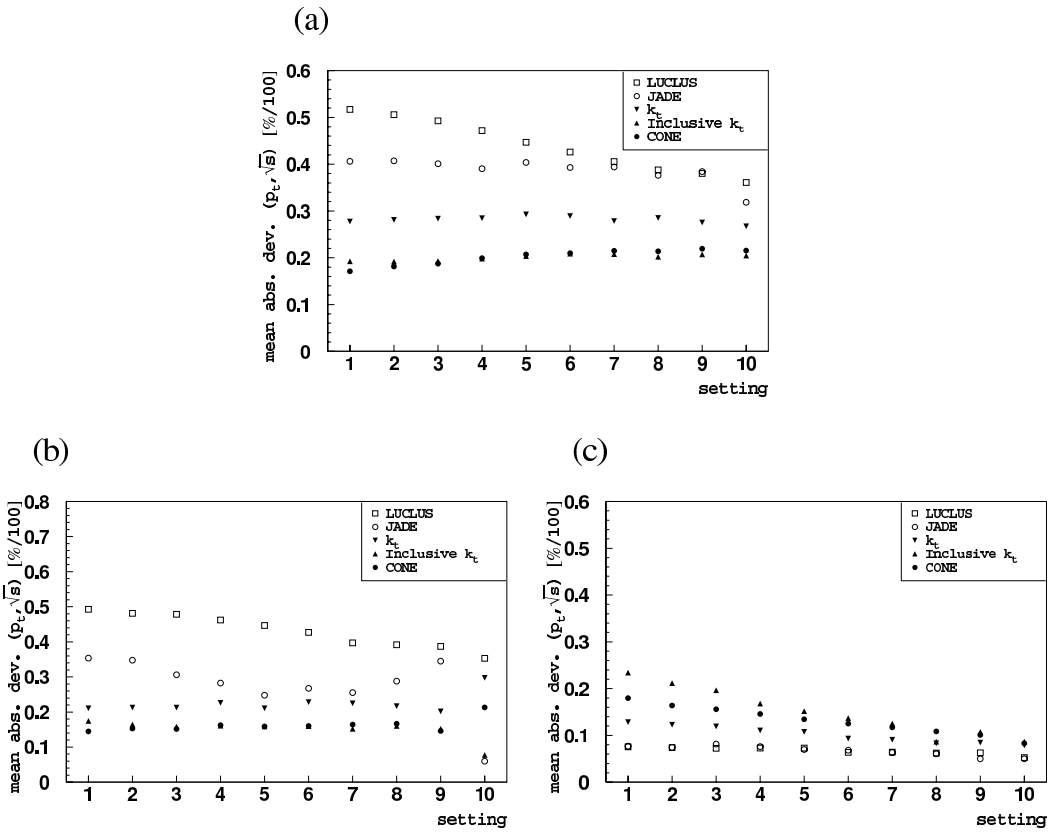

Figure 5.12: *The mean absolute deviation between the matrix element partons and the corresponding jets at the hadron level in* $(p_T, \sqrt{\hat{s}})$ *space for* (a) *the inclusive sample* (b) *the diffractive resolved pomeron sample* (c) *the diffractive 2-gluon* $q\bar{q}$ *production sample, as a function of the setting used in the algorithm seen in table 5.1.*

as DISENT [56] and JETVIP [57], have been developed for this task. These generators include the possibility for NLO calculations in standard DIS, whereas diffraction is not included. Possibilities exist for doing NLO calculations for diffraction based on the resolved pomeron model [3] For 2-gluon exchange the calculations would become very complex. We have used the generator DISENT for a study of the sensitivity to NLO corrections which has been performed on the *CDF-CONE*, *JADE* and *Inclusive* $k_\perp$ algorithms. The effects of changing the value of the renormalisation and factorisation scale in NLO should be included in the estimation of jet algorithm performance, since these scales are not known from first principles. We calculate the change in the di-jet rate for a scale $Q^2 + p_T^2$, with $p_T^2 = 50GeV^2$ and plot it as a function of Q^2. The scale is then changed by a factor of 4 or $1/4$. Along with the cut-offs applied in the jet algorithm reconstruction, a minimum p_T cut has been made on the sum of the jet p_T. The two algorithm settings used are divided into a lower and a medium cut-off scenario. The lower setting means a $p_T = 3\ GeV$ cut-off in the *CDF-CONE* and *Inclusive* $k_\perp$ reconstruction and $y_c = 0.02$ for the *JADE* algorithm. The sum of the jet p_T is required to be $8GeV$. The medium setting means a $p_T = 5\ GeV$ cut-off for the *CDF-CONE* and *Inclusive* $k_\perp$, and a $y_c = 0.04$ cut-off for *JADE*. The

[3]For diffraction according to the resolved pomeron model, NLO programs can be directly used by replacing the proton parton density function with that of the pomeron.

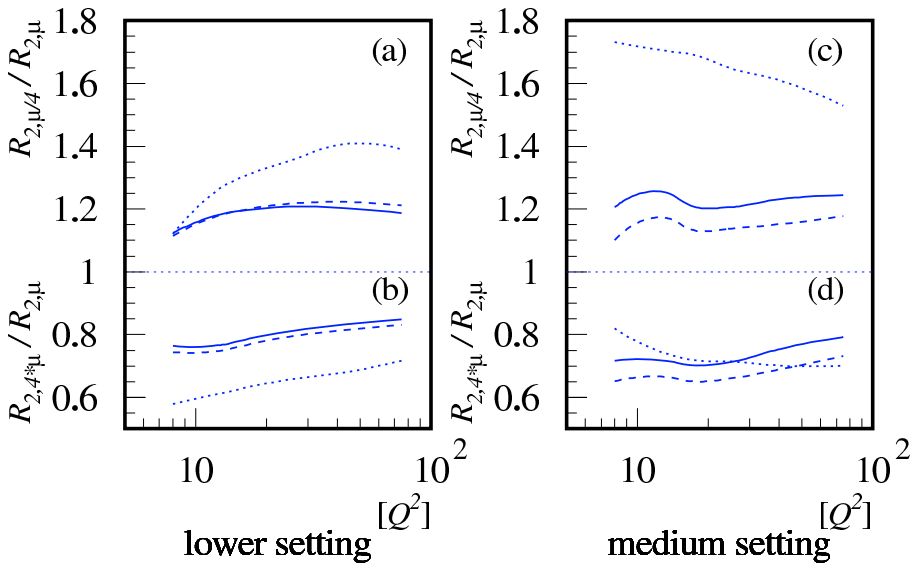

Figure 5.13: *The relative change in the 2-jet rate, when changing the renormalisation and factorisation scales in NLO calculations. The nominal scale, μ, is $Q^2 + p_t^2$. The algorithms investigated are the CDF-CONE (full line), Inclusive $k_\perp$ (dashed line) and JADE (dotted line).* (a) *The scales are changed by a factor 1/4 for the lower settings scenario.* (b) *The scales are changed by a factor 4 for the lower settings scenario.* (c) *The scales are changed by a factor 1/4 for the medium settings scenario.* (d) *The scales are changed by a factor 4 for the medium settings scenario.*

sum of the jet p_T is required to be $13\ GeV$. The two cut-off schemes were tuned as to produce *(2+1)* jet rates of similar size for the different algorithms. The requirement on the sum of the jet p_T is included as to achieve asymmetric transverse momentum, which we need in order to ensure valid NLO calculations [58].

The results are presented in fig. 5.13. The *CDF-CONE* and *Inclusive* $k_\perp$ algorithms show similar dependences on the NLO scaling, with deviations of up to around 20%, investigating the lower setting. The *JADE* algorithm reconstruction of the jet rate has a large dependence on the scale, changing with up to 40%. In the medium cut-off scenario, the *CDF-CONE* and *Inclusive* $k_\perp$ are around $20\% - 30\%$ dependent on the scale. The dependence of *JADE* is similar when changing the scale by a factor 4, but it has an even larger scale dependence than before, the jet rate changing with around 80%, for certain values of Q^2 when the scale is changed with $1/4$.

5.5 Conclusions

We have investigated the reconstruction performance of five different jet algorithms with regard to matrix element partons, parton shower and hadron level jets, using the Monte Carlo generator

RAPGAP. This was done for an ep-scattering inclusive sample, a diffractive sample based on the resolved pomeron model and one based on 2-gluon exchange $q\bar{q}$ processes. The performance of the *JADE* and *LUCLUS* algorithms is fairly poor, already when comparing matrix element partons to jets reconstructed after parton showering has been applied. A difference in the resolution obtained when investigating different models can also be noted for these two algorithms. The discrepancies are enlarged by hadronisation, and the *JADE* and *LUCLUS* algorithms show large deviations in the reconstruction of energy and momentum, when comparing hadron level jets to matrix element partons. The *DURHAM*-k_T algorithm provides a reasonable resolution in all jet quality variables and there are rarely any shifts in the reconstructed properties between different levels. The *CDF-CONE* and the *Inclusive* $k_\perp$ algorithms generally perform best. They reconstruct the properties of the hard partons well, also for lower cut-offs, and with little dependence on the type of process investigated.

Studying the systematic variation of the cut-off gave us an idea of how non-corresponding cut-offs on hadron and matrix element level affect the jet reconstruction. These effects were found to be small compared to the size of the jet algorithm resolution and to detector effects. This was true for all three event samples used.

The sensitivity of the di-jet rate to changes in the renormalisation and factorisation scales was calculated for three of the algorithms and for inclusive scattering using the NLO generator DISENT. The *JADE* algorithm here shows changes in the hadron level jet rate that is up to four times those for the reconstruction provided by the *CDF-CONE* and *Inclusive* $k_\perp$ algorithms.

Chapter 6

Forward Jet Event Analysis

Measurements on the production of forward jets and inclusive pions in HERA ep-scattering have been made, comparing data to different QCD model predictions. The measurements show that generators using standard DGLAP evolution fail in describing the forward jet and forward pion event cross-sections. However, Monte Carlo generators like RAPGAP, including a resolved component of the virtual photon, and ARIADNE, based on the colour dipole model, provide a reasonable description of the data [8, 9, 10, 11, 12].

In this chapter we present a new forward jet measurement using data taken by the H1 collaboration, during the 1997 running period at HERA. The measurement is based on a luminosity that is approximately five times that used for the previous H1 forward jet measurement [11]. In our analysis we have, along with the forward jet event cross-section as a function of Bjoerken-x, also measured the cross-section as a function of the transverse momentum, $p_{T,FWD}$, and of the fraction of the proton energy carried by the forward jet, x_{JET}. As an extension of the standard forward jet analysis, we investigate events in which two "hard" jets are found in addition to the forward jet (see fig. 6.1). Cross-sections of the above variables, Bjoerken-x, $p_{T,FWD}$ and x_{JET}, are measured. We also study the rapidity distributions of the forward jet and the two "hard" jets for different angular configurations of the hard subsystem.

The different Monte Carlo generators used for various calculations and comparisons with data in our measurements are briefly discussed in section 6.1. In section 6.2 and 6.3 we present the selection of DIS events used in this analysis. The forward jet selection is presented in section 6.4. The selection of events, where two "hard" jets are found in addition to the forward jet is presented in section 6.5. Our measurement of the forward jet event cross-section is presented in section 6.6. The cross-section of events where a forward jet and two "hard" jets are found will be presented in section 6.7. A study of the rapidity of the forward jet and the "hard" jets in such events, is presented in section 6.8. Conclusions and suggestions on how one might continue the investigation of ep DIS parton dynamics in the forward jet final state, are presented in section 6.9.

(a) (b)

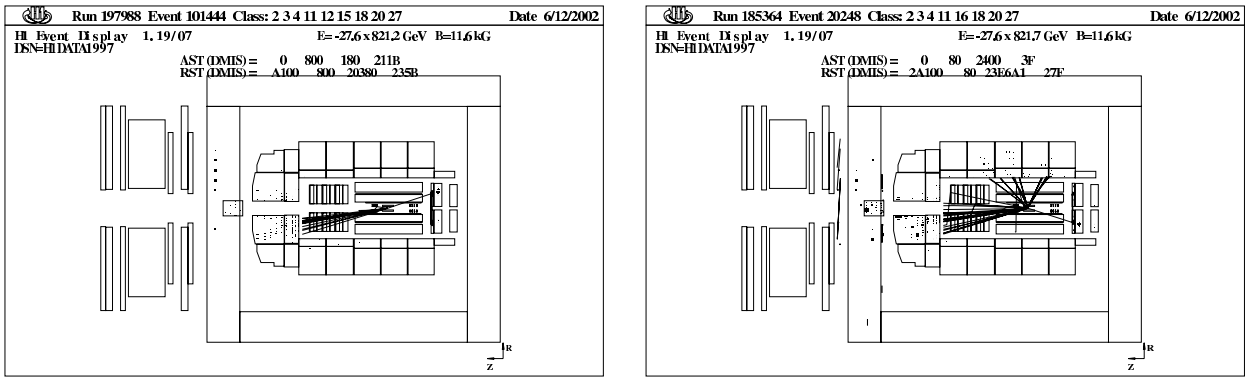

Figure 6.1: *H1 event display view of* (a) *a forward jet event,* (b) *a 2+forward jet event.*

6.1 Monte Carlo Generators

In this analysis we used the RAPGAP [20] Monte Carlo generator, which accounts for QCD radiation by means of parton showers based on the DGLAP (see section 2.3.2) evolution formalism, using a backward evolution scheme. The evolution starts on the photon side, at the scale of the hard scattering, and continues towards the proton side, to a cut-off value, Q_0^2. This is done under the requirement of strong ordering in parton propagator virtuality, k^2, which generally means ordering also in the transverse momentum squared, ${k_T}^2$, of the propagators in the parton ladder. RAPGAP, using a standard DGLAP evolution, based on the higher order DIS scheme parton density function [59], with a $\mu^2 = p_T + Q^2$ for the factorisation and renormalisation scale, will be referred to as *RG(DIR)* in this analysis.

The RAPGAP generator contains the possibility of treating the photon as a resolved object, according to the *resolved photon model* [21] (discussed in section 2.4.1). The expansion of the photon is in RAPGAP added by applying a backward DGLAP evolution, that starts at the hard scattering, and is limited by the virtuality of the photon. We will refer to RAPGAP, including the contribution from a resolved component of the virtual photon, based on the SaS [60] photon structure function as *RG(DIR+RES)*.

The Monte Carlo generator ARIADNE [27] adds QCD radiation according to the Colour Dipole Model, *CDM* (see section 2.4.2), where the emitted partons form a chain of radiating dipoles. In ep-scattering, the evolution starts from a dipole formed by the proton remnant and the scattered parton. This scheme takes QCD-Compton processes into account, whereas BGF processes have to be added from matrix element calculations. In the ARIADNE CDM evolution, no requirements on strong ordering in virtuality are made.

In addition to the well established Monte Carlo generators RAPGAP and ARIADNE, we have also used the recently developed generator CASCADE [24], which is based on the CCFM formalism, discussed in section 2.3.4. CASCADE, calculates first order processes from matrix

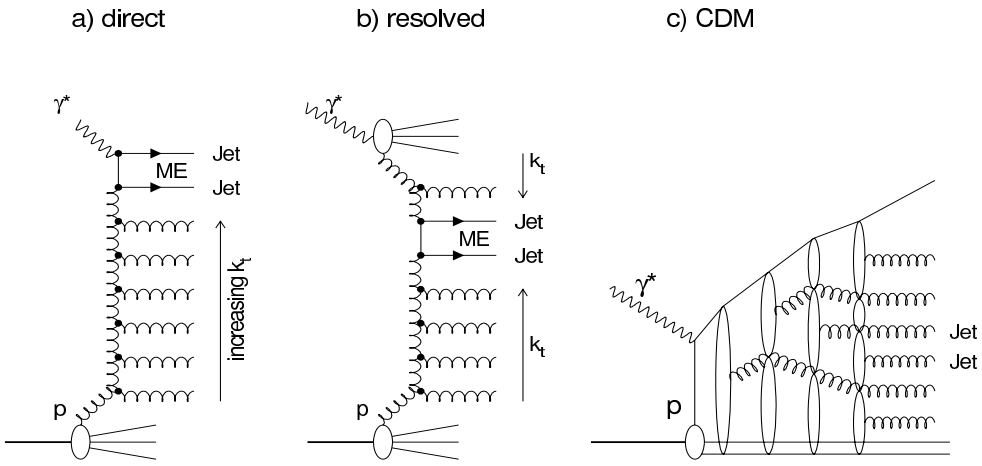

Figure 6.2: *Generic diagrams of parton emissions, according to different models.* (a) *In a direct process where the emissions are made according to the DGLAP evolution formalism, the propagator partons are strongly ordered in transverse momentum* k_T. (b) *Adding the resolved photon to the DGLAP picture, evolution is made from both sides of the ladder, with increasing* k_T*, the closer to the matrix element hard partons the propagators on the different sides are.* (c) *According to the colour dipole model, where emissions pairs are treated as dipoles and no requirements are made on strong ordering in transverse momentum.*

elements and adds initial state parton showering, using a backward evolution scheme. The evolution is carried out under the requirement of angular ordering between the ladder emissions. For normalisation, the results of the CASCADE generator have for this analysis been reweighted by a factor 0.6, and will be referred to as *CASCADE(RW)*.

In the discussion on the event reconstruction, the errors calculated and the correction carried out in this analysis, we have used the predictions of RAPGAP and ARIADNE, that have undergone a detector simulation, whereas differential cross-sections will be compared to the predictions of all four models.

In the detector simulation of generated events, the effects of the detector, including limitations in resolution and acceptance are taken into account, and a detector reconstruction is applied to the events. This is done using the standard H1 program H1SIM. After detector simulation, the generated final state is specified through different detector objects: clusters, tracks and hits, corresponding to those of the experimental data.

6.2 Run and Trigger Selection

The data analysed are from the 1997 data taking period at H1, where runs with a total luminosity of 21.57 pb^{-1} were collected. A run selection has been made requiring that the high voltage

system is operational for the subdetectors used in the measurement: the LAr calorimeter, the SpaCal, the BDC, the central jet chambers CJC1 and CJC2, the CIZ, the time-of-flight scintillators and the luminosity system[1].

A trigger selection is made for events to be in the *'DIS'* and *'jet'* physics classes, making requirements on the event kinematics in accordance with what is expected from a deep inelastic scattering jet event. Backgrounds and photoproduction events are suppressed by requiring the positron to be detected in the SpaCal. Low Q^2 events are cut away and scaled, and events with specific physics signatures, such as a high p_T jet are selected.

The basic L1 requirement on the S_0 trigger, used in this analysis, is:

$$S_0 = (IET > 2) \wedge (TOF) \quad , \tag{6.1}$$

where IET is the *Inclusive Electron Trigger*, of the SpaCal and the requirement $IET > 2$ corresponds to an energy threshold of $5.7\ GeV$. The TOF requirement guarantees a time window that is characteristic for DIS events.

The down-scaling made on the different trigger levels is accounted for by applying the corresponding weights to the events kept. The total luminosity of the runs satisfying the trigger requirements was found to be 13.72 pb^{-1}.

6.3 DIS Selection

To accurately measure ep DIS events, we want to ensure that the scattered lepton is properly detected, and not misidentified with the hadronic or photoproduction background. Furthermore we want to reduce the influence of bremsstrahlung, and make sure that the event vertex is well defined. The DIS selection cuts are designed to ensure event reconstruction within the acceptance of the different detectors, to suppress backgrounds and to minimise corrections. In section 6.3.1 the different cuts made on the positron candidate are presented. The selection with respect to $\sum_i (E_i - p_{z,i})$, summing over all final state objects, is described in 6.3.2. Section 6.3.3 describes the treatment of the event vertex. The DIS kinematic range of this analysis is discussed in section 6.3.4 and the detector reconstruction of DIS events, in section 6.3.5.

6.3.1 Positron Selection

The SpaCal consists of a number of cells, and a SpaCal cluster is defined by summing up the energy, E_i, of the cells in an event. The largest background contributions when identifying the positron comes from photoproduction events, where the interaction energy is low and the scattered lepton travels down the beam pipe. A "fake" positron candidate, stemming from showering in the dead material in front of the SpaCal, or in the form of a hadron, may be misidentified

[1]The H1 experiment uses the elastic bremsstrahlung process $e + p \rightarrow e + \gamma + p$, as detected by the *electron tagger* ($z = -33.4m$) and *photon detector* ($z = -102.9m$) to measure the luminosity of the scattering.

as the scattered lepton. Therefore, a cut on the reconstructed energy of the positron, E_e, is applied, $E_e > 11\ GeV$. We also demand the scattered positron polar angle, to be within the range $160° < \theta_e^{'} < 172.5°$, as to ensure that the positron is well contained within the SpaCal.

The centre-of-gravity of the SpaCal cluster, r_{CLUS}, can be defined:

$$r_{CLUS} = \frac{\sum_{i=1}^{n} \sqrt{E_i} r_i}{\sum_{i=1}^{n} \sqrt{E_i}} \quad , \tag{6.2}$$

where r_i is the centre of the i:th SpaCal cell. An energy-weighted cluster radius is given by:

$$R_{CLUS} = \frac{1}{E_{CLUS}} \sum_{i=1}^{n} E_i \times |r_i - r_{clus}| \quad , \tag{6.3}$$

where E_{CLUS} is the cluster energy. We cut on this variable $R_{CLUS} < 3.5\ cm$, to further reduce backgrounds, since hadronic showers generally are broader than what is expected from the positrons.

The hadronic backgrounds can also be reduced through measuring the energy in the hadronic part of the SpaCal. The electromagnetic calorimeter is able to contain energies of up to 30 GeV and if the energy deposit in the hadronic calorimeter, E_{HAD}, is large, this is a sign of hadronic interactions. A cut is therefore imposed on the energy in a circle of radius $15\ cm$, with respect to the impact position of the positron candidate, demanding $E_{HAD} < 0.5\ GeV$.

The SpaCal comprises a layer of four *veto* cells adjacent to the beam pipe. The veto layer can be used to reject events for which the transverse energy leakage out of the detector is large. The occurrence of energy leakage means that the full lepton energy is not detected within the SpaCal, and that the measurement of the lepton is distorted. Therefore, we require the energy deposited in the veto layer, E_{VETO}, not to exceed a limit of 1 GeV, $E_{VETO} < 1\ GeV$.

A cut on the radial distance between the SpaCal cluster and the track reconstructed in the BDC, $\Delta R_{BDC} < 3cm$, is made to reduce the background of photons that are detected in the SpaCal, in combination with a hadronic track in the BDC, which could otherwise fake a lepton signal.

6.3.2 Final State Object $\sum_i (E_i - p_{z,i})$

In the case of a perfect measurement, the sum of all final state objects $E - p_z$ should, due to energy conservation, equal twice the lepton beam energy: $\sum_i (E_i - p_{z,i}) = 2E_e = 55\ GeV$, where the variable E_i denotes the energy of particle i, $p_{i,z}$ denotes the z component of its momentum, and the summation is made over all detected particles, including the scattered positron. The sum of the difference between the final state object energy and its momentum in the z direction, is in this analysis calculated from both calorimeter and track information. If a hadron is misidentified as the scattered lepton in a photoproduction event, the sum is expected to be smaller than the above value. Photons radiated off the incoming positron can also contribute to distorting this quantity.

We demand the sum to be within the range $35 < \sum_i (E_i - p_{z,i}) < 75\ GeV$, to suppress such backgrounds.

6.3.3 Requirements on the Vertex

Interactions of the beam with the beam-pipe and the rest gas in the vacuum system occurs throughout the full length of the HERA ring. The total interaction length of the bunch crossings is within limits of the nominal interaction point. In order to reject the beam interaction background we make a requirement on the distance of the vertex to the nominal interaction point along the z axis, $|z_{vtx}| < 30\ cm$. In this region, the contribution from ep interactions are much larger than that from background contributions.

6.3.4 Kinematic Reconstruction and the DIS Kinematic Range

In the so-called *electron method*, the scattered positron energy, $E_e^{'}$, and angle, $\theta_e^{'}$, are used to calculate the inclusive quantities, x, y and Q^2. The measurement of these quantities rely on the SpaCal, BDC and the LAr calorimeter. The different variables are calculated as:

$$Q^2 \approx 4E_e E_e^{'} \cos^2(\theta_e^{'}/2) \tag{6.4}$$

$$x_{Bj} \approx 4E_e E_e^{'} \cos^2(\theta_e^{'}/2) E_p (E_e - E_e^{'} \sin^2(\theta_e^{'}/2)) \tag{6.5}$$

$$y \approx \frac{E_e - E_e^{'} \sin^2(\theta_e^{'}/2)}{E_e} \tag{6.6}$$

The DIS kinematic range is defined in y and Q^2, and we demand the events to satisfy:

$$5\ GeV^2 < Q^2 < 75\ GeV^2$$

$$0.1 < y < 0.7$$

This sets the limits for the acceptance of the scattered positron in the SpaCal and cuts away kinematic regions where the backgrounds are large.

In addition, throughout this analysis, a cut in Bjoerken-x will be applied, as to create a clearly defined region in this variable:

$$0.0001 < x < 0.004$$

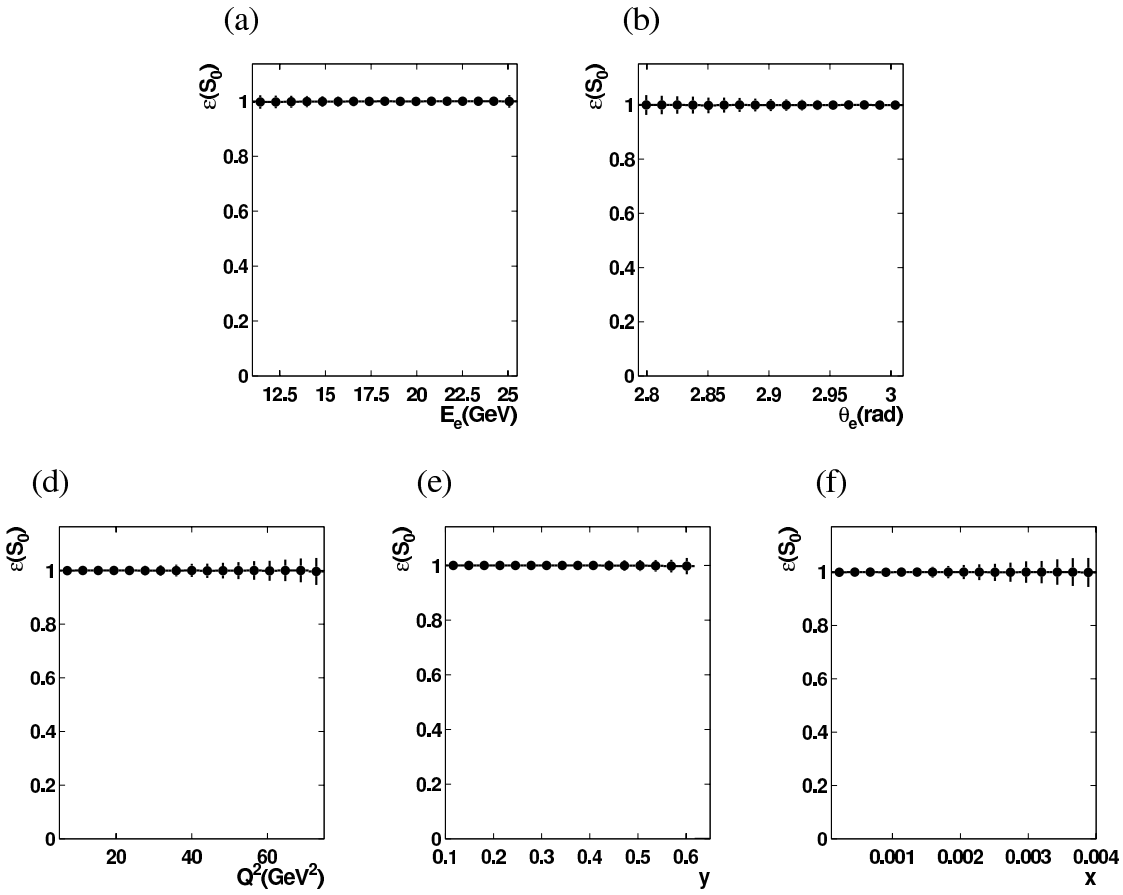

Figure 6.3: *Trigger efficiency, ϵ, for DIS events, of the S_0 trigger, shown as a function of (a) $E_e^{'}$, (b) $\theta_e^{'}$, (c) Q^2 calculated from the electron method, (d) Bjoerken-y calculated from the electron method and (e) Bjoerken-x calculated from the electron method. The results from experimental data (dots) are shown.*

6.3.5 DIS Event Reconstruction

During 1997, the S_0 trigger showed insensitivities for certain fiducial regions of the SpaCal, and we are forced to exclude these regions from our analysis. In the spatial coordinates of the SpaCal, (x_S, y_S), the following regions are removed:

$$
\begin{gathered}
-16.2 < x_S < 8.1 \wedge -8.1 < y_S < 16.2 \\
-25.0 < x_S < -20.5 \wedge -37.5 < y_S < -33.0 \\
-16.25 < x_S < 12.5 \wedge -21.0 < y_S < -16.0 \\
-31.5 < x_S < -25.5 \wedge 33.1 < y_S < 39.1 \\
-48.0 < x_S < -46.1 \wedge -28.0 < y_S < -25.0
\end{gathered}
$$

We study the *trigger efficiency*, ϵ, of S_0, by selecting events using a *monitor trigger*, independent of S_0, and calculating the fraction of these events passing the event selection $N_{SEL,MON}$, that

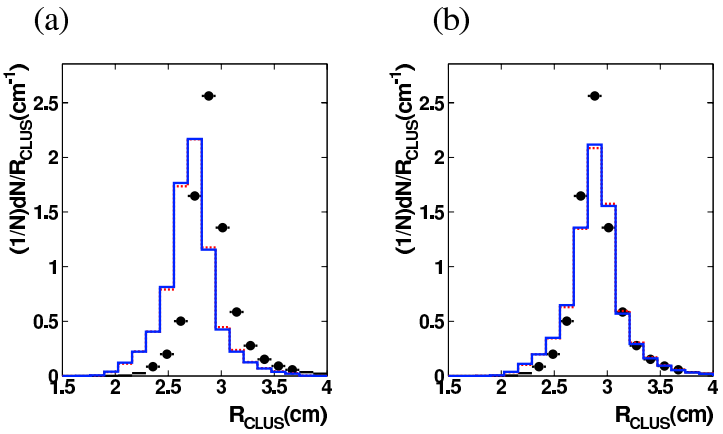

Figure 6.4: *The electron cluster radius, R_{CLUS}, (a) before, and, (b) after a correction factor* 1.065 *has been applied to the Monte Carlo distributions. Experimental data (dots) are compared to detector simulated Monte Carlo data from ARIADNE (full line) and RAPGAP (dashed line).*

also pass the trigger requirements, $N_{SEL,MON,SUB}$:

$$\epsilon = \frac{N_{SEL,MON,SUB}}{N_{SEL,MON}} \tag{6.7}$$

In fig. 6.3, the S_0 trigger efficiency, calculated for the DIS selection described in section, and the kinematic cuts of section 6.3.4 is shown. Only negligible deviations from $\epsilon = 1$ can be seen, meaning the trigger does not select any events outside our event selection.

The detector simulation contains an error that produces a misestimate of the cluster radius compared to that obtained from data [61]. As to gain agreement between data and the detector simulated Monte Carlo events in the region where the cut is applied, a correction factor of 1.065 is applied to the simulated cluster radius distribution, see fig. 6.4.

The HERA beam position and H1 experimental interaction point changes during data taking, while it was fixed at $z = 0$ in the detector simulation. This causes the average value and the spread of the Monte Carlo z_{vtx} to differ from that of data. We have therefore reweighted the simulated z_{vtx} position to fit that of data. The z_{vtx} distributions before and after reweighting has been applied are shown in fig. 6.5.a and 6.5.b.

The DIS selection presented in section 6.3, and the kinematic cuts of section 6.3.4 have been applied to uncorrected data and detector level simulated samples of RAPGAP and ARIADNE events. The scattered positron energy, $E_e{}'$ and angle $\theta_e{}'$, Q^2, Bjoerken-y and Bjoerken-x calculated according to the electron method, are shown in fig. 6.6. The distributions are normalised to the number of events selected.

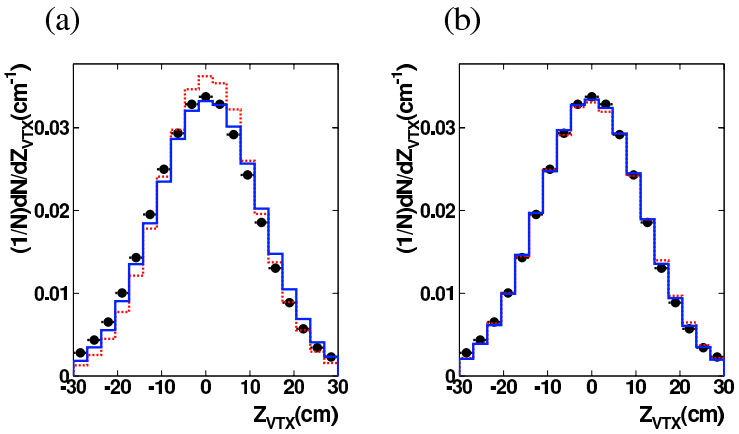

Figure 6.5: *The z_{vtx} position, (a) before, and, (b) after a z_{vtx} reweighting has been applied to the Monte Carlo distributions. Experimental data (dots) are compared to detector simulated Monte Carlo data from ARIADNE (full line) and RAPGAP (dashed line).*

6.4 Forward Jet Event Selection

DIS events in which an energetic jet is emitted close to the direction of motion of the proton remnant are called *forward jet events*. A number of requirements have been applied to the forward jet, as to enhance the BFKL-like parton dynamics of these events.

The jet selection of this analysis is carried out using the *Inclusive* $k_\perp$ jet algorithm[2] (see section 5.1.5). The algorithm is applied on objects that are a combination of clusters and tracks, according to the FSCOMB method [62].

In the event selection, a forward jet must be found in a rapidity region of $1.735 < \eta_{JET} < 2.79$, which corresponds to an angular region in which the spatial resolution is reasonable. We thereby avoid selecting the proton remnant as a forward jet, or including parts of the remnant in the jet [63].

In order to enhance the sensitivity to BFKL-like dynamics, the phase-space for DGLAP evolution is suppressed by requiring that the forward jet transverse momentum, $p_{T,FWD}$, squared is close to the Q^2 value. The cut applied is: $0.5 < \frac{p^2_{T,FWD}}{Q^2} < 2$.

The relative energy of the forward jet is given by the variable $x_{JET} = E_{FWD}/E_p$, where E_{FWD} is the energy of the forward jet, and E_p is the energy of the proton, and it is required that $x_{JET} > 0.035$. Events in which the difference between Bjoerken-x and x_{JET} is large are thereby selected, leaving room for a sufficiently large parton ladder and evolution in x.

A cut on the transverse momentum of the forward jet is also made, as to ensure a good jet reconstruction and exclude jets created from noise or proton dissociation. In this analysis, we

[2]The jet selection of the previous H1 forward jet analysis [11] was carried out using the *CDF-CONE* algorithm.

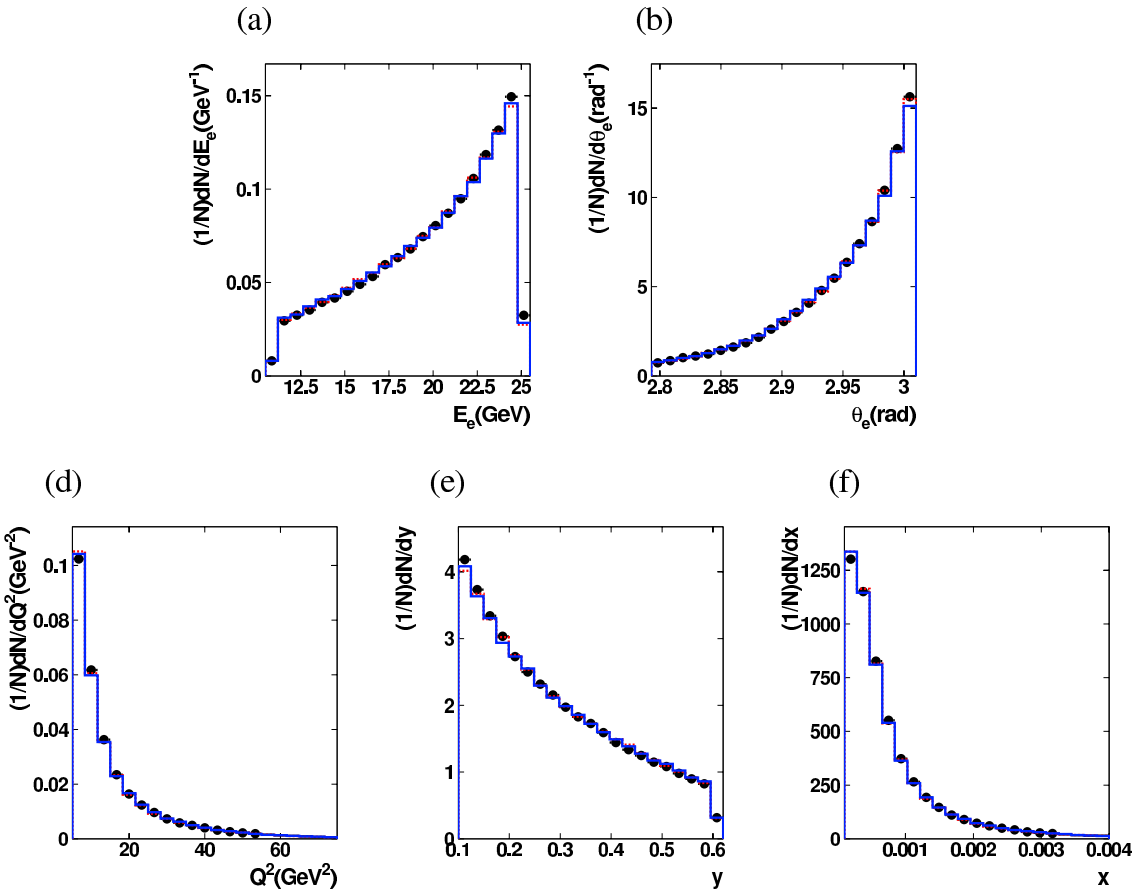

Figure 6.6: *Detector level distributions for DIS events, showing* (a) E_e', (b) $\theta_e{}'$, (c) Q^2 *calculated from the electron method,* (d) *Bjoerken-*y *calculated from the electron method and* (e) *Bjoerken-*x *calculated from the electron method. Experimental data (dots) are compared to detector simulated Monte Carlo data from ARIADNE (full line) and RAPGAP (dashed line). The distributions are normalised to the number of events selected,* N.

study two transverse momentum cutoff scenarios: $p_{T,FWD} > 3.5GeV$ or $p_{T,FWD} > 5GeV$.

Selecting forward jet events in this way, we expect to be dealing with less DGLAP-like parton dynamics as compared to standard DIS processes, and allow for BFKL-like dynamics to be more visible. Around 1% of the DIS events selected are also selected as forward jet events. In $\approx 1\%$ of these events, more than one jet passes the forward jet cuts, and in such an event, the most forward of these jets are defined as the forward jet.

In fig. 6.7 and 6.8, various kinematic quantities are plotted after the DIS and forward jet cuts have been applied. The distributions are normalised to the number of events passing the forward jet cuts. Detector simulated Monte Carlo events, from the DGLAP based generator RAPGAP show disagreements with data while the ARIADNE program manages to provide a reasonable description of both the basic kinematic variables and the variables reconstructed from the for-

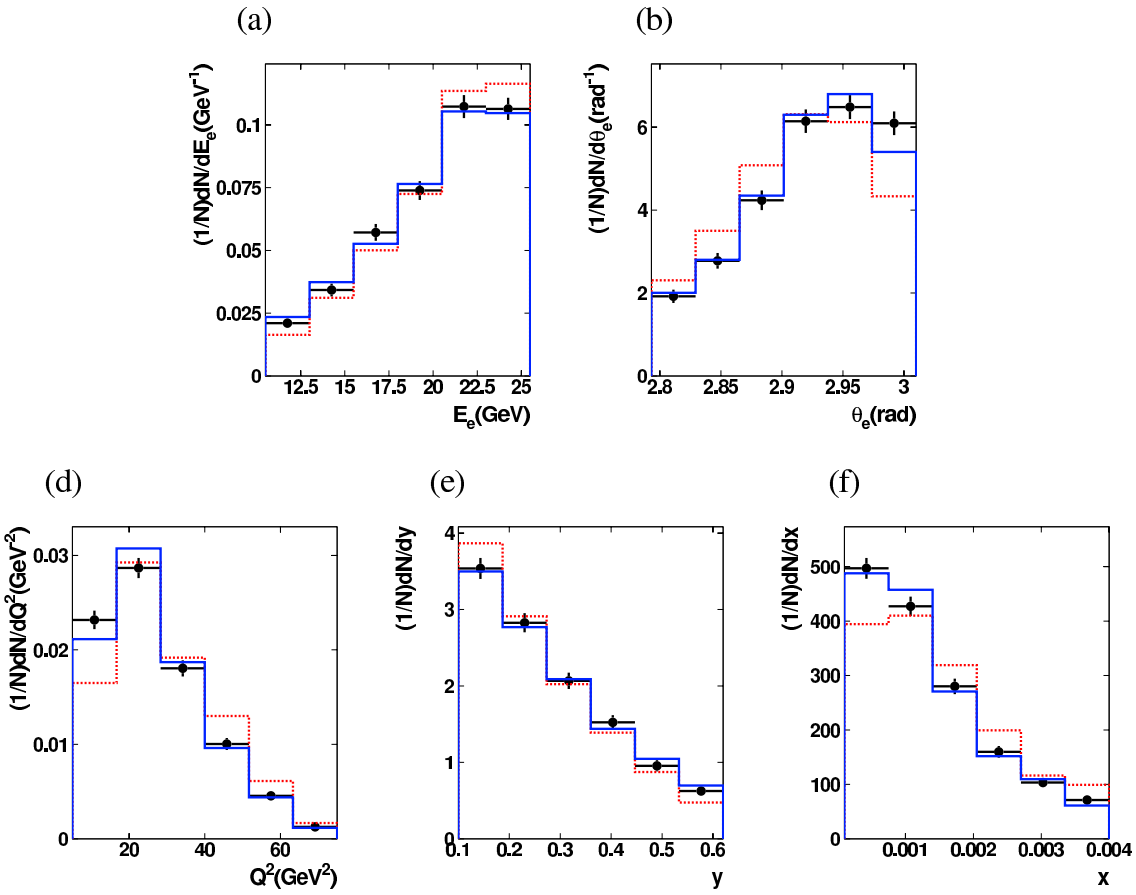

Figure 6.7: *Detector level distributions for forward jet DIS events, demanding a forward jet* $p_{T,FWD} > 3.5$ *GeV, showing* (a) E_e', (b) θ_e', (c) Q^2, (d) *Bjoerken-*y *and* (e) *Bjoerken-*x*. Experimental data (dots) are compared to detector simulated Monte Carlo data from ARIADNE (full line) and RAPGAP (dashed line). The distributions are normalised to the number of events selected,* N*.*

ward jet properties.

In Fig. 6.9, the transverse energy flow, around the axis of the selected forward jet has been plotted as a function of $\Delta\eta = \eta_i - \eta_{FWD}$ and $\Delta\phi = \phi_i - \phi_{FWD}$, for the clusters found in a slice of $\Delta\phi = 1$ and $\Delta\eta = 1$, respectively. η_i and ϕ_i are here the rapidity and azimuthal angle of the clusters and η_{FWD} and ϕ_{FWD} are the forward jet rapidity and azimuthal angle. Experimental data and detector simulated RAPGAP and ARIADNE Monte Carlo data are compared. We note that neither the predictions of RAPGAP, nor of the ARIADNE generator, give a completely satisfactory description of the full forward jet profile in η and ϕ.

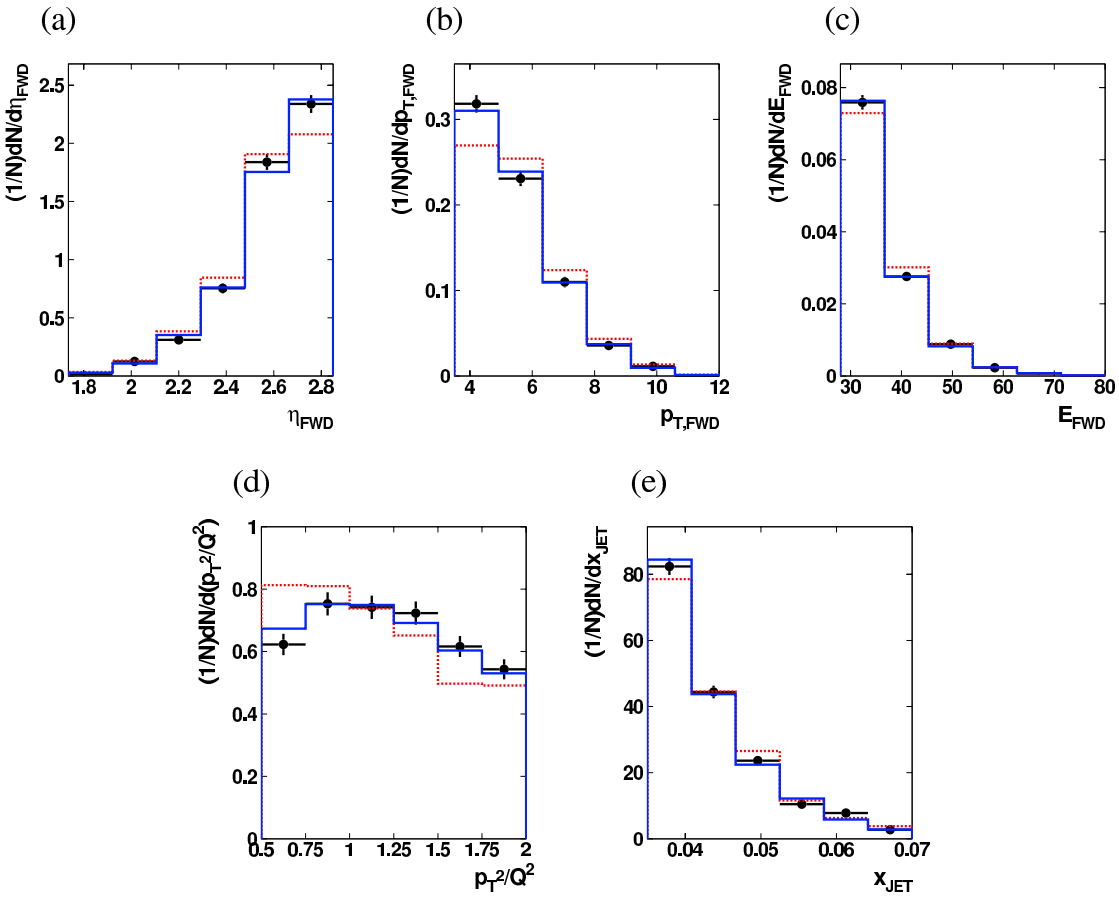

Figure 6.8: *Detector level distributions for forward jet DIS events, demanding a forward jet* $p_{T,FWD} > 3.5\ GeV$*, showing* (a) *the forward jet rapidity,* η_{JET}*,* (b) *the forward jet transverse momentum,* $p_{T,FWD}$*,* (c) *the forward jet energy,* E_{FWD}*,* (d) $\frac{p^2_{T,FWD}}{Q^2}$ *and* (e) $x_{JET} = \frac{E_{FWD}}{E_P}$*. Experimental data (dots) are compared to detector simulated Monte Carlo data from ARIADNE (full line) and RAPGAP (dashed line). The distributions are normalised to the number of events selected,* N*.*

6.5 2+Forward Jet Event Selection

We define the particular class of forward jet events, in which two "hard" jets are found in addition to the forward jet, as *2+forward jet* events. Selecting such events, allows us to target a more specific parton ladder configuration than when requiring only a forward jet to be found. By including the hard subsystem in the measurement we gain further information on the structure of the QCD cascade and the parton dynamics of forward jet events.

The "hard" jets are required to have a transverse momentum, $p_T > 3.5\ GeV$ and a rapidity smaller than that of the forward jet found, and larger than that of the scattered lepton in the event, $\eta_e < \eta_{HARD} < \eta_{FWD}$. This is to create a well defined parton ladder, for each event, where the start and end points of the ladder in angular space are given by the scattered lepton and the

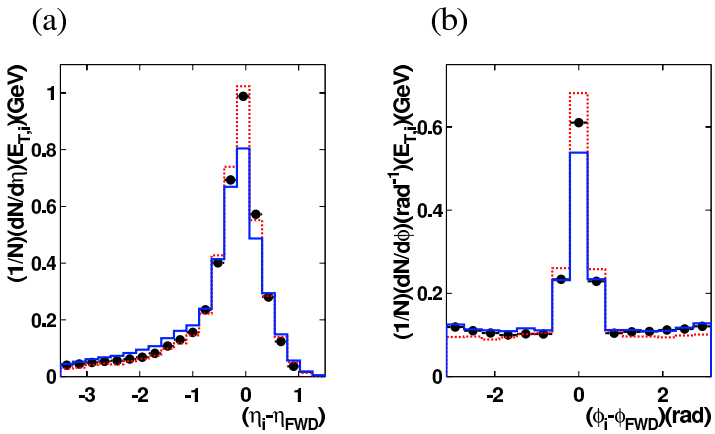

Figure 6.9: *Detector level distributions of the transverse energy flow around the axis of the forward jet, as a function of* (a) $\Delta\eta = \eta_i - \eta_{FWD}$ *in a slice of* $\Delta\phi = \phi_i - \phi_{FWD} = 1$ *and* (b) $\Delta\phi = \phi_i - \phi_{FWD}$ *in a slice of* $\Delta\eta = \eta_i - \eta_{FWD} = 1$. *Experimental data (dots) are compared to detector simulated Monte Carlo from ARIADNE (full line) and RAPGAP (dashed line). The distributions are normalised to the number of events selected,* N.

forward jet.

In fig. 6.10 we investigate the forward jet quantities, for the 2+forward jet event selection. We see that, as for the standard forward jet selection, the detector simulated ARIADNE Monte Carlo gives a reasonable description of the data, whilst the description provided by the RAPGAP generator often shows discrepancies from the data. Around 20% of the forward jet events are identified as 2+forward jet events.

The two hardest jets in an event, satisfying the above conditions, will be taken as the "hard" jets defining a 2+forward jet event. The individual "hard" jets may then be referred to as the jet closest to the scattered lepton, and the jet closest to the forward jet, in rapidity, respectively. Different angular configurations of these jets can then be studied. We define the distance in rapidity between the jets:

$$\Delta\eta = \eta_{HARD2} - \eta_{HARD1} \quad , \tag{6.8}$$

where η_{HARD1} is the rapidity of the "hard" jet closest in rapidity to the scattered lepton and η_{HARD2} the rapidity of the "hard" jet closest in rapidity to the forward jet. Different ranges in the $\Delta\eta$ of the hard subsystem, correspond to different QCD cascade structures (see fig. 6.11). In the case of a small $\Delta\eta$, we enhance the phase space for BFKL evolution, whereas, if we demand a large rapidity gap between the jets of the hard subsystem, we restrict the possibility of multiple parton emissions between the most forward "hard" jet and the forward jet. The latter situation would correspond to the dynamics of a process in which the photon has a resolved structure.

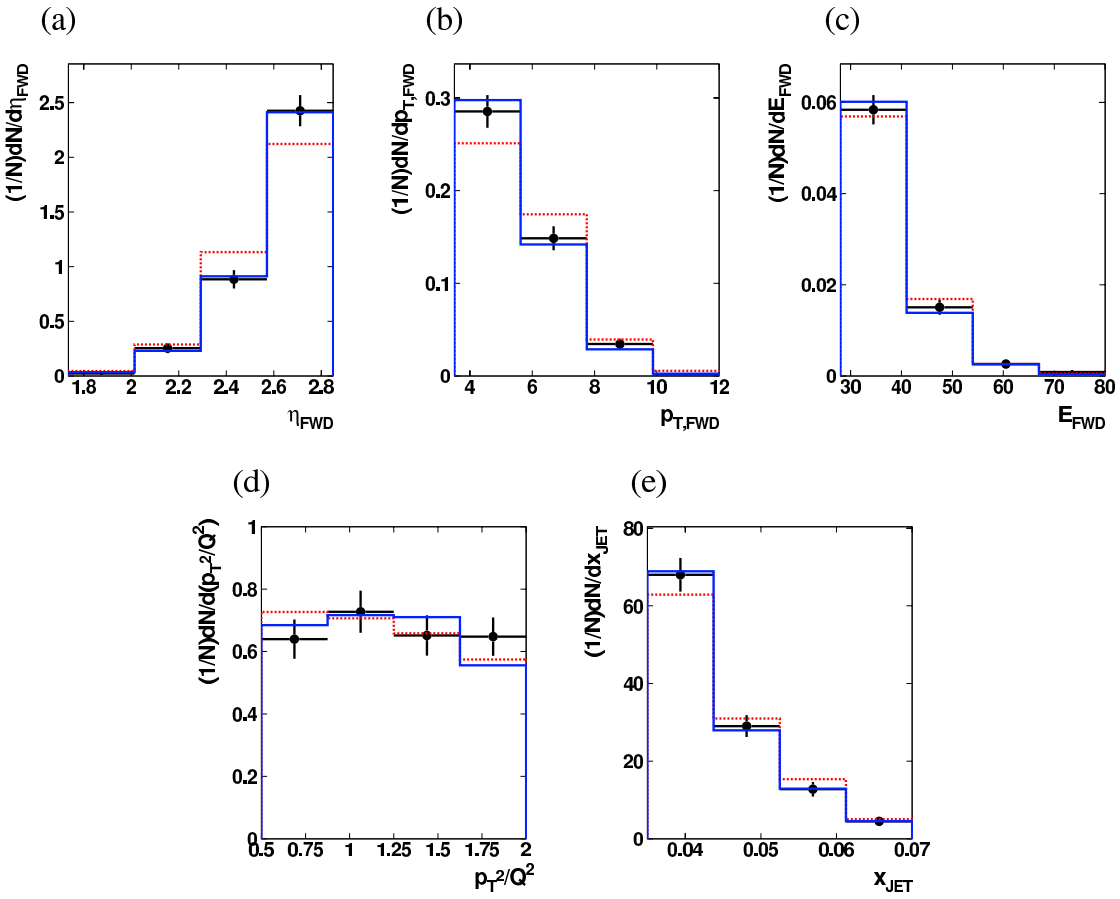

Figure 6.10: *Detector level distributions for 2+forward jet DIS events, demanding a forward jet* $p_{T,FWD} > 3.5\ GeV$*, showing* (a) *the forward jet rapidity,* η_{FWD}*,* (b) *the forward jet transverse momentum,* $p_{T,FWD}$*,* (c) *the forward jet energy,* E_{FWD}*,* (d) $\frac{p^2_{T,FWD}}{Q^2}$ *and* (e) $x_{JET} = \frac{E_{FWD}}{E_p}$*. Experimental data (dots) are compared to detector simulated Monte Carlo data from ARIADNE (full line) and RAPGAP (dashed line). The distributions are normalised to the number of events selected,* N*.*

6.6 Forward Jet Event Cross-section Measurement

The forward jet event cross-section measurement is made using data taken by H1 in 1997, for which the runs selected have a total luminosity of 13.72 pb^{-1}. The quality of the forward jet event selection of our measurement is investigated in section 6.6.1. The detector level distributions and the correction to hadron level is presented in section 6.6.2. The calculation of systematic errors, derived from the model dependence of the correction and a number of detector uncertainties is presented in section 6.6.3. The forward jet event cross-section is presented as a function of three different quantities, x, $p_{T,FWD}$ and x_{JET}, and data are compared to generator predictions based on different evolution schemes, in section 6.6.4.

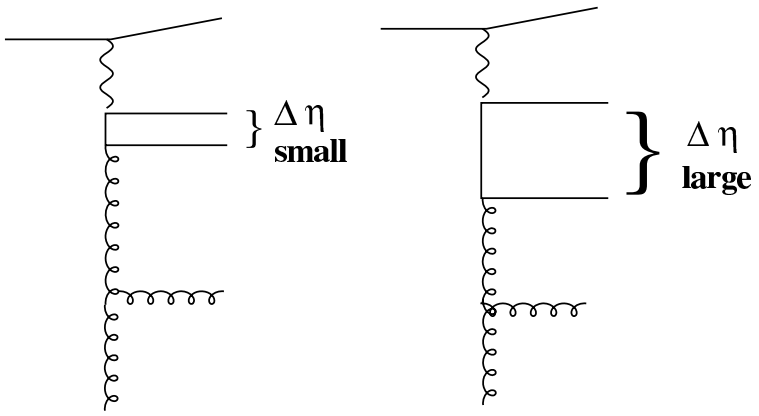

Figure 6.11: *Illustration of different 2+forward jet event $\Delta\eta$ configurations.*

6.6.1 Purity, Stability, Background and Acceptance

In order to appreciate the validity of our measurement, we need to investigate the relation between the description provided on the detector and on the hadron level, in each bin of the measurement. We define the purity, P, stability, S, background, B, and acceptance, A, in the following way:

$$P = \frac{N_{HAD\cap DET}}{N_{DET}}(HAD \cap DET) \tag{6.9}$$

$$S = \frac{N_{HAD\cap DET}}{N_{HAD}}(HAD \cap DET) \tag{6.10}$$

$$B = 1 - \frac{N_{HAD\cap DET}}{N_{DET}}(DET) \tag{6.11}$$

$$A = \frac{N_{HAD\cap DET}}{N_{HAD}}(HAD) \quad , \tag{6.12}$$

where N_{HAD} is the number of events found in a certain bin on hadron level, N_{DET} is the number of events found in a certain bin on detector level, and, $N_{HAD\cap DET}$, are the number of events that are found in the same bin both on hadron and detector level. P and S are defined on an event-by-event basis where both the hadron and detector level cuts have been passed. B is calculated from the events passing the detector level cuts and A is calculated from the events passing the hadron level cuts.

In fig. 6.12, diagrams of the purity, stability, background and acceptance, are shown for events containing a forward jet, calculated in bins of Bjoerken-x. The histograms relate the detector simulated results of the Monte Carlo generators RAPGAP and ARIADNE to their hadron level predictions. The purity and stability for Bjoerken-x are larger than 0.6 and sometimes reach

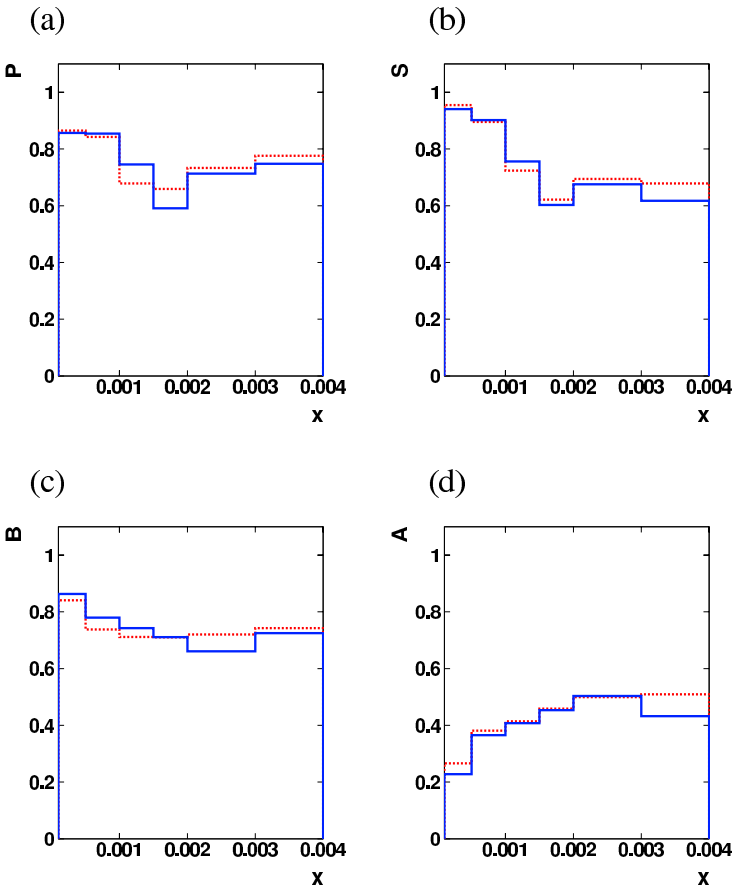

Figure 6.12: *The forward jet DIS event* (a) *purity,* P*,* (b) *stability,* S*,* (c) *background,* B*, and* (d) *acceptance,* A*, calculated in bins of Bjoerken-*x*. The predictions from Monte Carlo generators ARIADNE (full line) and RAPGAP (dashed line) are shown.*

values of 0.8-0.9. The background is however quite large in all bins, and the acceptance is particularly low in the lowest x-bin.

The purity, stability, background and acceptance, as a function of variables $p_{T,FWD}$ and x_{JET}, are plotted in figs. 6.13 and 6.14. They similarly show reasonable purities and stabilities but a sometimes large background and low acceptance.

The low acceptance for forward jet events has been observed also in previous analyses [63], [9] and may to a large extent originate from the $\frac{{p_{T,FWD}}^2}{Q^2}$ cut [64] where the smearing in p_T affects the effective cut in Q^2.

In fig. 6.15.a, the possible range in Q^2, as a function of p_T, when $0.5 < \frac{p_T^2}{Q^2} < 2$, is illustrated. With a finite resolution in p_T, a broad variation in the Q^2 cross-section is possible, leaving us highly sensitive to the $\frac{1}{Q^4}$ dependence of the total cross-section in eq. (2.8). The $\frac{{p_{T,FWD}}^2}{Q^2}$ is however reasonably well described by ARIADNE, also outside of the cuts (see fig. 6.15.b). We

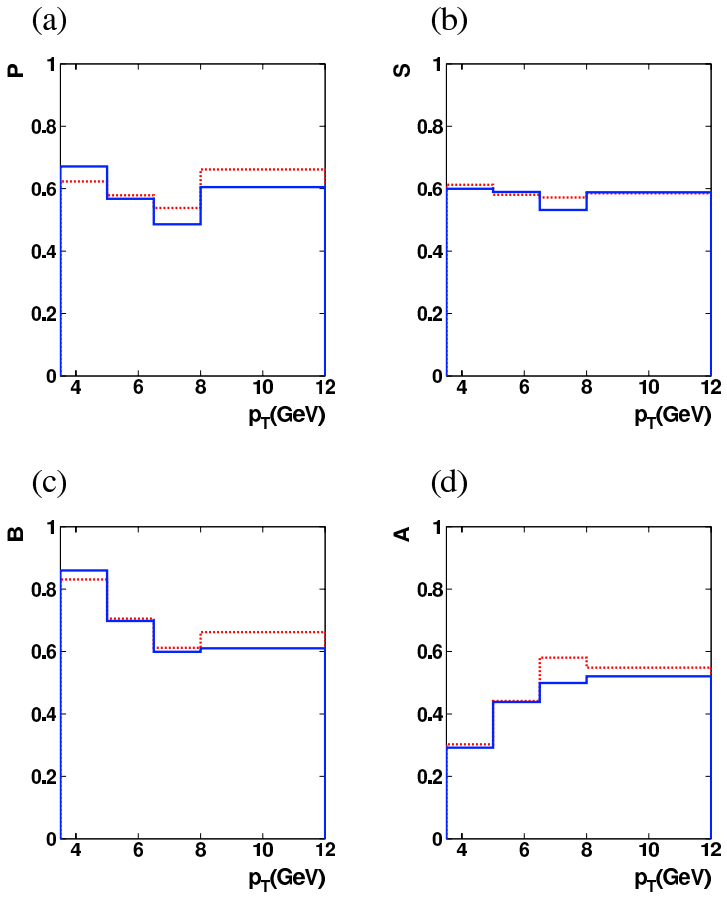

Figure 6.13: *The forward jet DIS event* (a) *purity,* P*,* (b) *stability,* S*,* (c) *background,* B*, and* (d) *acceptance,* A*, calculated in bins of* $p_{T,FWD}$*. The predictions from Monte Carlo generators ARIADNE (full line) and RAPGAP (dashed line) are shown.*

note that the RAPGAP and ARIADNE predictions give similar values of the resolution, which may be due to a good description of the inclusive cross-section.

6.6.2 Detector Correction

In order to make a reliable detector correction, we want the detector simulated Monte Carlo predictions to be able to describe the properties of experimental data, as given by the detector. In fig. 6.16, uncorrected data is compared to detector simulated RAPGAP and ARIADNE Monte Carlo data, for forward jet DIS events. To compare the characteristic shape of the quantities to be measured, we have rescaled the Monte Carlo distributions to the data, which are normalised to its luminosity, L. The distributions in Bjoerken-x, forward jet p_T and x_{JET} are investigated, showing discrepancies between the RAPGAP results and experimental data, while ARIADNE often provides an reasonable detector level description.

The correction from detector to hadron level of the distributions measured, is carried out

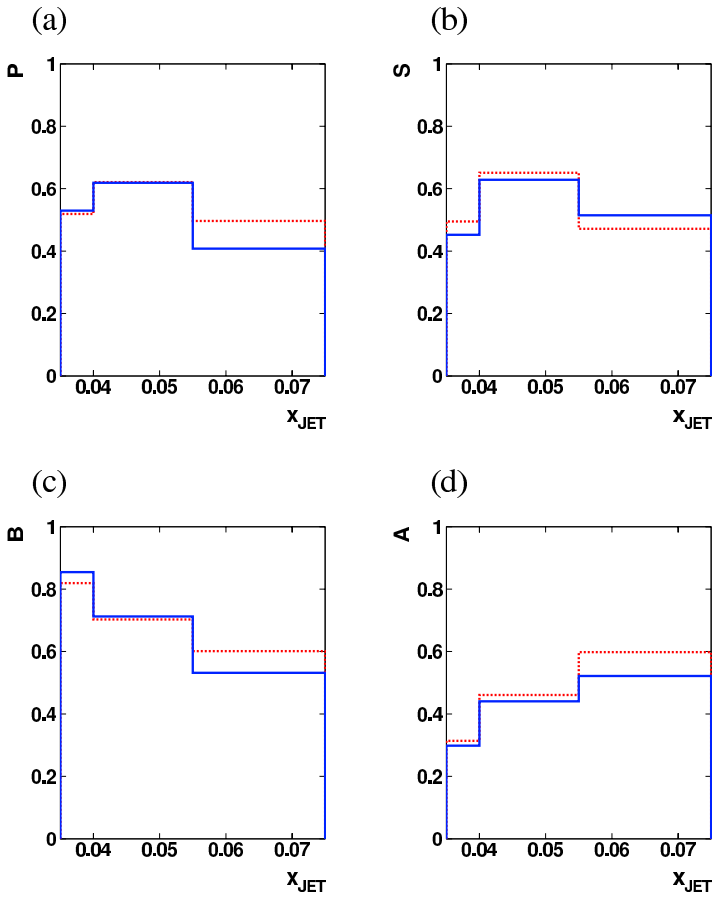

Figure 6.14: *The forward jet DIS event* (a) *purity,* P, (b) *stability,* S, (c) *background,* B, *and* (d) *acceptance,* A, *calculated in bins of* x_{JET}. *The predictions from Monte Carlo generators ARIADNE (full line) and RAPGAP (dashed line) are shown.*

according to a bin-by-bin procedure. The correction includes QED radiation from the incoming and scattered positron i.e. the correction is done directly to the non-radiative hadron level. This means that for each bin, we define the correction factor, C, as:

$$C = \frac{N_{HAD}^{NRAD}}{N_{DET}} \quad , \tag{6.13}$$

where N_{DET} is the number of events found in a certain bin on detector level and N_{HAD}^{NRAD} the number of events found in the corresponding bin on non-radiative hadron level. The correction factor for the distributions in Bjoerken-x, $p_{T,FWD}$ and x_{JET} are shown in fig. 6.17. We see that the correction, for all quantities and in most bins, obtained from the ARIADNE Monte Carlo is smaller i.e. the correction factor is closer to unity, than the correction obtained for the RAPGAP Monte Carlo. As noted previously, the ARIADNE MC provides a markedly better detector level description than the RAPGAP MC does. We will therefore use ARIADNE exclusively for our correction of the data. The difference between the two Monte Carlos will then be used as an estimate of the model dependence of the detector correction, to be added as a systematic error.

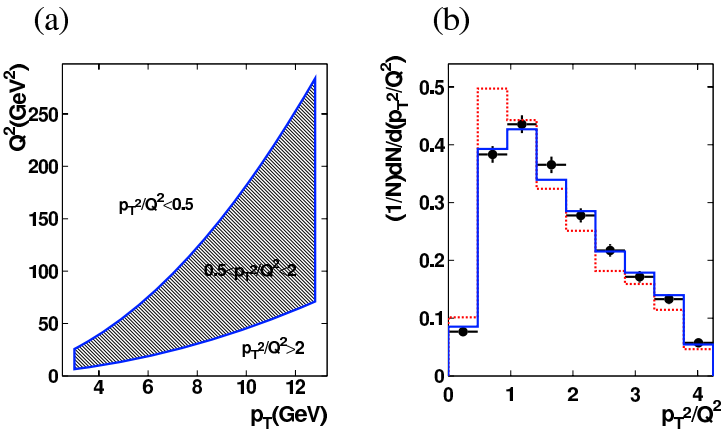

Figure 6.15: *The $\frac{p_T^2}{Q^2}$ cut. (a) The possible range in Q^2 for different values of p_T when requiring $0.5 < \frac{p_T^2}{Q^2} < 2$. (b) Detector level distribution for forward jet DIS events, showing $\frac{{p_{T,FWD}}^2}{Q^2}$, for the full range in this variable. Experimental data (dots) are compared to detector simulated Monte Carlo data from ARIADNE (full line) and RAPGAP (dashed line). The distribution is normalised to the number of events selected, N.*

6.6.3 Systematic Errors

We have estimated the model dependence of the detector correction by taking the difference between the correction factors obtained from the ARIADNE and the RAPGAP Monte Carlos as the systematic error. The error from the model dependence constitutes the largest contribution to the overall systematic error and is on average ± 9 %.

The second largest contribution to the total systematic error arises from the dependence of the event reconstruction at the detector level on the hadronic energy scale. The energy of the clusters found in the LAr calorimeter is only known to an accuracy of ± 4 %. Thus, the uncertainty in the measured cross-section coming from the uncertainty in the energy scale, can be estimated by changing the energy scale by this percentage and calculating the change to the cross-section. This gives an average systematic error of -7/+8 %.

In the same way as the energy scale of the LAr calorimeter gives rise to a systematic error, we need to estimate an error also for the SpaCal electromagnetic calorimeter. The energy scale of this calorimeter is known to within ± 1 %. We hence change the scale of this detector by $\pm$ 1% and use the change in the cross-section as an estimate of the error. This error is on average ± 2 %.

Another systematic error comes from the uncertainty in the measurement of the polar angle, θ_e, of the positron, which is ± 2 $mrad$. We thus change the positron angle with these values and calculate the effect this has on the final forward jet event cross-sections. The average systematic error from this source is $\pm$ 2%.

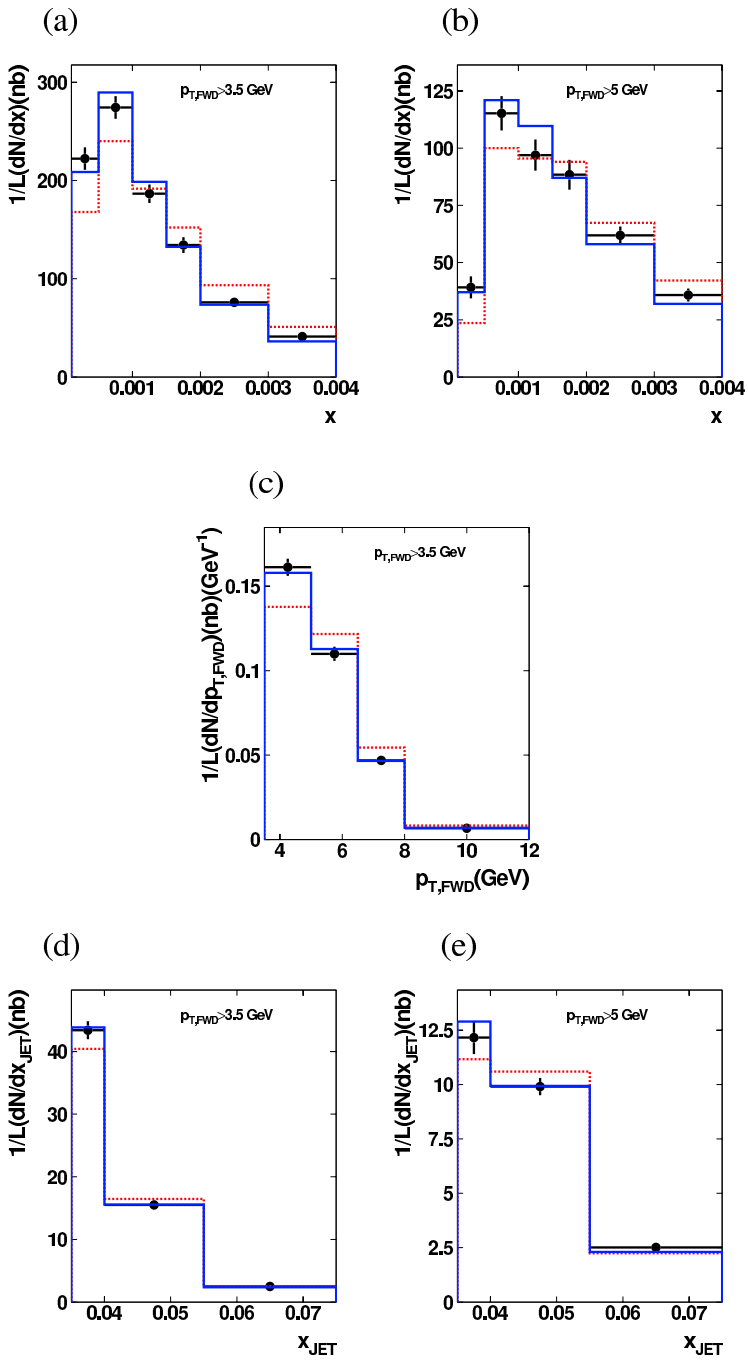

Figure 6.16: *Detector level distributions for forward jet DIS events, showing* (a) *Bjoerken-*x *demanding a forward jet* $p_T > 3.5\ GeV$, (b) *Bjoerken-*x *demanding a forward jet,* $p_T > 5\ GeV$, (c) $p_{T,FWD}$ $(p_{T,FWD} > 3.5\ GeV)$, (d) x_{JET} *demanding a forward jet* $p_T > 3.5\ GeV$ *and* (e) x_{JET}, *demanding a forward jet* $p_T > 5\ GeV$. *Experimental data (dots) are compared to detector simulated Monte Carlo from ARIADNE (full line) and RAPGAP (dashed line). The distributions have been scaled to the data, which are normalised to the luminosity,* L.

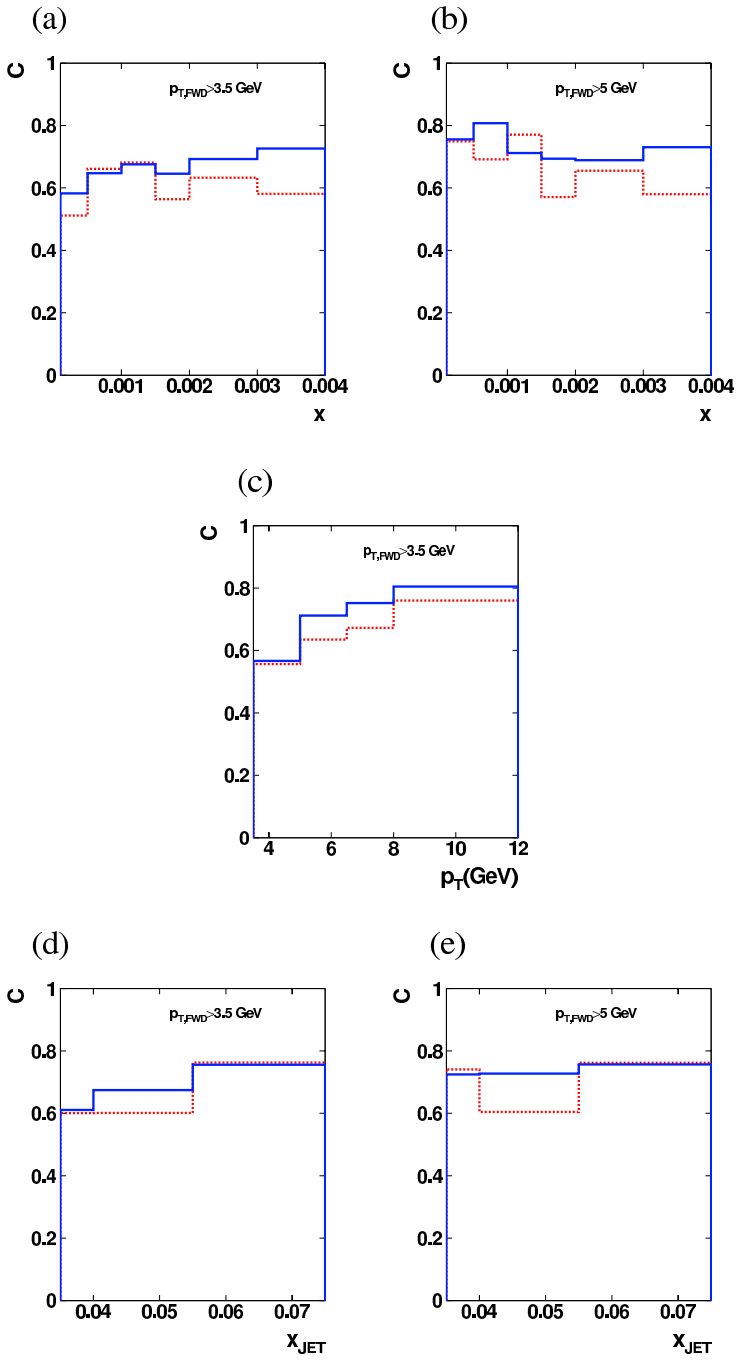

Figure 6.17: *The correction factor, C, for forward jet DIS events, shown as a function of (a) Bjoerken-x, demanding a forward jet $p_T > 3.5\ GeV$, (b) Bjoerken-x, demanding a forward jet $p_T > 5\ GeV$, (c) $p_{T,FWD}$ ($p_{T,FWD} > 3.5\ GeV$), (d) x_{JET}, demanding a forward jet $p_T > 3.5\ GeV$ and (e) x_{JET}, demanding a forward jet $p_T > 5\ GeV$. The predictions from Monte Carlo generators ARIADNE (full line) and RAPGAP (dashed line) are shown.*

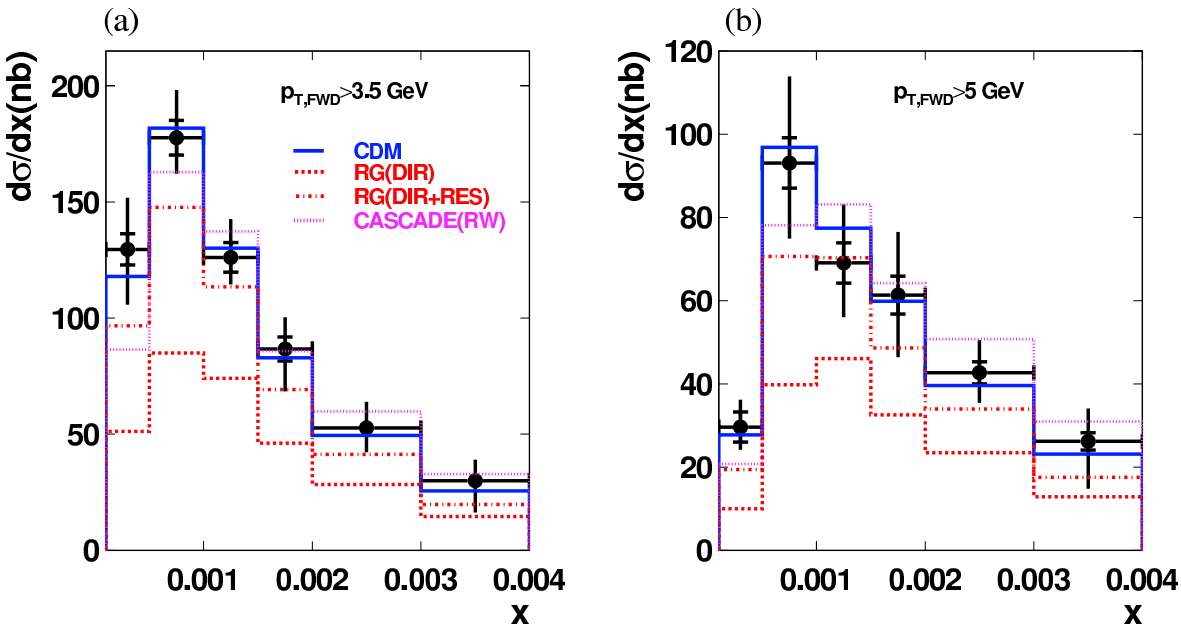

Figure 6.18: *The forward jet DIS event differential cross-section, shown as a function of Bjoerken-x, requiring a forward jet transverse momentum* (a) $p_{T,FWD} > 3.5\ GeV$ *and* (b) $p_{T,FWD} > 5\ GeV$.

We have also studied the contribution of photoproduction to the forward jet cross-section, using the PHOJET [65] Monte Carlo generator, and estimated the uncertainty due to this to this background as 1%.

6.6.4 Differential Cross-Section

The differential forward jet event cross-section as a function of the variables Bjoerken-x, x_{JET} and $p_{T,FWD}$ are presented in fig. 6.18-6.20. Data corrected to the hadron level are compared to the predictions of the Monte Carlo generators presented in section 6.1.

The RAPGAP standard DGLAP prediction of the forward jet event cross-section clearly falls below the data for all different quantities investigated, and in nearly all bins. The description provided by *RG(DIR)* is however, as expected, closer to data with increasing values of Bjoerken-x.

The cross-section of *RG(DIR+RES)*, based on DGLAP including the contribution of a resolved component of the virtual photon, is often close to that of data and sometimes shows agreement within the systematic errors. For lower values of Bjoerken-x, x_{JET} and $p_{T,FWD}$ however, the differences from data increase.

ARIADNE, based on the colour dipole model, gives a very good description of the data. The CDM prediction is often in agreement with the cross-section of data within the statistical errors.

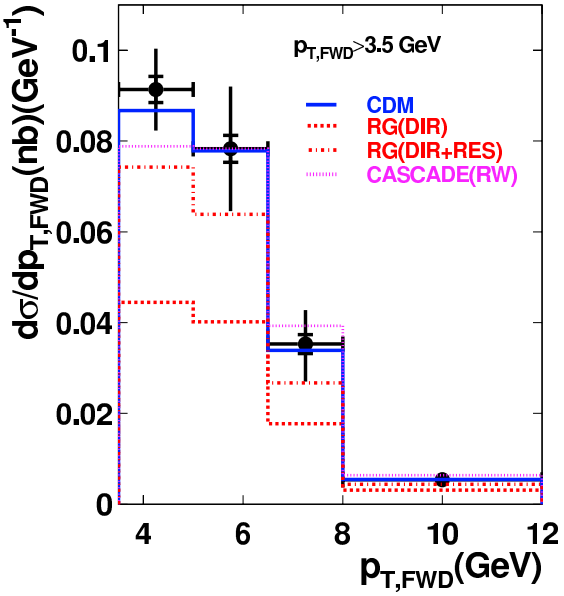

Figure 6.19: *The forward jet DIS event differential cross-section, shown as a function of* $p_{T,FWD}$ *(*$p_{T,FWD} > 3.5\ GeV$*).*

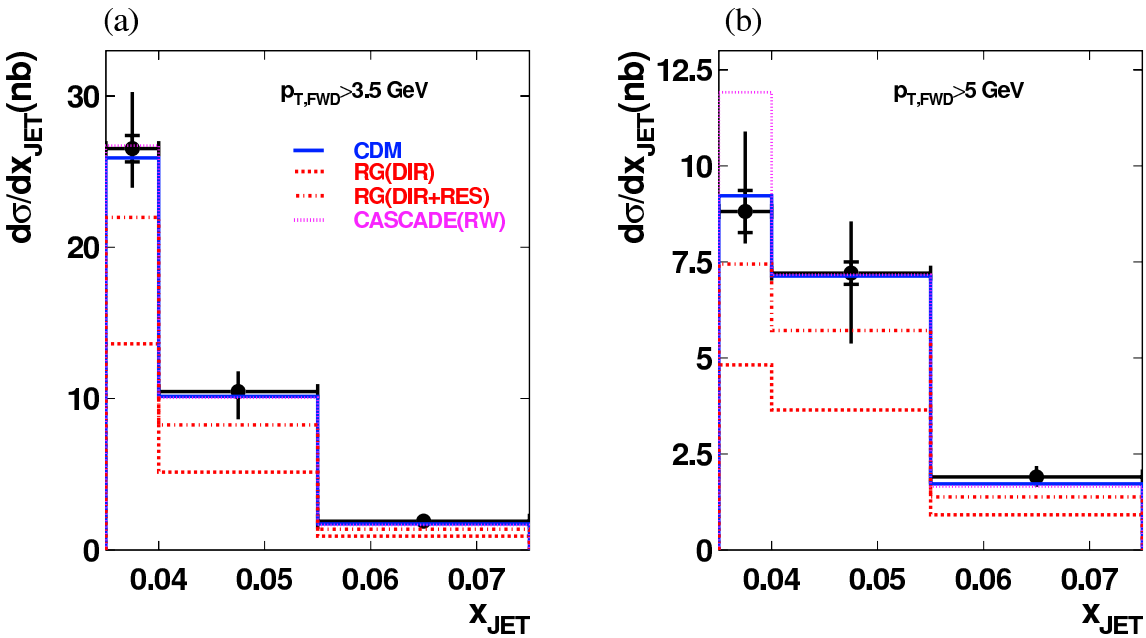

Figure 6.20: *The forward jet DIS event differential cross-section shown as a function of* x_{JET}*, requiring a forward jet transverse momentum* (a) $p_{T,FWD} > 3.5\ GeV$ *and* (b) $p_{T,FWD} > 5\ GeV$*.*

The quality of the description is similar for the different distributions and for both $p_{T,FWD}$ cut-offs.

The cross-section of CASCADE overshoots that of data. We have, as to be able to make a comparison between the shapes of the distributions given by data and by CASCADE, reweighted the results of CASCADE by a factor 0.6, and we refer to these results as *CASCADE(RW)*. We see that the shape of *CASCADE(RW)* agrees with that of data in a majority of the bins of the measurement. The problem of the description is to a large extent a normalisation issue, possibly related to the scale of α_s,in the evolution, which is presently under study [66].

6.7 2+Forward Jet Event Cross-section Measurement

Extending the analysis of the standard forward jet cross-section, we have measured the cross-section of events, where, in addition to a forward jet, two "hard" jets are found. We apply the DIS and forward jet event selection previously described, adding the di-jet selection described in section 6.5. The class of events thereby selected are referred to as 2+forward jet events. Investigating such events, we gain further information on the development of the QCD cascade and the parton dynamics of low-x processes.

The quality of the event selection is investigated in section 6.7.1. The detector level distributions and the correction to the hadron level is presented in section 6.7.2. The systematic errors of the measurement are presented in section 6.7.3. The 2+forward jet event cross-section is presented as a function of three different quantities, x, $p_{T,FWD}$ and x_{JET}, and data are compared to generator predictions based on different evolution schemes, in section 6.6.4.

6.7.1 Purity, Stability, Background and Acceptance

We study the quality of the 2+forward jet event selection, for the same bin division that will used in the measurement of the Bjoerken-x, $p_{T,FWD}$ and x_{JET} differential cross-sections. The purity, P, stability, S, background, B, and acceptance, A, defined according to eq. (6.9-6.12), and calculated in bins of Bjoerken-x, are shown in fig. 6.21. The purity and stability of Bjoerken-x tend to be larger than 0.6, and for some bins reach 0.8-0.9, as was the case for the standard forward jet selection. We note that the RAPGAP prediction gives a higher purity and stability for 2+forward jet events than for the standard forward jet selection. The background is large in all bins, and the acceptance becomes increasingly low with lower values of x.

The purity, stability, background and acceptance, for the variables $p_{T,FWD}$ and x_{JET}, are plotted in fig. 6.22 and 6.23. As for the standard forward jet event selection, the purities and stabilities are reasonable, but the background increases and the acceptance becomes lower when the cut-off values of $p_{T,FWD}$ and x_{JET} are approached, indicating smearing effects.

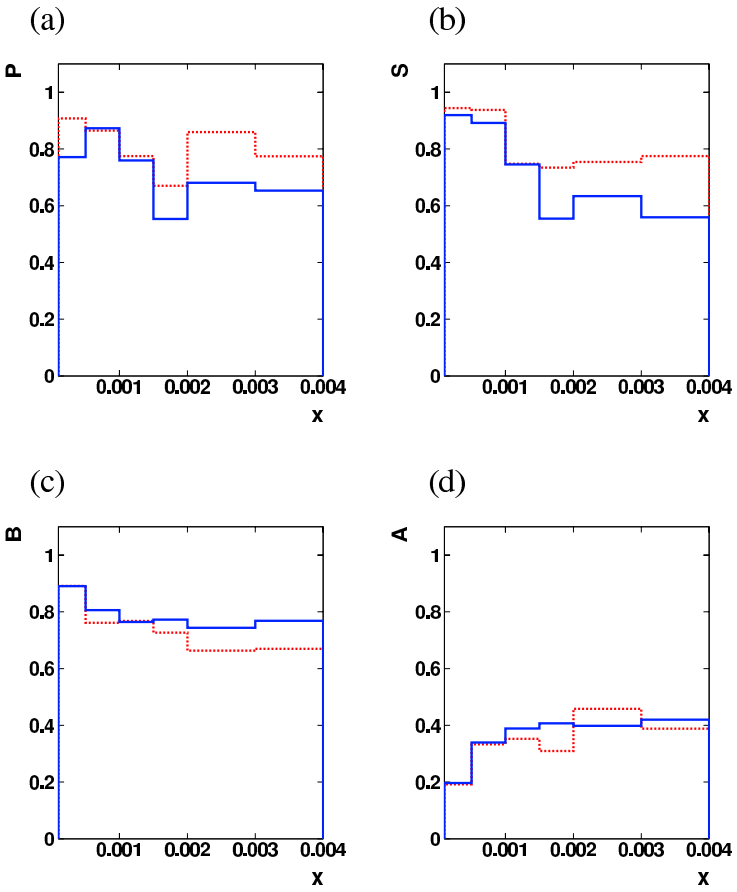

Figure 6.21: *The 2+forward jet DIS event* (a) *purity,* P*,* (b) *stability,* S*,* (c) *background,* B*, and* (d) *acceptance,* A*, calculated in bins of Bjoerken-*x*. The predictions from Monte Carlo generators ARIADNE (full line) and RAPGAP (dashed line) are shown.*

6.7.2 Detector Correction

The detector level description of 2+forward jet DIS events are studied in fig. 6.24, where experimental data are compared to predictions from the ARIADNE and RAPGAP Monte Carlo generators, that have undergone detector simulation. The distributions shown are scaled to the luminosity of the data. Compared to the standard forward jet event selection, the data show less of agreement with the description provided by the ARIADNE Monte Carlo generator, and more with the predictions of RAPGAP, than before. ARIADNE does however still provide a reasonable description of the detector level quantities.

The correction of data is in this measurement, as for the standard forward jet cross-section measurement, carried out according to a bin-by-bin procedure, including QED radiation from the incoming and scattered positron. The correction factor, C, is defined according to eq. (6.13). The correction factors of the quantities we measure are shown in fig. 6.25. The RAPGAP Monte Carlo generator provides a correction factor that often has a value closer to unity than in the standard forward jet measurement. Fluctuations between adjacent bins, can be noticed in the

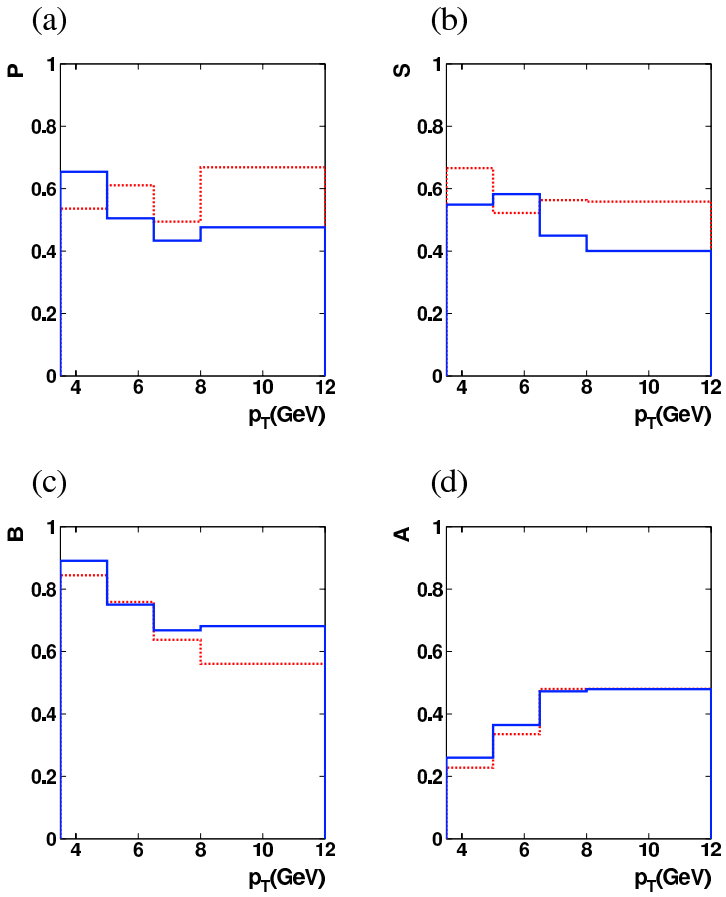

Figure 6.22: *The 2+forward jet DIS event* (a) *purity,* P, (b) *stability,* S, (c) *background,* B, *and* (d) *acceptance,* A, *calculated in bins of* $p_{T,FWD}$. *The predictions from Monte Carlo generators ARIADNE (full line) and RAPGAP (dashed line) are shown.*

RAPGAP correction factor, for the RAPGAP sample used, due to the highly exclusive cuts of the 2+forward jet selection. The correction factor given by the ARIADNE Monte Carlo generator, however, is sometimes lower than in the previous measurement, but has a value that is above 0.5 for all quantities and in all bins. For reasons of congruity between the measurements, we use ARIADNE exclusively for the correction of the data also in this measurement. The difference between the correction factors given by the two Monte Carlos will again be used as an estimate of the model dependence of the correction, to be added as a systematic error.

6.7.3 Systematic Errors

The estimate of the systematic errors of the 2+forward jet event cross-section measurement is carried out in the same way as in the previous measurement, described in section 6.6.3. We obtain the following systematic errors:

- The systematic error from the model dependence of the correction is on average ± 15 %.

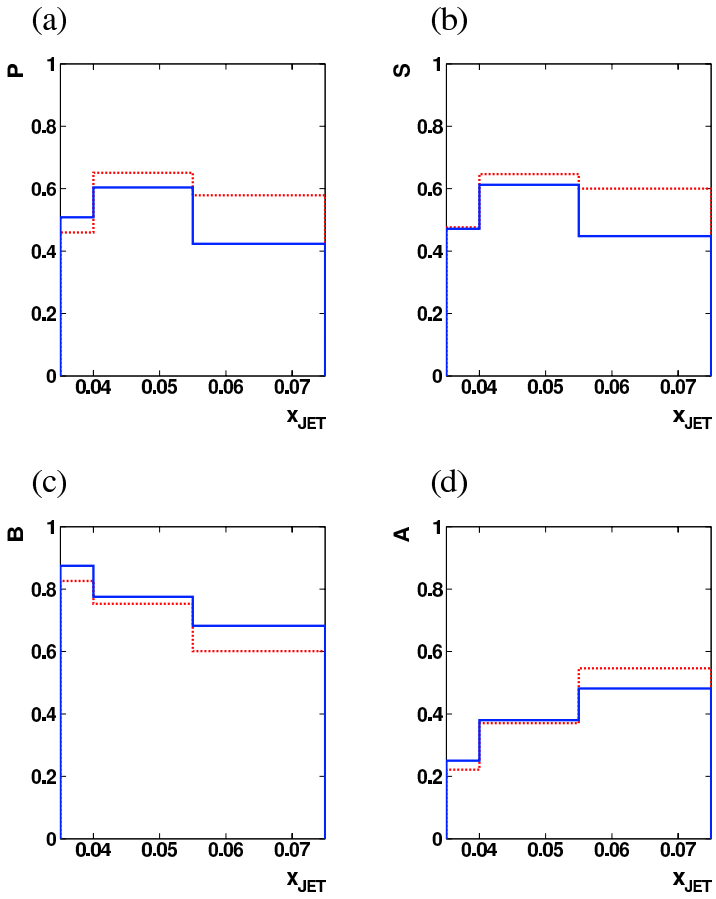

Figure 6.23: *2+forward jet DIS event* (a) *purity,* P*,* (b) *stability,* S*,* (c) *background,* B *and* (d) *acceptance,* A*, calculated in bins of* x_{JET}*. The predictions from Monte Carlo generators ARIADNE (full line) and RAPGAP (dashed line) are shown.*

- The systematic error due to the uncertainty in the LAr calorimeter energy scale is on average -7/+14 %.
- The systematic error due to the uncertainty in the SpaCal electromagnetic calorimeter energy scale is on average ± 2 %.
- The systematic error from the measurement of the polar angle, θ_e, of the positron is on average -1/+2%.

6.7.4 Differential Cross-Section

The 2+forward jet event differential cross-section is presented as a function of variables Bjoerken-x, x_{JET} and $p_{T,FWD}$ in fig. 6.26-6.28. Data corrected to the hadron level are compared to the predictions from the Monte Carlo generators presented in section 6.1.

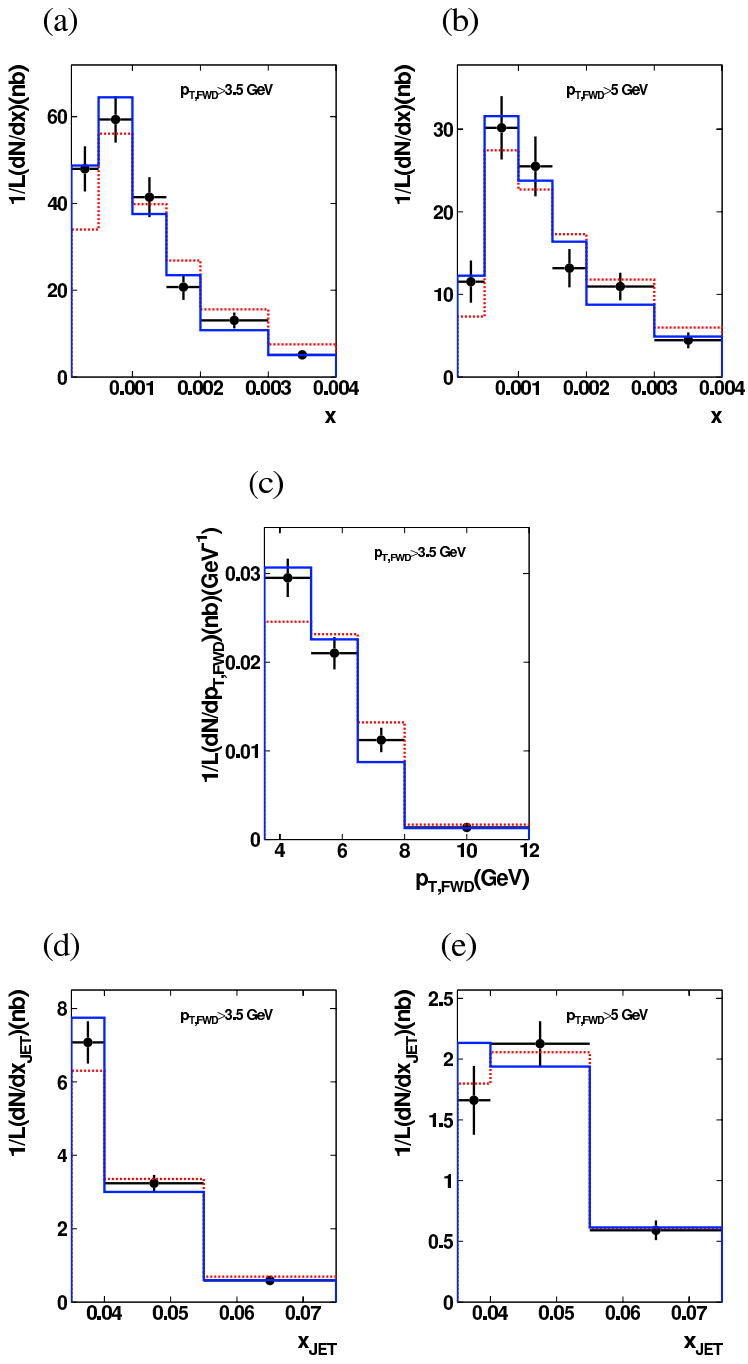

Figure 6.24: *Detector level distributions for 2+forward jet DIS events, showing* (a) *Bjoerken-*x*, demanding a forward jet* $p_T > 3.5\ GeV$, (b) *Bjoerken-*x*, demanding a forward jet,* $p_T > 5\ GeV$, (c) $p_{T,FWD}$ ($p_{T,FWD} > 3.5\ GeV$), (d) x_{JET}, *demanding a forward jet* $p_T > 3.5\ GeV$ *and* (e) x_{JET}, *demanding a forward jet* $p_T > 5\ GeV$. *Experimental data (dots) are compared to detector simulated Monte Carlo data from ARIADNE (full line) and RAPGAP (dashed line). The distributions have been scaled to the data, which are normalised to the luminosity,* L.

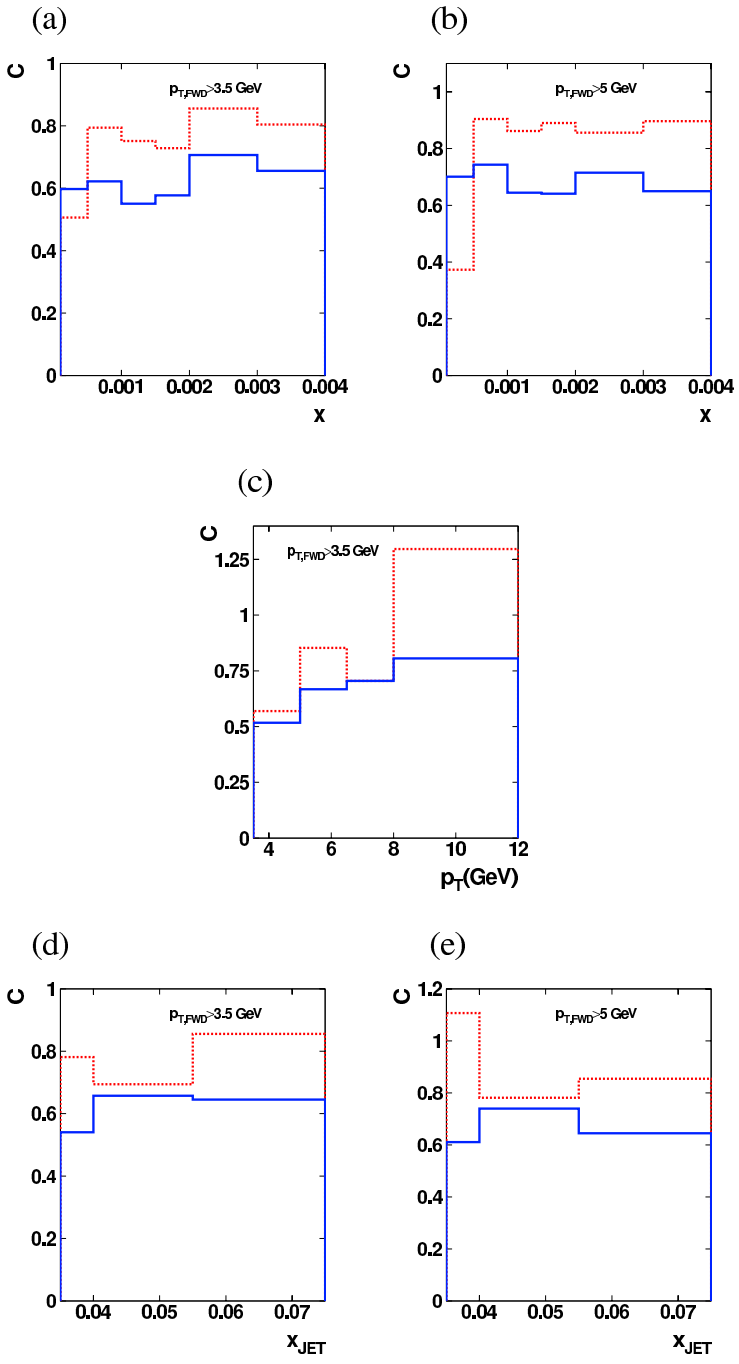

Figure 6.25: *The correction factor, C, for 2+forward jet DIS events, shown as a function of (a) Bjoerken-x demanding a forward jet $p_T > 3.5\ GeV$, (b) Bjoerken-x demanding a forward jet $p_T > 5\ GeV$, (c) $p_{T,FWD}$ ($p_{T,FWD} > 3.5\ GeV$), (d) x_{JET}, demanding a forward jet $p_T > 3.5\ GeV$ and (e) x_{JET}, demanding a forward jet $p_T > 5\ GeV$. The predictions from ARIADNE (full line) and RAPGAP (dashed line) Monte Carlo are shown.*

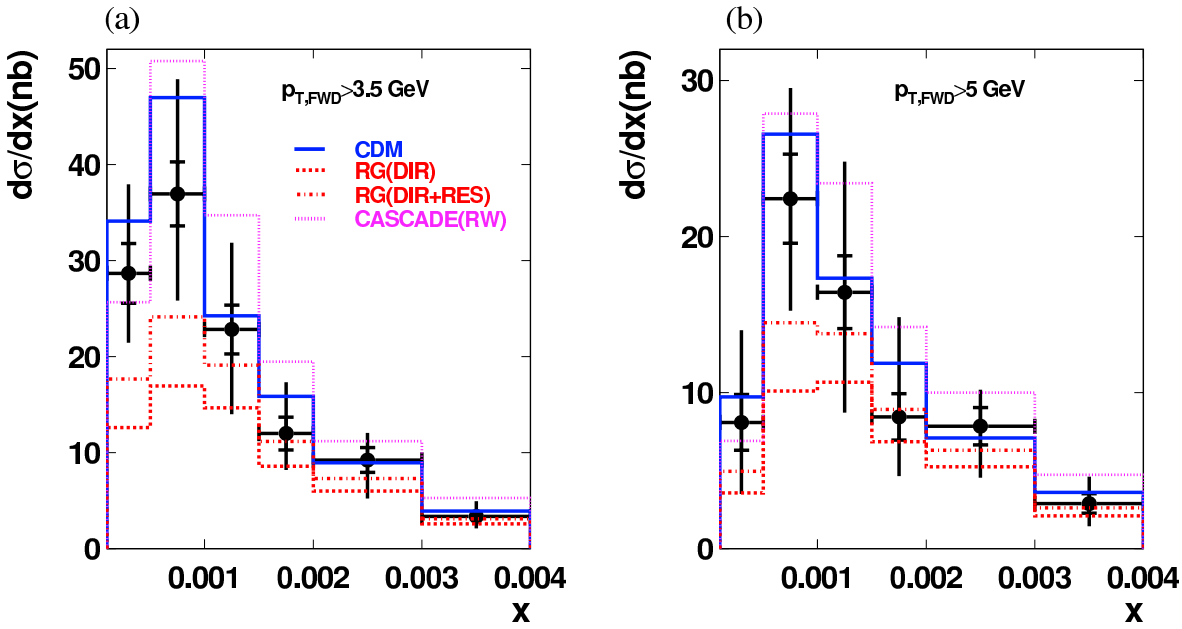

Figure 6.26: *The 2+forward jet DIS event differential cross-section shown as a function of Bjoerken-x, requiring a forward jet transverse momentum* (a) $p_{T,FWD} > 3.5\ GeV$ *and* (b) $p_{T,FWD} > 5\ GeV$.

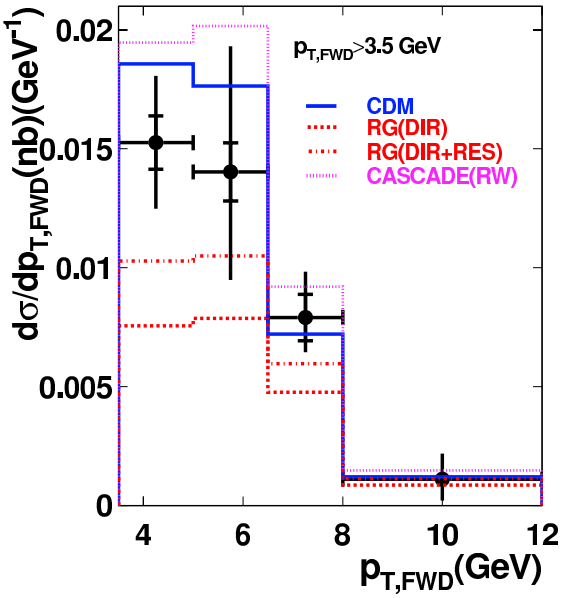

Figure 6.27: *The 2+forward jet DIS event differential cross-section shown as a function of* $p_{T,FWD}$, $(p_{T,FWD} > 3.5\ GeV)$.

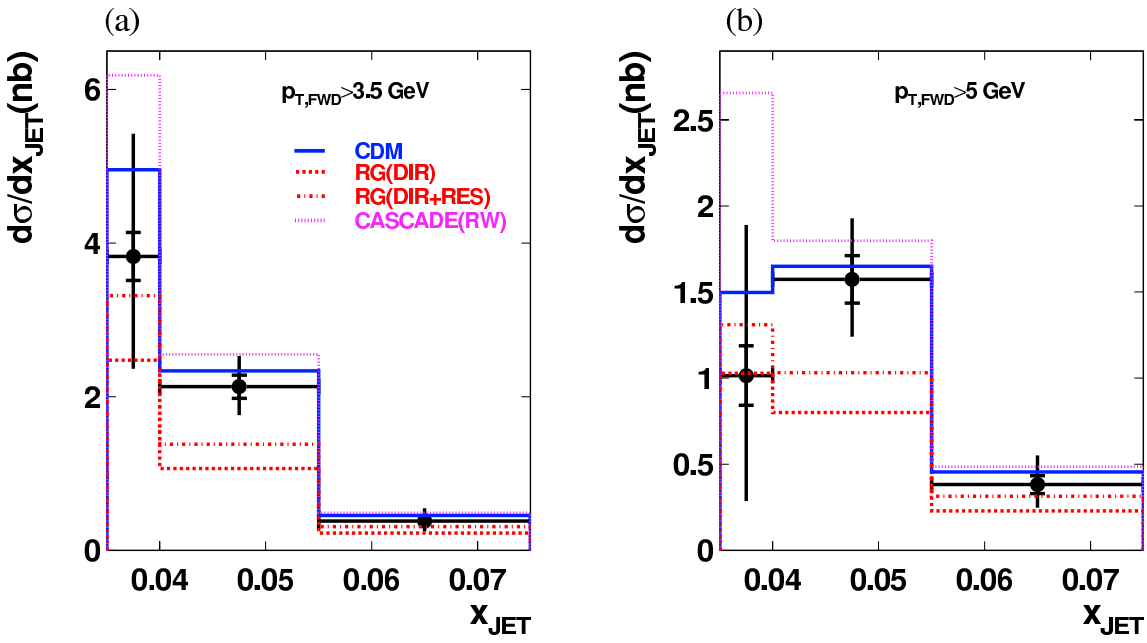

Figure 6.28: *The 2+forward jet DIS event differential cross-section shown as a function of* x_{JET}*, requiring a forward jet transverse momentum* (a) $p_{T,FWD} > 3.5\,GeV$ *and* (b) $p_{T,FWD} > 5\,GeV$.

The 2+forward jet event cross-section from standard DGLAP often shows, as for the standard forward jet cross-section measurement, differences from the cross-section of data, in the region of lower Bjoerken-x and for lower values of $p_{T,FWD}$. For higher values of Bjoerken-x, the predictions are however within the errors of the data. For x_{JET}, *RG(DIR)* deviates clearly from the data in the middle bin of our measurement, but is within the errors of data for the lower bin.

RG(DIR+RES) often gives a description within the systematic errors of the data Bjoerken-x differential cross-section, but shows discrepancies for lower values of this variable. It also, as *RG(DIR)*, shows clear discrepancies in x_{JET}, for the middle bin of our measurement in this variable.

The description of data provided by ARIADNE is now less accurate than was the case for the standard forward jet measurement. The *CDM* cross-section is often outside the statistical errors of data, but however still within systematic errors for all bins of the Bjoerken-x and x_{JET} distributions. In the lowest bin of $\frac{d\sigma}{dp_T}$ the *CDM* discrepancy to data is larger than the error of the measurement.

The shape of the reweighted CASCADE cross-section is now less in agreement with that of data, than was the case in the standard forward jet measurement. Also the x_{JET} distribution of data shows a clear deviation from the shape of *CASCADE(RW)*, whereas in the standard forward jet measurement, the shape was well described.

6.8 Forward and Hard Jet η Measurement

We now study 2+forward jet events and measure the event cross-section as a function of the forward jet rapidity, η_{FWD} and the individual "hard" jet rapidities, η_{HARD1} and η_{HARD2}. Hereby, the defining angular characteristics of the QCD cascade in forward jet events are investigated. The jet rapidities are measured for different distances in rapidity between the two "hard" jets defined in the events, $\Delta\eta$. By applying different requirements in $\Delta\eta$, we expect to be sensitive to different parton ladder structures and low-x dynamics, and possibly we will be able to differentiate between BFKL-like processes and the ladder structure expected in resolved photon processes.

The quality of the measurement is investigated in section 6.8.1. The detector level distributions, and the corrections to the hadron level are presented in section 6.8.2. The systematic errors of the measurement are discussed in section 6.8.3. The 2+forward jet event cross-section is presented as a function of η_{FWD}, η_{HARD1} and η_{HARD2}, and data are compared to generator predictions based on different evolution schemes, in section 6.6.4. The hadron level cross-sections are presented, and data are compared to generator predictions in section 6.8.4.

6.8.1 Purity, Stability, Background and Acceptance

Investigating the quality of the 2+forward jet event selection used in this measurement, we define purity, P, stability, S, background, B, and acceptance, A, according to eq. (6.9-6.12). These quantities are calculated in bins of forward jet rapidity, η_{FWD}, in fig. 6.29, of the rapidity "hard" jet closest in rapidity to the photon, η_{HARD1}, in fig. 6.30, and of the rapidity of the "hard" jet closest in rapidity to the forward jet, η_{HARD2}, in fig. 6.31. The purity and stability of the forward jet tends to vary between values of 0.6 and 0.8, and the "hard" jets show purities and stabilities between 0.8 and close to unity. As in previous measurements, the background is high, here around 0.8 for all jets. The acceptance for the 2+forward jet selection lies between 0.3 and 0.4, for the binning of our measurement.

6.8.2 Detector Correction

The description of η provided by the detector, for the 2+forward jet event selection is investigated in fig. 6.32. Experimental data are compared to predictions from the ARIADNE and RAPGAP Monte Carlo generators, that have undergone detector simulation. We study the rapidity of the "hard" jets and the forward jet, first applying no $\Delta\eta$ requirement, then applying a $\Delta\eta < 1$ and a $\Delta\eta > 1$ requirement. The distributions shown are scaled to the luminosity of the data, and the shape of the η distributions is investigated. We see, as for the variables previously investigated for the 2+forward jet selection, that ARIADNE tends to provide a reasonable detector level description also of the jet rapidity distributions of data.

As before, we calculate the correction factor, C, according to eq. (6.13). The correction factors for the different jet rapidity distributions are shown in fig. 6.33. The predictions of the RAPGAP Monte Carlo generator tends to give a reasonable correction, but the value of the correction factor is below 0.2 in one of the bins of the measurement. The correction factor given by the ARIADNE Monte Carlo is sometimes lower than that of RAPGAP, but has a value that is

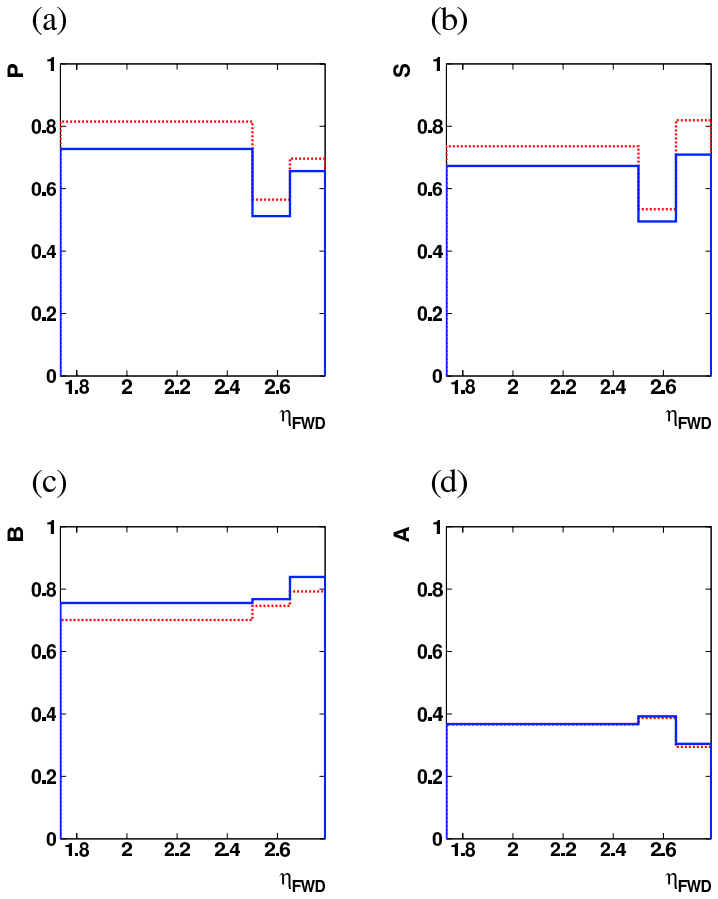

Figure 6.29: *The 2+forward jet DIS event* (a) *purity,* P*,* (b) *stability,* S*,* (c) *background,* B*, and* (d) *acceptance,* A*, calculated in bins of* η_{FWD}*. The predictions of Monte Carlo generators ARIADNE (full line) and RAPGAP (dashed line) are shown.*

above 0.3 for all quantities and in all bins. Since ARIADNE also gives a description closer to the data on detector level than RAPGAP does, we will as in previous measurements use ARIADNE exclusively for the correction of the data to hadron level. The difference between the correction factor provided by the ARIADNE and RAPGAP predictions is as before used to approximate the error from the model dependence of the correction.

6.8.3 Systematic Errors

The estimate of the systematic errors of the 2+forward jet event cross-section measurement as a function of the jet rapidities is carried out in the same way as in the previous measurements, as described in section 6.6.3. We obtain the following systematic errors:

- The systematic error from the model dependence of the correction is on average ± 9 %.
- The systematic error due to the uncertainty in the LAr calorimeter energy scale is on average -6/+8 %.

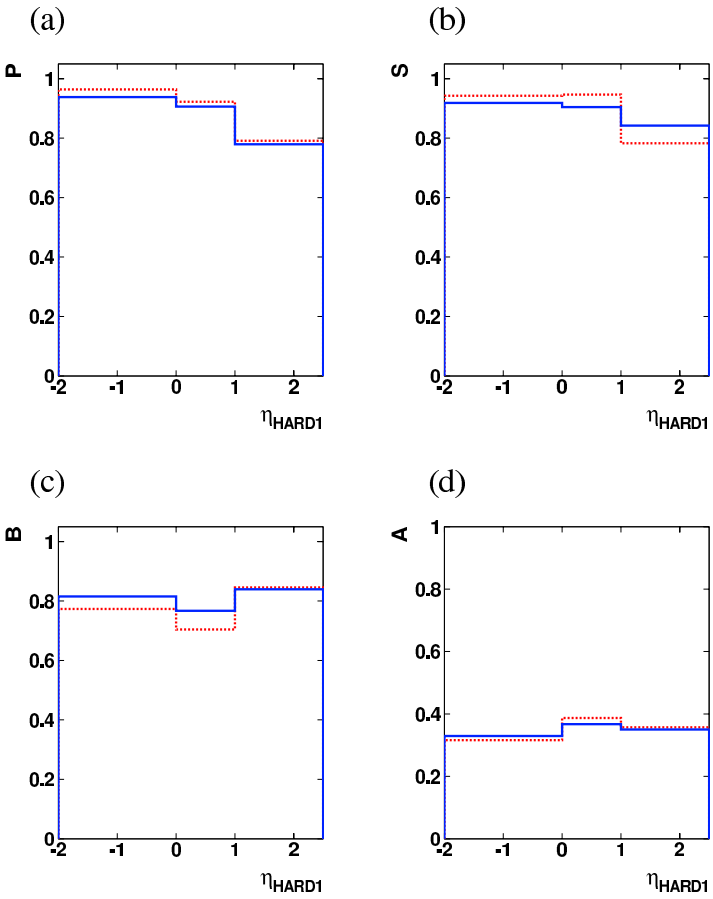

Figure 6.30: *The 2+forward jet DIS event* (a) *purity,* P*,* (b) *stability,* S*,* (c) *background,* B*, and* (d) *acceptance,* A*, calculated in bins of* η_{HARD1}*. The predictions from Monte Carlo generators ARIADNE (full line) and RAPGAP (dashed line) are shown.*

- The systematic error due to the uncertainty in the SpaCal electromagnetic calorimeter energy scale is on average ± 2 %.
- The systematic error from the measurement of the polar angle, θ_e, of the positron is on average ± 1 %.

6.8.4 Differential Cross-Section

The differential 2+forward jet event cross-section is presented as a function of rapidity, for different configurations of the distance in rapidity between the two "hard" jets of an event, in fig. 6.34. Data corrected to the hadron level are compared to generator predictions.

The 2+forward jet event cross-section from standard DGLAP tends to fail in describing the rapidity distributions of the forward jet and the "hard" jets in a 2+forward jet event. We note however that the description given by *RG(DIR)* is closest to data when $\Delta\eta > 1$.

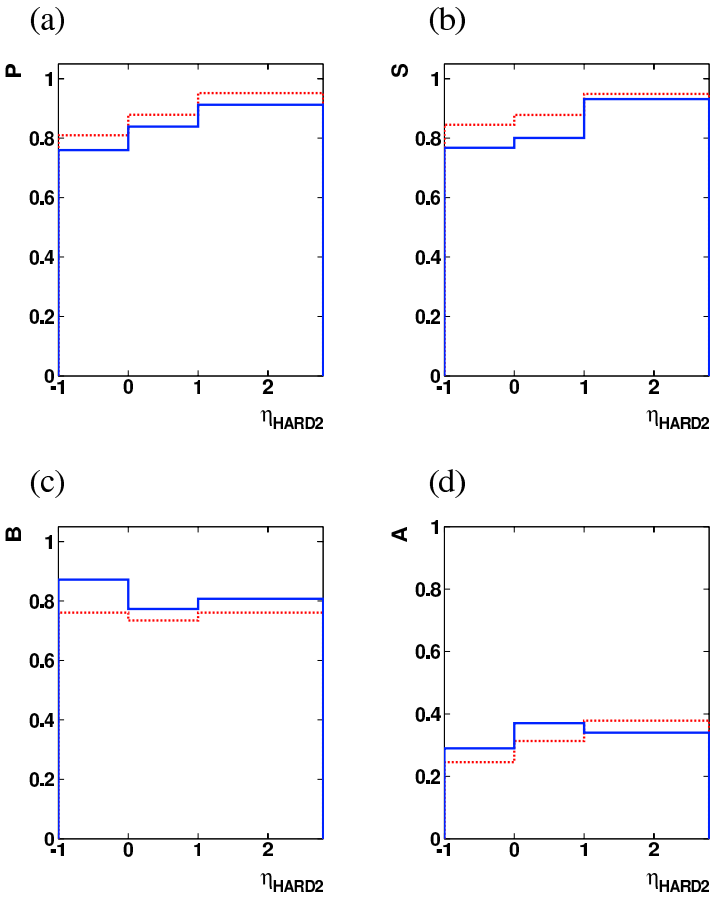

Figure 6.31: *The 2+forward jet DIS event* (a) *purity,* P, (b) *stability,* S, (c) *background,* B, *and* (d) *acceptance,* A, *calculated in bins of* η_{HARD2}. *The predictions from Monte Carlo generators ARIADNE (full line) and RAPGAP (dashed line) are shown.*

The *RG(DIR+RES)* cross-section, as a function of η_{HARD1} or η_{HARD1} often describes that of data reasonably well, for lower values of these variables. Requiring $\Delta\eta < 1$, the description of η_{FWD}, provided by *RG(DIR+RES)* becomes inadequate. With a $\Delta\eta > 1$ requirement applied, however, *RG(DIR+RES)* gives the closest description of the forward jet, indicating that the parton dynamics of events in which the photon is resolved are enhanced by applying this cut.

The description of jet rapidity provided by CDM, is often reasonable, when applying no $\Delta\eta$ requirement. When requiring that $\Delta\eta < 1$, the CDM cross-section is often within the statistical errors and always within systematic errors of data, providing clearly the best description of the forward jet. This may be taken as an indication of processes with less of ordering in propagator virtuality being selected through this requirement. Applying a $\Delta\eta > 1$ requirement, the description is however sometimes outside the errors of data.

The results of the CASCADE generator, reweighted by a factor 0.6, *CASCADE(RW)*, often show a difference in shape from the data, but provide an, in many cases, reasonable description

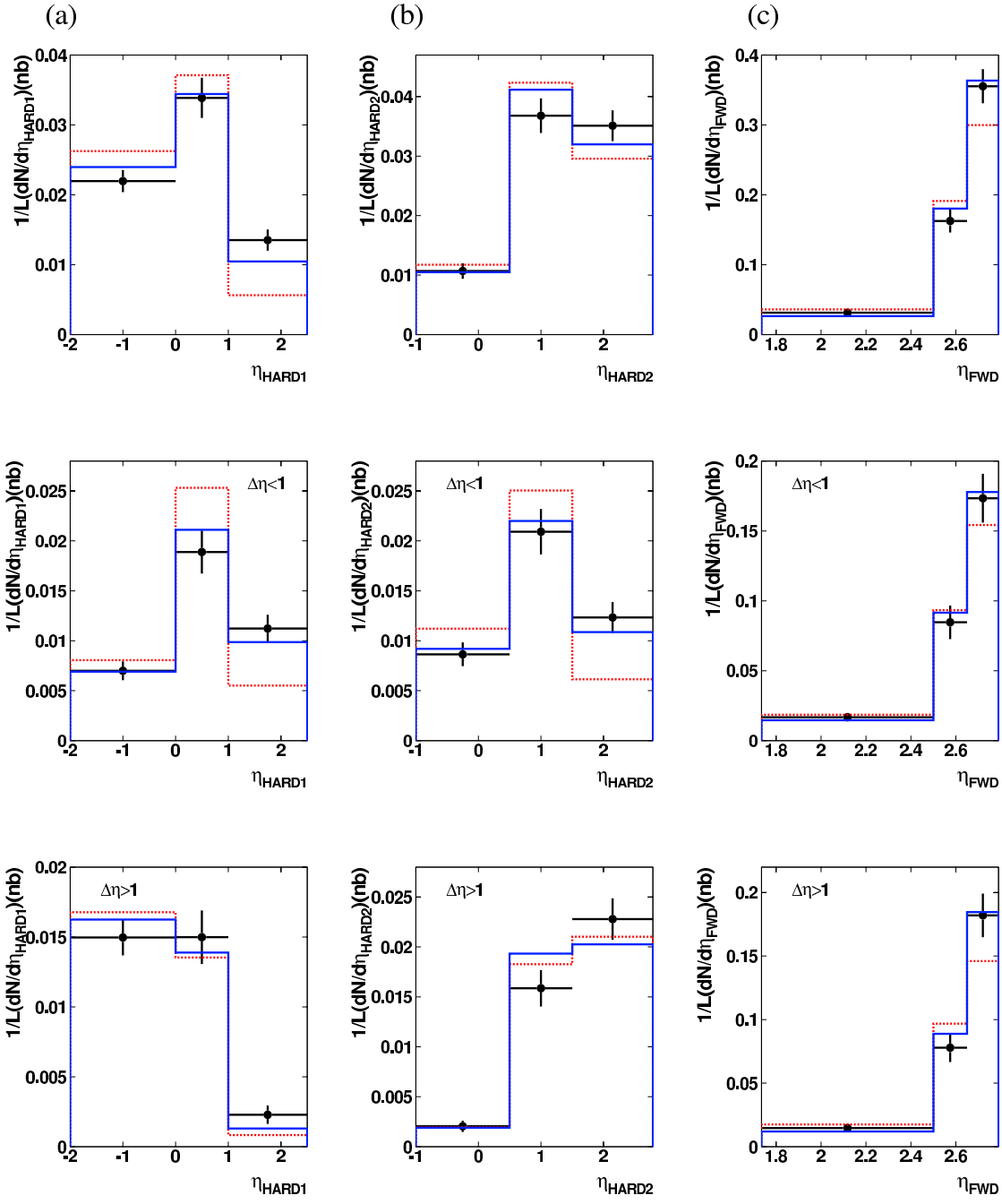

Figure 6.32: *Detector level distributions for 2+forward jet DIS events, showing* (a) η_{HARD1}, (b) η_{HARD2} *and* (c) η_{FWD}, *making no requirement in* $\Delta\eta$ *(upper row), for* $\Delta\eta < 1$ *(middle row) and for* $\Delta\eta > 1$ *(lower row). Experimental data (dots) are compared to detector simulated Monte Carlo data from ARIADNE (full line) and RAPGAP (dashed line). The distributions are scaled to the data, which are normalised to the luminosity,* L.

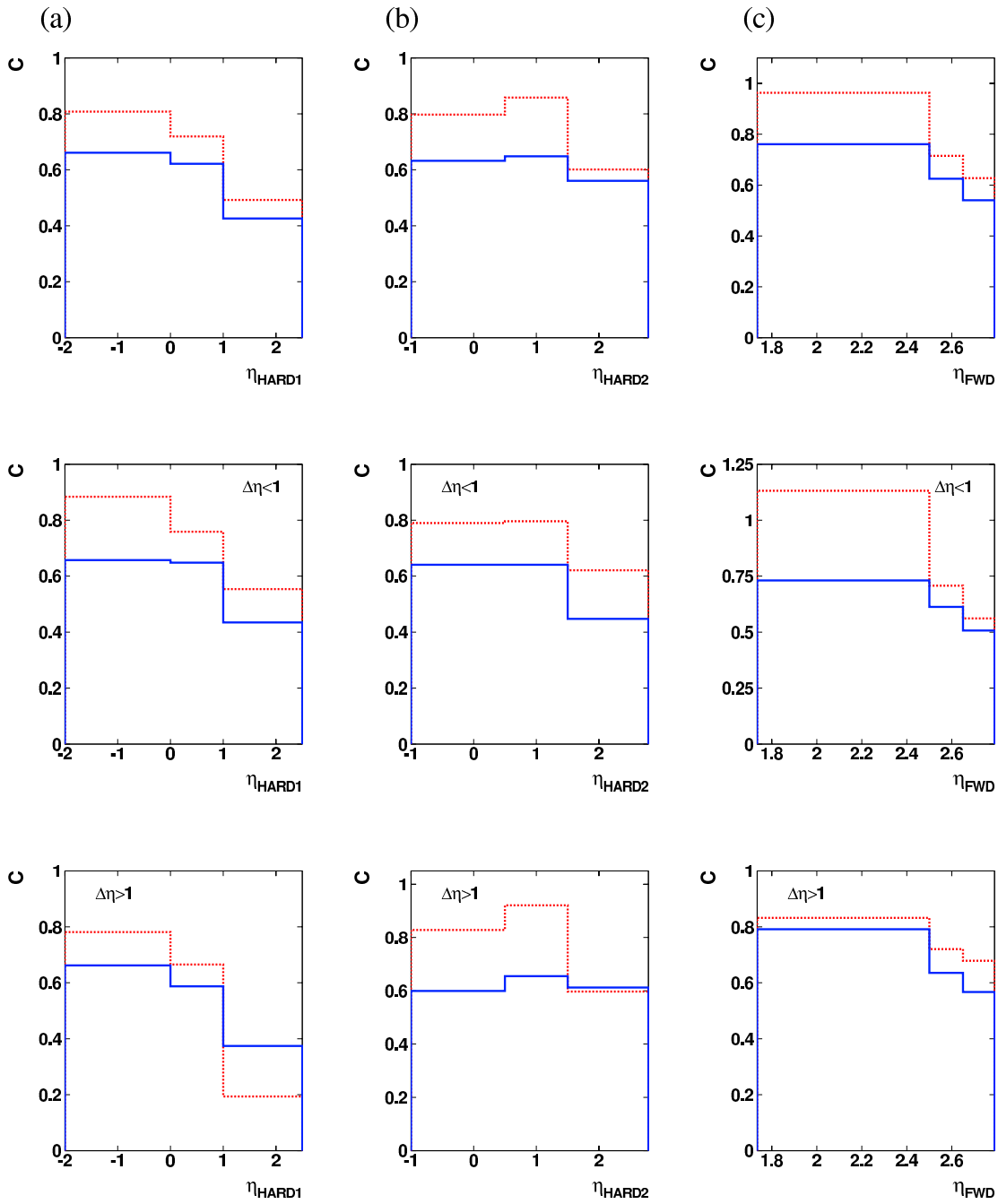

Figure 6.33: *The correction factor, C, for 2+forward jet DIS events, calculated in bins of (a) η_{HARD1}, (b) η_{HARD2} and (c) η_{FWD}, making no requirement in $\Delta\eta$ (upper row), for $\Delta\eta < 1$ (middle row) and for $\Delta\eta > 1$ (lower row). The predictions from Monte Carlo generators ARIADNE (full line) and RAPGAP (dashed line) are shown.*

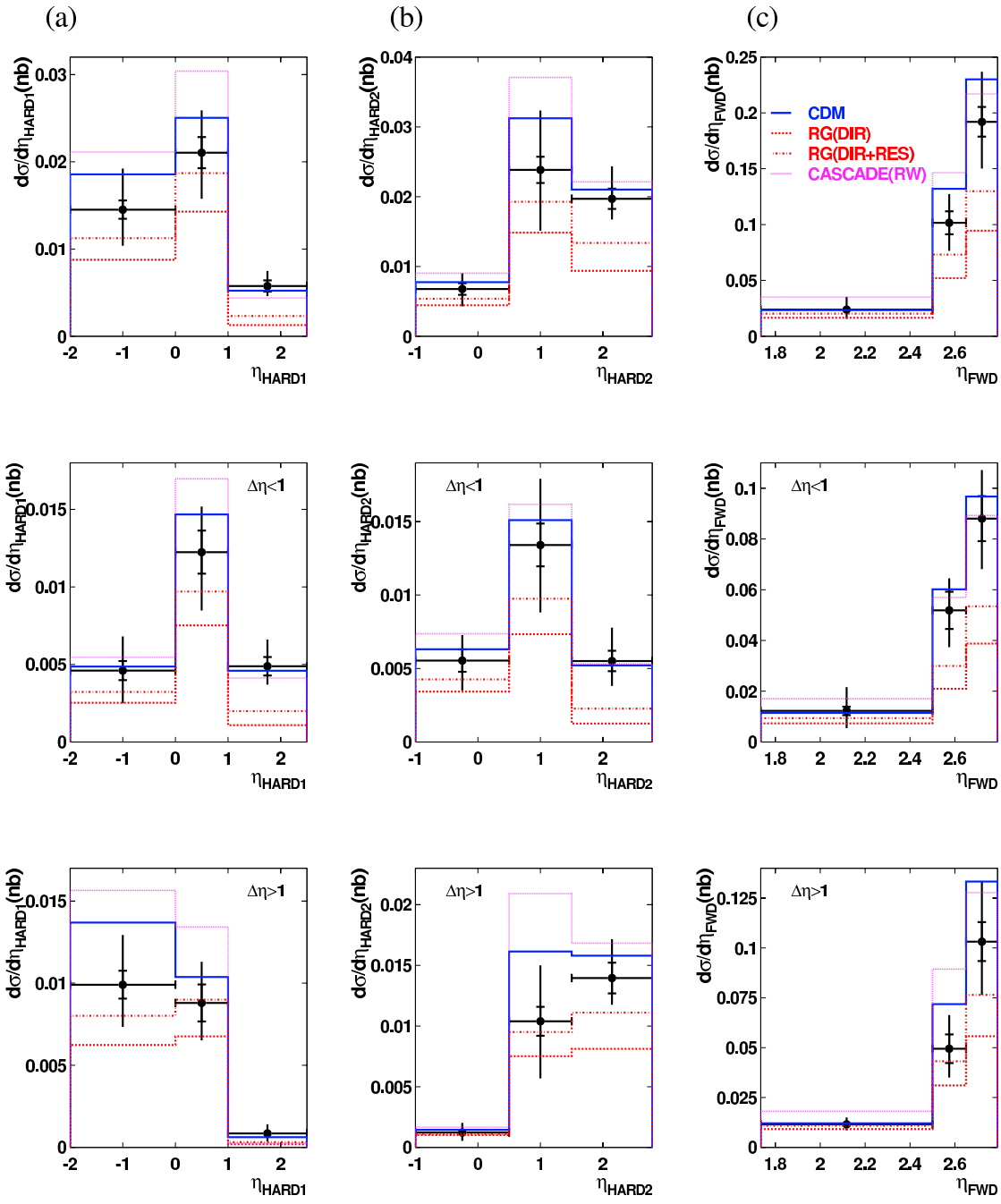

Figure 6.34: *The 2+forward jet DIS event differential cross-section shown* (a) *as a function of* η_{HARD1}, (b) *as a function of* η_{HARD2} *and* (c) *as a function of* η_{FWD}, *making no requirement in* $\Delta\eta$ *(upper row), for* $\Delta\eta < 1$ *(middle row) and for* $\Delta\eta > 1$ *(lower row).*

in shape when $\Delta\eta < 1$.

6.9 Conclusions and Outlook

We have measured the forward jet event cross-section as a function of Bjoerken-x, the forward jet transverse momentum $p_{T,FWD}$, and of the fraction of the protons momentum carried by the forward jet, x_{JET}. The measurement is based on a $13.72\ pb^{-1}$ data sample taken by the H1 collaboration during the 1997 running period at HERA. The data are corrected to hadron level and compared to a number of QCD model predictions. The cross-section predictions of the DGLAP-based Monte Carlo generator RAPGAP shows significant deviations from the cross-section of data. Including the contribution from a resolved component of the virtual photon, the accuracy of the description increases and is often within the errors of the measurement. The ARIADNE Monte Carlo generator, based on the colour dipole model, describes the forward jet event cross-section well, for all distributions measured. The cross-section given by the CASCADE generator, based on CCFM evolution, tends to overshoot that of data, but often describes the shape of the distributions.

The first measurement of 3-jet events at HERA that includes the forward region, has been carried out as an extension of the forward jet event cross-section measurement, giving a more detailed picture of the parton ladder. We demand that two "hard" jets are found in addition to the forward jet, and again investigate the event cross-section as a function of Bjoerken-x, $p_{T,FWD}$, and x_{JET}. The description of data provided by standard DGLAP is unsatisfactory also here, but within the errors of data to a larger extent than in the standard forward jet measurement. Adding the possibility of resolving the photon, a better description of the data is given. The CDM cross-section often agrees well with that of data, but the description is less exact for 2+forward jet events, than for standard forward jet events. CASCADE as in the standard forward jet measurement overestimates the cross-section of data, but for the 2+forward jet event selection describes the shape of data less accurately.

We have studied the rapidities of the jets defining a 2+forward jet event, for different distances in rapidity, $\Delta\eta$, between the hard subsystem jets of such an event, thereby investigating the different parts of the ladder separately, for different QCD cascade structures. The standard DGLAP scheme is generally inadequate also here. Requiring that $\Delta\eta > 1$, and including the possibility of resolving the photon, an often reasonable description of the jet rapidities is obtained. The resolved photon model can however not contribute with an accurate description when $\Delta\eta < 1$, where CDM gives a good description of the data. The description provided by CDM is however often unsatisfactory for $\Delta\eta > 1$. This indicates a possibility to differentiate between the ladder structure of the resolved photon model, and a ladder that is unordered in virtuality, by applying a $\Delta\eta$ cut. We also note that CASCADE gives its best description of the rapidity distribution shapes when $\Delta\eta < 1$.

The study of forward jet events provides us with information on the dynamics of the low-x QCD cascade, and by studying 2+forward jet events, we are able to specifically investigate different parts of the ladder. Starting from a 2+forward jet event selection, the QCD cascade

between the hard subsystem and the forward jet could also be investigated. Reconstructing jets from the softer emissions of this region, and measuring the cross-section for events in which a different number of such jets are found, would provide us with a more direct description of the different possible ladder structures. A measurement of the difference and correlation in transverse momentum between the propagators of the parton ladder, using mini-jets, has been carried out in [67] and [68]. The 2+forward jet event cross-section measurements of our analysis may be seen as providing a foundation for analyses of this kind. Additional observables of interest in this respect exist, such as the k_T *dispersion* variable presented in [69].

The data collected at HERA during the period 1998-2000 comprises a total luminosity of around $100\ pb^{-1}$, thus enabling an increase in the statistics of the exclusive forward jet event selection, and an effective decrease in the errors of a measurement such as ours. Due to the increase in the proton beam energy from 820 GeV to 920 GeV, lower values of Bjoerken-x than before can also be reached, and a greater relative statistic for the low-x region will be available.

Chapter 7

Acknowledgements

I would like to thank Leif Jönsson for through all these years being constantly supportive of me, and for supervision and help. Hannes "Puten" Jung for supervision, answers to questions, and for invaluable lessons in historical and dialectical materialism. My old colleague Mattias "D Diddy" Davidsson. Albert "Abomination" Knutsson for help with the bug in *selcuts.txt*. Rasmus Mackeprang for help with generator results. Thanks to the people at the University of Lund Department of Elementary Particle Physics (does it now still exist?) for their assistance in things and for putting up with me. I would also like to thank the whole H1 collabration and in particular the Jet/HaQ working group at H1. Shout out to family and friends. Peace.

Bibliography

[1] S. Aid et al., *Nucl. Phys.* **B470** (1996) 3.

[2] C. Callan, D. Gross, *Phys. Rev. Lett.* **22** (1969) 156.

[3] R. E. Taylor, *Rev. Mod. Phys.* **63** (1991) 573.

[4] V. Gribov, L. Lipatov, *Sov. J. Nucl. Phys.* **15** (1972) 438 and 675.

[5] L. Lipatov, *Sov. J. Nucl. Phys.* **20** (1975) 94.

[6] G. Altarelli, G. Parisi, *Nucl. Phys.* **B 126** (1977) 298.

[7] Y. Dokshitzer, *Sov. Phys. JETP* **46** (1977) 641.

[8] S. Aid et al., *Phys. Lett.* **B356** (1995) 118.

[9] J. Breitweg et al., *Eur. Phys. J.* **C6** (1999) 239.

[10] J. Breitweg et al., *Phys. Lett.* **B474** (2000) 223.

[11] C. Adloff et al., *Nucl. Phys.* **B538** (1999) 3.

[12] C. Adloff et al., *Phys. Lett.* **B462** (1999) 440.

[13] V. Fadin, E. Kuraev, L. Lipatov, *Sov. Phys. JETP* **45** (1972) 199.

[14] Y. Balitsky, L. Lipatov, *Sov. J. Nucl. Phys.* **28** (1978) 822.

[15] A. Martin, *Contemporary physics* **36** (1995) 335.

[16] M. Ciafaloni, *Nucl. Phys.* **B296** (1988) 49.

[17] S. Catani, F. Fiorani, G. Marchesini, *Phys. Lett.* **B 234** (1990) 339.

[18] S. Catani, F. Fiorani, G. Marchesini, *Nucl. Phys.* **B336** (1990) 18.

[19] S. Catani, M. Ciafaloni, F. Hautmann, *Nucl. Phys.* **B366** (1991) 135.

[20] H. Jung, *Comp. Phys. Commun.* **86** (1995) 147.

[21] H. Jung, L. Jonsson, H. Kuster, *hep-ph/9805396* (1998) .

[22] G. Ingelman, A. Edin, J. Rathsman, *Comput. Phys. Commun.* **101** (1997) 108.

[23] G. Marchesini et al., *Comput. Phys. Commun.* **67** (1992) 465.

[24] H. Jung, *Comput. Phys. Commun.* **143** (2002) 100.

[25] J. B. et. al, *Eur. Phys. J.* **C1** (1998) 81.

[26] B. Andersson, The Lund Model, 1998, iSBN 0 521 42094 6.

[27] L. Loennblad, , in *Hamburg 1991, Proceedings, Physics at HERA, vol. 3* 1440-1445. (see HIGH ENERGY PHYSICS INDEX 30 (1992) No. 12988).

[28] M. Derrick et al., *Phys. Lett.* **B315** (1993) 481.

[29] T. Ahmed et al., *Nucl. Phys.* **B429** (1994) 477.

[30] P. Landshoff., 135, proceedings, Hadronic Aspects of Collider Physics (1994).

[31] T. Regge, *Nuovo Cimento* **14** (1959) 951.

[32] T. Regge, *Nuovo Cimento* **14** (1960) 947.

[33] K. Goulianos, *Phys. Rept.* **101** (1983) 169.

[34] G. Chew, S. Frautschi, S. Mandelstam, *Phys. Rev.* **126** (1962) 1202.

[35] A. Donnachie, P. Landshoff, *Nucl. Phys.* **B 231** (1983) 189.

[36] C. Adloff et al., *Z. Phys.* **C76** (1997) 613.

[37] G. Ingelman, P. Schlein, *Phys. Lett.* **B 152** (1985) 256.

[38] M. Wusthoff, , dESY-95-166.

[39] M. Diehl, Diffraction in electron-proton collisions, 1996, PhD thesis.

[40] J. Bartels, H. Lotter, M. Wüsthoff, *Phys. Lett.* **B 379** (1996) 239.

[41] J. Bartels, C. Ewerz, H. Lotter, M. Wüsthoff, *Phys. Lett.* **B 386** (1996) 389.

[42] J. Bartels, H. Jung, M. Wüsthoff, *Eur. Phys. J.* **C 11** (1999) 111.

[43] H. S. group, The H1 Lead/Scintillating-Fibre Calorimeter, 1996, internal H1 Report, DESY-H1-96-171.

[44] J. Ban et al., *Nucl. Instrum. Meth.* **A372** (1996) 399.

[45] F. Abe et al., *Phys. Rev.* **D45** (1992) 1448.

[46] W. Bartel et al., *Z. Phys.* **C33** (1986) 23.

[47] S. Bethke et al., *Phys. Lett.* **B213** (1988) 235.

[48] T. Sjostrand, *Comput. Phys. Commun.* **28** (1983) 229.

[49] S. Catani, Y. L. Dokshitzer, B. R. Webber, *Phys. Lett.* **B285** (1992) 291.

[50] S. Catani, Y. L. Dokshitzer, M. H. Seymour, B. R. Webber, *Nucl. Phys.* **B406** (1993) 187.

[51] S. D. Ellis, D. E. Soper, *Phys. Rev.* **D48** (1993) 3160.

[52] S. Catani, Y. Dokshitzer, B. Webber, *Phys. Lett.* **B 285** (1992) 291.

[53] S. Catani, Y. Dokshitzer, M. Seymour, B. Webber, *Nucl. Phys.* **B 406** (1993) 187.

[54] T. Sjöstrand, *Comp. Phys. Comm.* **39** (1986) 347.

[55] M. Davidsson, Jet physics at the electron proton collider HERA, 1999, Lic thesis, LUNDFD6/(NFFL-7181)1999.

[56] S. Catani, M. H. Seymour, *Acta Phys. Polon.* **B28** (1997) 863.

[57] B. Potter, Report DESY 98-071, 1998, [hep-ph/9806437].

[58] C. Adloff et al., *Eur. Phys. J.* **C13** (2000) 415.

[59] M. Gluck, E. Reya, A. Vogt, *Z. Phys.* **C67** (1995) 433.

[60] G. A. Schuler, T. Sjostrand, *Phys. Lett.* **B376** (1996) 193.

[61] A. Meyer, Measurement of the Structure Function F2 (x, Q2) of the Proton at Low Q2 with the H1 Detector at HERA Using the New Detector Components Spacal and BDC, 1997, PhD thesis.

[62] C. Adloff et al., *Z. Phys.* **C74** (1997) 221.

[63] E. Lobodzinska, Measurement of the forward jet cross-section in the low-xB region at HERA as a signature of BFKL dynamics, 1997, PhD thesis.

[64] T. Schoerner-Sadenius, Messung inklusiver Jet-Wirkungsquer- schnitte in tiefunelastischer ep- Streuung mit dem H1-Detektor bei HERA, 2001, PhD thesis.

[65] R. Engel, *Z. Phys.* **C66** (1995) 203.

[66] H. Jung, *Acta Phys. Polon.* **B33** (2002) 2995.

[67] M. Karlsson, Jet Reconstruction and its Application in Studies of Parton Dynamics, 2001, Lic thesis.

[68] M. Davisson, Jet Production and Parton Dynamics in Deep Inelastic Scattering, 2001, PhD thesis.

[69] E. A. De Wolf, P. Van Mechelen, (1998) .

Appendix A

Forward Jet Production at HERA

Submitted to
31st International Conference on High Energy Physics, ICHEP02, July 24, 2002, Amsterdam
Abstract: **1001**
Parallel Session **5, 6**
www-h1.desy.de/h1/www/publications/conf/conf_list.html

Forward Jet production at HERA

H1 Collaboration

Abstract

New parton dynamics, characterized by an initial state cascade which is non-ordered in parton virtuality, is expected to become important in the kinematic region of small Bjorken-x_{Bj}. Evidence for this feature of QCD is searched for by studying events with a forward jet produced close to the direction of the incoming proton in the angular range $7^o < \theta_{jet} < 20^o$. The measurements are compared with the predictions of simulations assuming ordered or non-ordered emissions in the initial state cascade. The cross section for forward jet production is presented as a function of x_{Bj}, and shows a significant deviation to the predictions based on DGLAP evolution. We also present the forward jet cross section as a function of x_{jet}, the energy fraction the forward jet takes from the initial proton, and as a function of the transverse momentum of the forward jet, $p_{t\,jet}$.

1 Introduction

HERA has extended the available x_{Bj} region down to values of $x_{Bj} > 10^{-5}$, for values of the momentum transfer, Q^2, larger than a few GeV, where perturbative calculations in QCD are still expected to be valid. In Deep Inelastic Scattering (DIS) a parton in the proton can induce a QCD cascade consisting of several subsequent parton emissions, before the final parton interacts with the virtual photon.

Several different prescriptions of the QCD dynamics at small values of x_{Bj} have been proposed. These include QCD parton evolution schemes such as the DGLAP [1–4] evolution equation, the small x_{Bj} specific BFKL [5–7] evolution equation as well as the CCFM [8–11] evolution equation, which forms a bridge between DGLAP and BFKL using the concept of color coherence.

Differences between the different dynamical approaches to the parton cascade are expected to be most prominent in the phase space region towards the proton remnant direction, i.e. away from the scattered quark.

We investigate the parton evolution at small values of x_{Bj} using jet production in the forward angular region (close to the proton remnant direction) in the laboratory frame. The analysis presented here is based on 5 times more statistics than our published one [12] and is complementary to a similar analysis [13] which used high energetic pions instead of jets. A schematic diagram for forward jet production is shown if Fig 1.

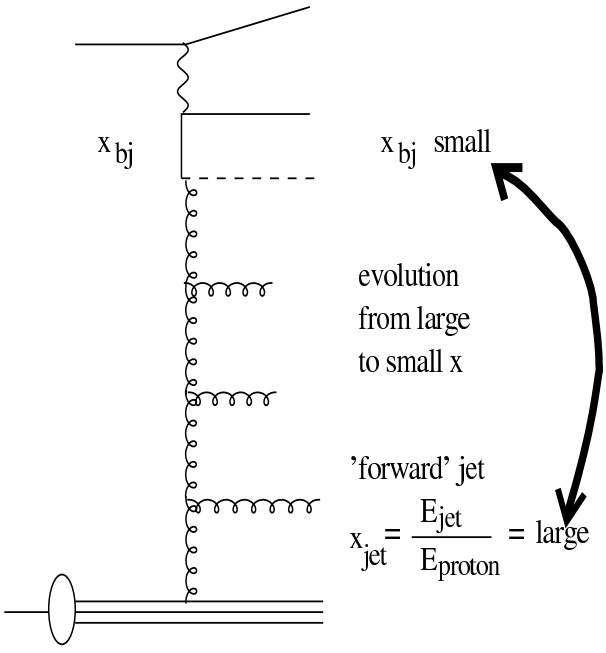

Figure 1: *Schematic diagram for forward jet production at HERA. Indicated is the evolution from large x_{jet} to small x_{Bj} while restricting the phase space for DGLAP evolution in Q^2 by the requirement of $p^2_{t\,jet} \sim Q^2$.*

In the DGLAP evolution scheme, the virtualities k_i of the propagator gluons are strictly increasing from the proton to the photon. Thus the cross section for forward jet production with $p^2_{t\,jet} \sim Q^2$ is expected to be small, since there is no phase space left for further parton radiation between the forward jet and the virtual photon. In the BFKL description, however, the virtualities (and transverse momenta) $k_{\perp i}$ can perform a so-called random walk. Based on calculations in the LLA of the BFKL kernel, the cross section for DIS events at low x_{Bj} and large Q^2 with a high $p^2_{t\,jet}$ jet in the proton direction (a forward jet) [14,15] is expected to rise more rapidly with decreasing x_{Bj} than expected from DGLAP based calculations.

2 Data and analysis method

The region in which the forward jet measurement is performed is chosen such that the phase space for jet production according to the DGLAP evolution is suppressed compared to that available for the BFKL evolution. This is achieved by requiring $p^2_{t\,jet} \sim Q^2$, where $p^2_{t\,jet}$ is the transverse momentum squared of the forward jet. In addition the momentum fraction of the forward jet $x_{jet} = E_{jet}/E_p$ is required to be large, whereas x_{Bj} is kept as small as possible, thus enhancing the phase space for evolution in x while suppressing the evolution in Q^2.

The e^+p scattering data have been collected at $\sqrt{s} = 300\,\mathrm{GeV}$ with the H1 detector in 1997 and comprises all together an integrated luminosity of $13.72\,\mathrm{pb}^{-1}$.

DIS events are selected by requiring a scattered electron in the backward SPACAL calorimeter with an energy $E'_e > 10$ GeV in the angular range of $156^o < \theta_e < 175^o$. The kinematics are determined from the scattered electron: $Q^2 = 4E_eE'_e\cos^2(\theta_e/2)$ and $y = 1 - (E'_e/E_e)\sin^2(\theta_e/2)$ where E_e is the incident positron energy. In summary the following cuts are applied:

$$
\begin{gathered}
E_{e'} > 10\ \text{GeV} \\
156^o < \theta_e < 175^o \\
0.1 < y < 0.7 \\
5\ \text{GeV}^2 < Q^2 < 75\ \text{GeV}^2
\end{gathered}
$$

The forward jets are defined using the inclusive k_t-jet algorithm [16,17] (applied in the Breit-frame without p_t-cut) by requiring:

$$
\begin{gathered}
p_{t\,jet} > 3.5\ \text{GeV} \\
7.0^o < \theta_{jet} < 20.0^o \\
x_{jet} > 0.035 \\
0.5 < p^2_{t\,jet}/Q^2 < 2
\end{gathered}
$$

where $p_{t\,jet}$ is measured in the laboratory frame.

The RAPGAP [18] Monte Carlo model uses LO matrix elements supplemented with initial and final state DGLAP parton showers (DIR-model). In addition resolved virtual photon

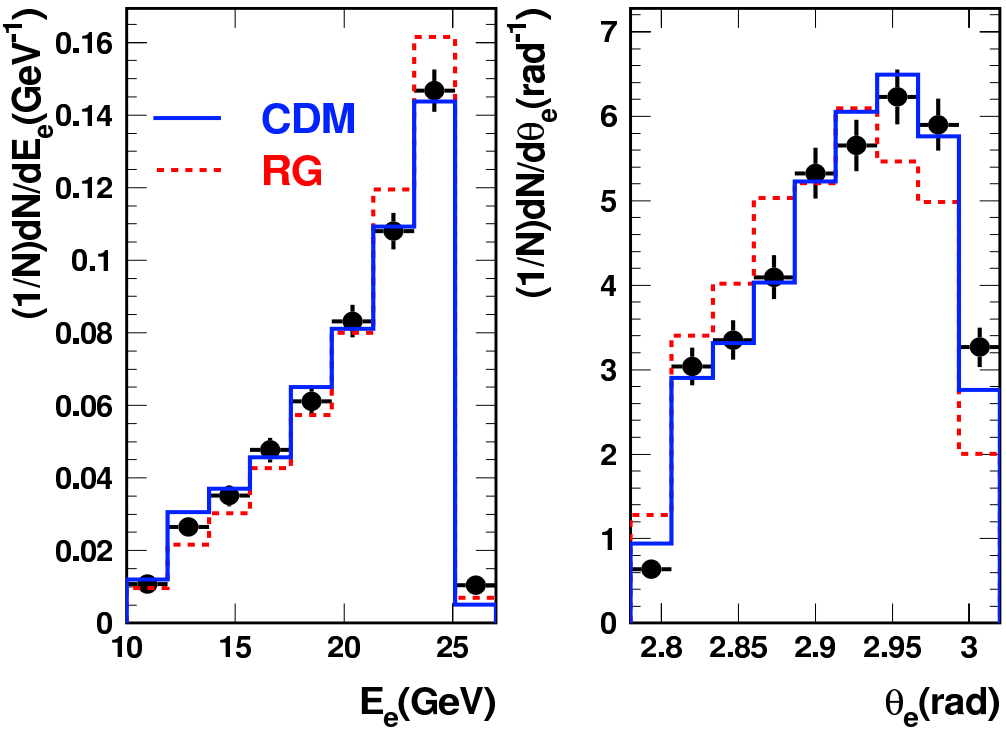

Figure 2: *Distribution of the energy E_e and the angle Θ_e of the scattered electron variables after the forward jet selection. The solid (dashed) line shows the predictions from* DJANGO *- CDM (*RAPGAP *- RG) Monte Carlo after full detector simulation.*

processes can be included (RES-model). The DJANGO [19] Monte Carlo model is used together with the Color-Dipole-Model as implemented in ARIADNE [20] for higher order QCD radiation. Simulated events of the RAPGAP (DIR) and DJANGO Monte Carlo programs have been processed through the detailed H1 detector simulation. In Fig. 2 the normalized distributions of the scattered electron energy and scattering angle, after the forward jet selection, are shown. In Fig. 3 the normalized distributions of basic jet variables, after the forward jet selection, are compared to the Monte Carlo predictions. Good agreement of the data with the full detector simulation of the DJANGO - CDM MC is observed. In Fig. 4 we show the transverse energy flow around the axis of the selected forward jet as a function of $\Delta\eta = \eta_{jet} - \eta_{clus}$ and $\Delta\phi = \phi_{jet} - \phi_{clus}$ in a slice of $\Delta\phi = 1$ and $\Delta\eta = 1$, respectively. Also shown are the predictions from the Monte Carlo simulations.

The DJANGO -CDM Monte Carlo, which describes best the data at detector level, is used for correcting the data to hadron level. The difference of the correction factors obtained by the two Monte Carlos, DJANGO and RAPGAP is $\sim 8\%$, and is treated as systematic error.

The effects of initial state QED radiation are corrected for using HERACLES interfaced to DJANGO and RAPGAP.

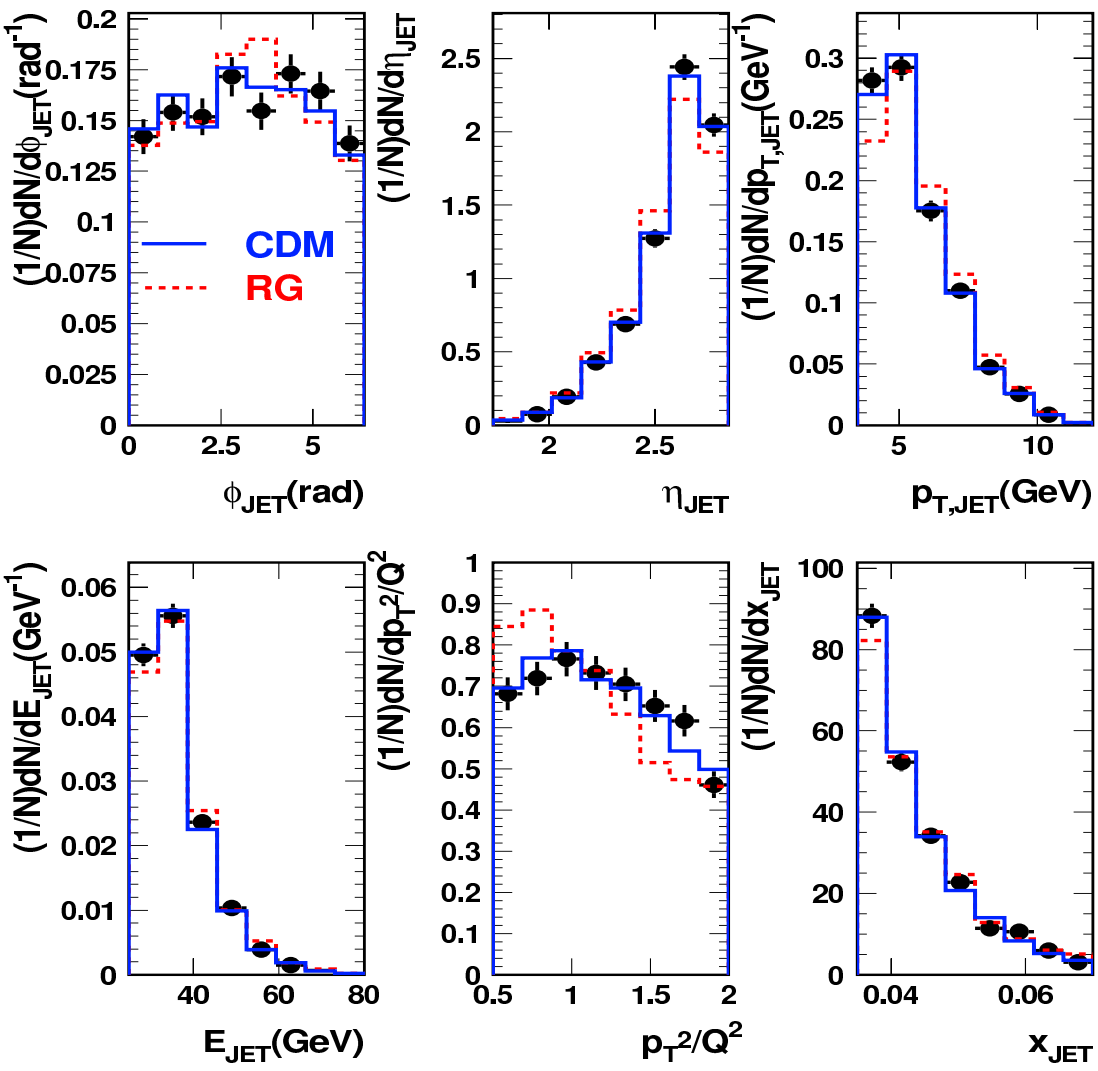

Figure 3: *Distribution of basic jet variables after the forward jet selection. The solid (dashed) line shows the predictions from* DJANGO *- CDM (*RAPGAP *- RG) Monte Carlo after full detector simulation.*

The following systematic errors are considered:

- The error on the hadronic energy scale of 4 % in the LAr- Calorimeter results in an error of the cross section measurement of $\sim 6\%$.
- The error on the electromagnetic energy scale of 1 % of the SPACAL Calorimeter results in an error of the cross section measurement of $\sim 3\%$.
- An error of 1 mrad is assumed on the angle measurement of the scattered electron, resulting in an error of the cross section measurement of $\sim 3\%$.

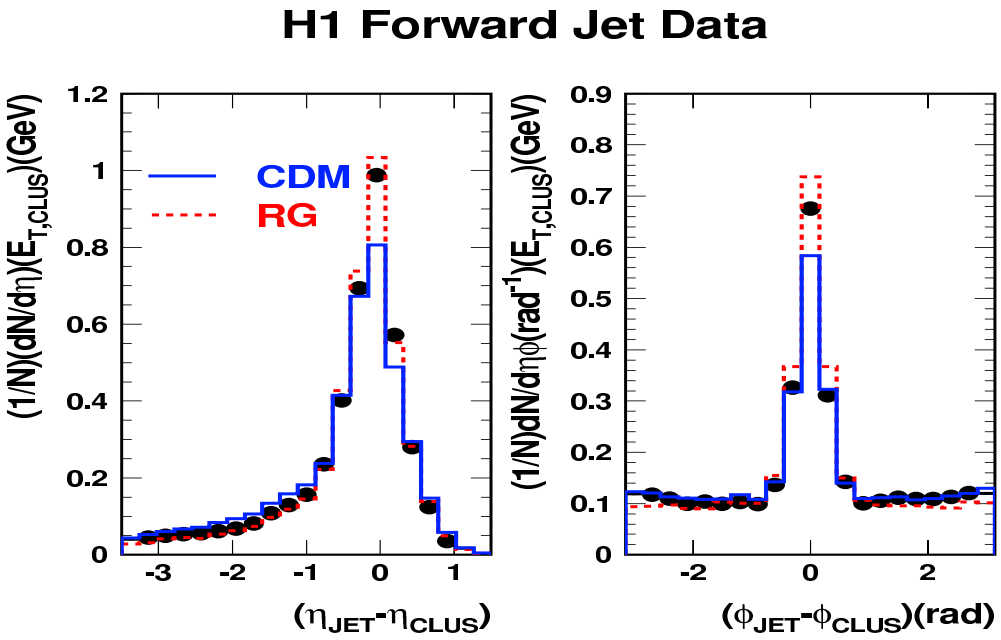

Figure 4: *Transverse energy flow around the axis of the selected forward jet as a function of* $\Delta\eta = \eta_{jet} - \eta_{clus}$ *and* $\Delta\phi = \phi_{jet} - \phi_{clus}$ *in a slice of* $\Delta\phi = 1$ *and* $\Delta\eta = 1$*, respectively. Also shown are the predictions from the* DJANGO *- CDM (solid) and* RAPGAP *- RG (dashed) Monte Carlo simulations.*

- The error coming from the model dependence between RAPGAP and DJANGO of $\sim 8\%$.
- The photoproduction background is estimated using the PHOJET [21,22] Monte Carlo simulations to $\sim 1\%$.

In Fig. 5-7 we show the forward jet cross section as a function of x_{Bj}, x_{jet} and $p_{t\,jet}$ for $p_{t\,jet} > 3.5$ GeV and $p_{t\,jet} > 5$ GeV corrected to the hadron level. Also shown are the predictions from a pure DGLAP type Monte Carlo (RAPGAP- DIR), including also a contribution from resolved virtual photons (DIR+RES), and a simulation using the Color Dipole Model (CDM) as implemented in ARIADNE (DJANGO). In ARIADNE the parton emissions perform a random walk in transverse momentum leading to a situation similar to the one expected in BFKL. Whereas the DGLAP type prediction falls below the data at small x_{Bj}, the CDM prediction gives a reasonable description of the measurement. The CCFM evolution equation in k_t-factorization (CASCADE) overestimates the data.

3 Conclusion

A new measurement of the forward jet production cross section as a function of x_{Bj}, x_{jet} and $p_{t\,jet}$ has been performed using an integrated luminosity of 13.71 pb^{-1}. The data are up to a

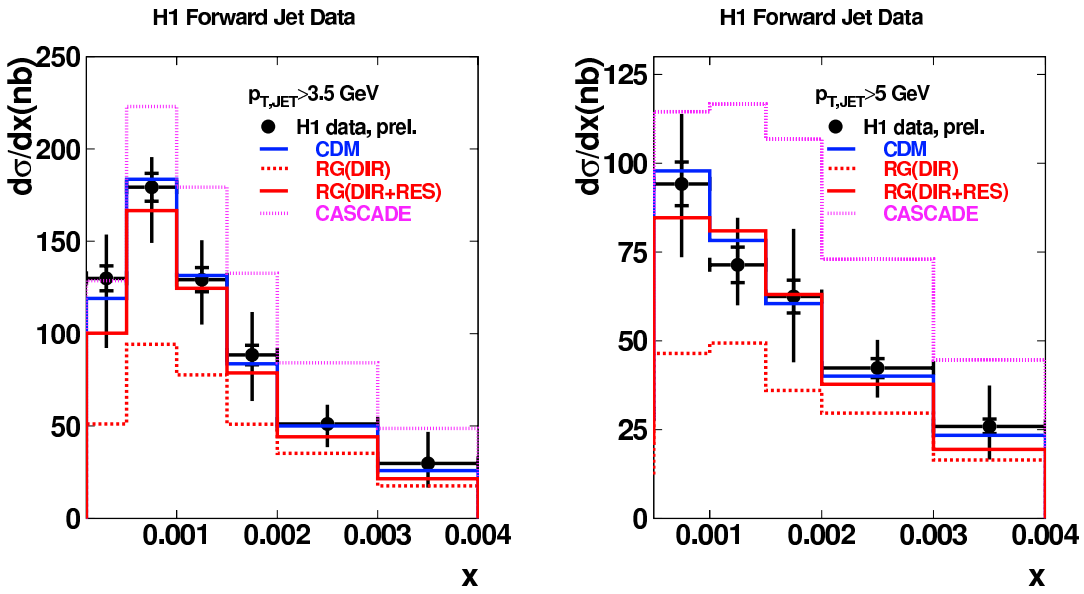

Figure 5: *The cross section for forward jet production on hadron level, as a function of* x_{Bj} *for* $p_{t\,jet} > 3.5$ *GeV (left) and* $p_{t\,jet} > 5$ *GeV (right). Also shown are the predictions from the* ARIADNE *- CDM,* RAPGAP *- RG and* CASCADE *Monte Carlos.*

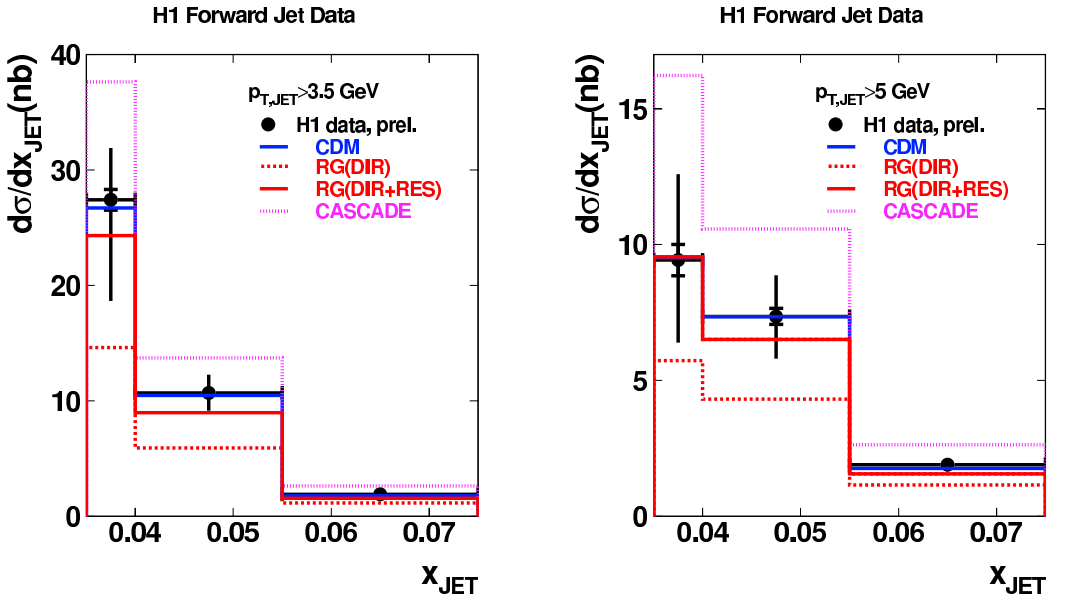

Figure 6: *The cross section for forward jet production on hadron level, as a function of* x_{jet} *for* $p_{t\,jet} > 3.5$ *GeV (left) and* $p_{t\,jet} > 5$ *GeV (right). Also shown are the predictions from the* ARIADNE *- CDM,* RAPGAP *- RG and* CASCADE *Monte Carlos.*

factor of two larger than the predicted cross section based on $\mathcal{O}(\alpha_s)$ and QCD calculation in the collinear factorization ansatz (DGLAP).

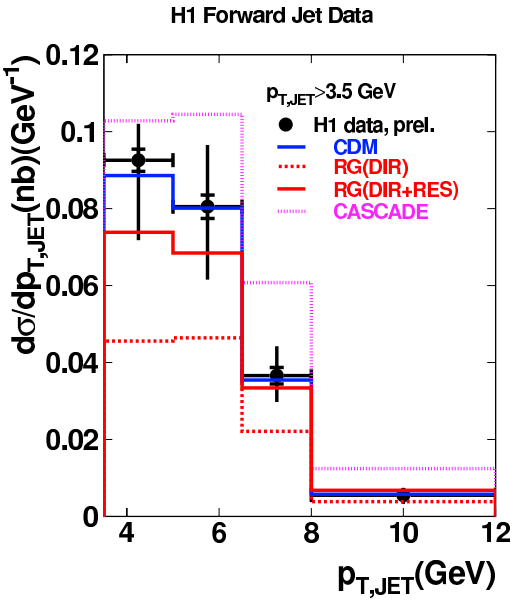

Figure 7: *The cross section for forward jet production on hadron level, as a function of* $p_{t\,jet}$ *for* $p_{t\,jet} > 3.5$ *GeV (left) and* $p_{t\,jet} > 5$ *GeV (right). Also shown are the predictions from the* ARIADNE *- CDM,* RAPGAP *- RG and* CASCADE *Monte Carlos.*

Using a hadron level Monte Carlo model incorporating resolved virtual photon processes in addition to the usual direct photon processes, the data are reasonably well described. Also the Color Dipole Model, which simulates higher order QCD radiation without strong ordering of the transverse momenta of the emitted partons, describes the measurements well. The more sophisticated CCFM approach, which is based on angular ordering coming from color coherence, predicts too high a rate of forward jet events.

References

[1] V. Gribov, L. Lipatov, *Sov. J. Nucl. Phys.* **15** (1972) 438 and 675.

[2] L. Lipatov, *Sov. J. Nucl. Phys.* **20** (1975) 94.

[3] G. Altarelli, G. Parisi, *Nucl. Phys.* **B 126** (1977) 298.

[4] Y. Dokshitser, *Sov. Phys. JETP* **46** (1977) 641.

[5] E. Kuraev, L. Lipatov, V. Fadin, *Sov. Phys. JETP* **44** (1976) 443.

[6] E. Kuraev, L. Lipatov, V. Fadin, *Sov. Phys. JETP* **45** (1977) 199.

[7] Y. Balitskii, L. Lipatov, *Sov. J. Nucl. Phys.* **28** (1978) 822.

[8] M. Ciafaloni, *Nucl. Phys.* **B 296** (1988) 49.

[9] S. Catani, F. Fiorani, G. Marchesini, *Phys. Lett.* **B 234** (1990) 339.

[10] S. Catani, F. Fiorani, G. Marchesini, *Nucl. Phys.* **B 336** (1990) 18.

[11] G. Marchesini, *Nucl. Phys.* **B 445** (1995) 49.

[12] H1 Collaboration, C. Adloff et al., *Nucl. Phys.* **B 538** (1999) 3.

[13] H1 Collaboration, Forward π^0 meson production at HERA, Lidia Goerlich - talk presented at DIS 2002, April, 2002.

[14] A. Mueller, *Nucl. Phys.* **B** *(Proc. Suppl)* **18C** (1990) 125.

[15] A. Mueller, *J. Phys.* **G 17** (1991) 1443.

[16] S. Catani, Y. Dokshitzer, M. Seymour, B. Webber, *Nucl. Phys.* **B 406** (1993) 187.

[17] S. Catani, Y. Dokshitzer, B. Webber, *Phys. Lett.* **B 285** (1992) 291.

[18] H. Jung, *The RAPGAP Monte Carlo for Deep Inelastic Scattering, version 2.08*, Lund University, 2002, `http://www.quark.lu.se/~hannes/rapgap/`.

[19] G. A. Schuler, H. Spiesberger, , in *Hamburg 1991, Proceedings, Physics at HERA, vol. 3* 1419-1432. (see HIGH ENERGY PHYSICS INDEX 30 (1992) No. 12988).

[20] L. Lönnblad, *Comp. Phys. Comm.* **71** (1992) 15.

[21] R. Engel, *Z. Phys.* **C66** (1995) 203.

[22] R. Engel, J. Ranft, *Phys. Rev.* **D54** (1996) 4244, hep-ph/9509373.